Coherence and Spectral Properties of Composite-Cavity Semiconductor Lasers

Thesis by
John M. Iannelli

In Partial Fulfillment of the Requirements
for the Degree of
Doctor of Philosophy

California Institute of Technology
Pasadena, California

1995

(Defended May 17, 1995)

To Gemma

Acknowledgments

I would like to extend my deepest gratitude and appreciation to my thesis advisor, Professor Amnon Yariv, for his patience, guidance, and assistance during my graduate career. His skills as both a physicist and a leader have made my studies at Caltech rewarding and enjoyable. A large part of the success of my research can be attributed to the open and intellectually stimulating environment Professor Yariv has created and maintained in his laboratories. His support and confidence are truly appreciated.

I am also very appreciative of the many students in Professor Yariv's research group that I have been able to work alongside. It has been a privledge to share thoughts and ideas with some of the brightest and most creative students one could ever encounter. In particular, I have benefited greatly from working with John Kitching, Randal Salvatore, Tony Kewitsch, Yuanjian Xu, and Thomas Schrans. The assistance of Jana Mercado with administrative matters was always appreciated very much. I am very grateful to Dr. T.R. Chen of the Ortel Corporation and Professor Bruno Crosignani of the University of Rome for many beneficial collaborations. Also, the friendship of Professor Ricardo Gomez of the Caltech department of Physics has broadened my insights into experimental physics as well as the appreciation of fine music. His humor and generosity are greatly appreciated.

I am very thankful to several agencies for the support I received during my graduate studies. These include the California Institute of Technology, The University of Glasgow, The National Science Foundation, and American Mensa. Their generosity

certainly relieved some of the drudgery of graduate student life.

Lastly, I would like to thank all of my family for their support and understanding throughout my education. Despite being several thousand miles away, my parents always provided me with the confidence and trust that only parents can. Their support in all of my efforts has been unwaivering and will always be remembered. I would also like to thank my mother and father-in-law who have always been understanding and supportive of their son-in-law's education. Finally, I would like to thank my wife Gemma. Through my successes and failures, she has always been there for me. Without her love and support, none of this would have been possible.

Coherence and Spectral Properties of Composite-Cavity Semiconductor Lasers

by

John M. Iannelli

In Partial Fulfillment of the
Requirements for the Degree of
Doctor of Philosophy

Abstract

This thesis addresses many current issues in the theoretical and experimental aspects of coherence and spectral properties of semiconductor lasers. It begins with a brief overview of the theory of fluctuations in semiconductor lasers. This includes a study of relative intensity noise, frequency/phase noise, and frequency chirp. A method of spectral linewidth reduction and stabilization is then proposed and analyzed. This method utilizes an atomic resonance in cesium to which a semiconductor laser can be frequency locked. A Van der Pol analysis as well as a rate equation analysis are carried out and predict reductions in the spectral linewidth, frequency chirp, and enhanced frequency stability. Experimental results confirm several aspects of the theory and also introduce the effects of 1/f noise in semiconductor lasers. Spectral linewidth reductions by a factor of 2000 below the solitary laser linewidth are presented.

Investigations are then made into the spectral characteristics of multielectrode distributed feedback (DFB) lasers. A novel measurement technique is introduced which utilizes the phase angle between the FM and AM responses for the determination of adiabatic chirp and linewidth enhancement factors. The mode switching properties of these devices are then studied within the context of bistable operation. Bistability in output power and output wavelength is shown and is applied to experiments in stochastic resonance. Using bistable DFB and Fabry-Perot semiconductor lasers, stochastic resonance is demonstrated experimentally in different laser systems as well as in electronic circuits. The effect is analyzed from a rate equation approach as well as a Kramer's escape approach. Results predict a noise suppression at higher even harmonic frequencies which are then experimentally verified.

Contents

List of Figures

List of Tables

Chapter 1

Introduction

Although optical communication systems are a relatively recent technological development, they have evolved through several design and application schemes. Early systems suffered from low quality transmission media and sources. As single mode fiber optics became better developed in terms of loss and dispersion characteristics, the research in semiconductor lasers as viable components in these systems intensified. Some of the primary uses envisioned for semiconductor lasers were as optical transmitters and functional photonic switching devices. As of today, research in both of these applications remains active.

1.1 Optical Communication Systems

Current optical communication systems frequently employ an intensity modulation / direct detection scheme. Laser output power is modulated through injection current modulation and detection is typically accomplished through the use of an avalanche photodiode. This system is relatively simple in terms of detection schemes however, it leaves room for much improvement. Analogous to communication systems which employ microwaves as a carrier, the high carrier frequency of the optical field can be exploited in a system of phase and/or frequency modulation. Such systems can improve the reciever sensitivity by as much as 20 dB compared to intensity modulated / direct detection systems as well as increase transmission capacity since the large bandwidth of the fiber can be utilized. These systems are frequently called coherent communication systems since the phase or frequency must be coherently demodulated by a local oscillator.

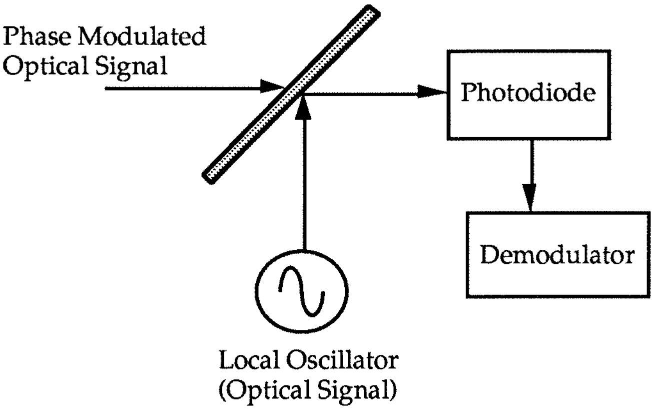

Figure 1-1: Schematic diagram of a coherent optical communications system.

A schematic diagram of a coherent communications system in shown in Figure 1-1. The local oscillator is also a semiconductor laser whose frequency can either be equal to that of the incoming optical signal (homodyne detection) or can be a slightly different frequency (heterodyne) in which case the summing action at the beam splitter produces an intermediate frequency analogous to a superheterodyne

Modulation Format	*Photons / Bit*
PSK Homodyne	9
PSK Heterodyne	18
FSK Heterodyne	36
ASK Homodyne	36
ASK Heterodyne	72

Table 1.1: Sensitivities of various modulation formats in a coherent receiver. (PSK: Phase Shift Keying, FSK: Frequency Shift Keying, ASK: Amplitude Shift Keying)

receiver in radio technology.

Depending on the modulation format used, the receiver sensitivity can be drastically improved. In Table 1.1 the number of photons per bit required is tabulated in order to achieve a bit error rate (BER) of 10^{-9}.

For comparison, a typical intensity modulated / direct detection receiver would require appoximately 2000 photons per bit for the same BER [1]. In order to realize these sensitivities in an actual communications system, the spectral linewidths of both the input signal and the local oscillator laser are extremely critical. Although the effects of a finite spectral linewidth are manifested differently in different modulation formats, phase fluctuations will be directly converted to photocurrent fluctuations because of the coherent nature of the demodulation process. As an example, a synchronous heterodyne PSK system with a BER of 10^{-9} requires a linewidth of 1 MHz for approximately 20 photons per bit.

In addition to the requirement on the semiconductor laser for narrow spectral linewidths, the absolute frequency and its stability are often of importance in communication systems. One method of utilizing the large fiber bandwidth without excessively large modulation bandwidths is to multiplex various frequencies as separate channels (known as frequency division multiplexing; FDM). Since channel spacing can be quite small in coherent systems (¡10 GHz) there is a need for lasers which not only demonstrate high coherence but also a high degree of frequency stability.

1.2 Photonic Functional Units

In addition to the vast uses of semiconductor lasers as transmitters and detector components in today's communication systems, these devices are also being considered for performing many logical and decision making functions which until recently were completely within the realm of digital electronics. There are several reasons for pursuing such applications with semiconductor lasers. First, the switching speed of many of the optical processes in these lasers is much faster than that in conventional electronics. More importantly, functional units based on semiconductor lasers would eliminate the optical/electrical/optical conversion process typically encountered. Instead of detecting an optical signal, performing signal processing and conditioning electrically, and then regenerating a new optical signal, the process could be kept in the optical regime thereby opening the possibility for improving the system's efficiency.

Some of the system applications currently being researched include all-optical repeaters, clock regenerators, and wavelength conversion devices. Many of these devices rely on an optically bistable semiconductor laser acting as a thresholding device [2,3]. A variety of devices have been investigated including bistable Fabry-Perot lasers [11], distributed feedback lasers [5], and distributed Bragg reflector structures [6].

1.3 Outline of the Thesis

This thesis begins with a review and discussion of semiconductor laser coherence theory, specifically amplitude and phase noise. Fundemental concepts such as the relaxation resonance, spectral linewidth, and relative intensity noise are described in detail. From there, a technique of phase noise reduction utilizing optical feedback is analyzed both theoretically and experimentally. This particular technique employs a frequency locking technique to an atomic resonance such that both linewidth reduction and frequency stability are achieved.

Frequency chirp and its measurement in complex devices is then analyzed for a three section distributed feedback (DFB) laser with suporting experimental results. A new measurement technique which uses the FM and AM responses of the semiconductor laser allows not only measurements of chirp but also of gain compression.

Lastly, a phenomenon known as stochastic resonance is introduced and applied to semiconductor lasers as a means of signal processing for both the electro-optical and optical-optical conversion schemes. The effect shows an increase in the output signal to noise ratio with an increase in input noise power. It is described theoretically and experimental results are presented for a variety of electro-optical systems.

References

[1] G.P.Agrawal, *Fiber-Optic Communication Systems*, John Wiley and Sons, New York, 1992.

[2] H.Kawaguchi, *Bistabilities and Nonlinearities in Laser Diodes*, Artech House, Boston, 1994.

[3] H.Kawaguchi, *Int. J. Optoelectronics*, vol.7, p.301, 1992.

[4] Ch.Harder, K.Lau, and A.Yariv, *Appl. Phys. Lett.*, vol.39, p.382, 1981.

[5] M.J.Adams and R.Wyatt, *IEE Proc. Pt. J*, vol.134, p.35, 1987.

[6] M.Margalit, R.Nagar, N.Tessler, G.Eisenstein, M.Orenstein, U.Koren, and C.A.Burrus, *Opt. Lett.*, vol.18, p.610, 1993.

Chapter 2

Theory of Fluctuation Phenomena in Semiconductor Lasers

2.1 Introduction

As discussed in the previous chapter, the coherence properties of semiconductor lasers can impose limitations to their performance in modern optical communication systems. In this chapter the various mechanisms and magnitudes of noise in semiconductor lasers will be described in detail. There are several aspects of semiconductor lasers which distinguish them from other laser systems in as far as noise is concerned. Without external modifications, semiconductor lasers possess a relatively low Q cavity as a consequence of their small size and low facet reflectivities. Therefore, noise and its subsequent reduction in these devices has become an area of extensive theoretical and experimental research [2,1,5,14,16,5].

If one assumes that a semiconductor laser is biased above threshold with an ideally constant injection current (i.e., neglecting fluctuations in injected carrier density), the two dominant mechanisms of noise are spontaneous emission and electron-hole recombination (i.e., shot noise) [2]. For our discussions we are primarily concerned with spontaneous emission. For a treatment of shot noise and its effects in semiconductor laser noise the reader is referred to other references [12,13]. Spontaneous emission events can be shown to affect not only the amplitude of the field but also its phase due to its lack of coherence with the existing lasing field. Obviously, its consequences are extremely important in the proper design of optical communication systems [3].

2.2 Noise Properties of Semiconductor Laser Diodes

Before embarking on the techniques of noise reduction in semiconductor lasers, we first consider the noise properties of these devices without any modifications such as feedback. It will be shown in the following chapter that optical feedback can be adequately treated as a simple extension of this theory.

2.2.1 Formulation of the Optical Field

In order to describe laser oscillation and the various noise properties of semiconductor lasers we employ the standard semiconductor laser rate equations [2]. The important quantities of interest are the electric field, the phase, and the carrier number. The electric field within the laser cavity is written as

$$E(\mathbf{x}, t) = Re[A(t)e^{-i\omega_L t}]\Phi(\mathbf{x}) \tag{2.1}$$

where ω_L is the lasing (angular) frequency, $\mathbf{x}$ is the (vector) spatial coordinate, and $A(t)$ is referred to as the complex wave amplitude. The complex amplitude $A(t)$, a very useful quantity for describing noise and coherence, is given by

$$A(t) = \sqrt{S(t)}e^{[-i\phi(t)]} \tag{2.2}$$

where $S(t)$ is the mean photon number in the cavity and $\phi(t)$ is the phase of the optical field. The rate equation for $A(t)$ is given by

$$\frac{dA(t)}{dt} = \frac{1}{2}(G - \frac{1}{\tau_p})(1 - i\alpha)A(t) \tag{2.3}$$

where G is the gain, τ_p is the photon lifetime, and α is the linewidth enhancement factor. This factor is proportional to the ratio of refractive index changes with carrier density to gain changes with carrier density and can be shown to be non zero in semiconductor lasers [18]. It is a dimensionless quantity with a typical value between 4 and 6 for semiconductor lasers [11]. It can be seen that gain saturation ($G = \frac{1}{\tau_p}$) causes $A(t)$ to be constant in steady state thereby causing the photon number $S(t)$ (and $E(t)$) to oscillate precisely at frequency ω_L and the phase $\phi(t)$ to also be constant. However, fluctuations in the field due to spontaneous emission cause changes in the photon number and phase. The changes in the photon number are damped by gain saturation and lead to relaxation oscillations of both the photon and carrier number. The changes in phase, however, are not damped and in fact are somewhat increased by gain saturation. The effects of these fluctuations on $A(t)$ can be simplistically illustrated as shown in Figure 2-1. This figure shows the phasor diagram of the complex amplitude driven by a single spontaneous emission event. Since spontaneous emission adds photons incoherently to the field, the phase angle γ is uniformly distributed as $-\pi < \gamma < \pi$. In the top graph, the instantaneous addition of a photon to the optical field is shown at time $t = \epsilon$. An instantaneous phase change ϕ' results as well as an increase in $S(t)$. However, since the carrier number has been reduced (by one) the gain is reduced accordingly. Since semiconductor lasers operate as detuned oscillators (i.e., the frequency of the imaginary part of the suceptibility maximum differs from the frequency of the real part of the sucepibility zero [18]), the restoration of the gain to its threshold value results in an additional phase change designated in the bottom graph as ϕ''.

These fluctuations can be represented mathematically by "driving" Equation 2.3 with an appropriate Langevin force as

$$\frac{dA(t)}{dt} = \frac{1}{2}(G - \frac{1}{\tau_p})(1 - i\alpha)A(t) + F_A(t). \qquad (2.4)$$

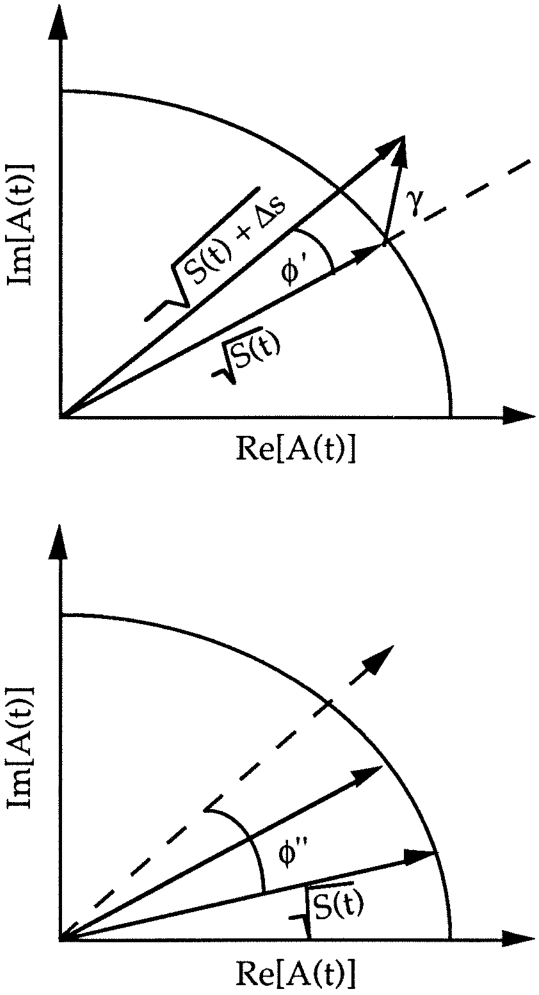

Figure 2-1: Phasor diagram of complex amplitude driven by spontaneous emission

In general, the force $F_i(t)$ is a complex quantity possessing the following properties:

$$< F_i(t) > \; = \; 0 \tag{2.5}$$

$$< F_i(t)F_j(t+\tau) > \; = \; 2D_{ij}\delta(\tau) \tag{2.6}$$

where D_{ij} is a diffusion coefficient and δ is the Dirac delta function. The second property, the fact that the force possesses no memory (i.e., the system is Markoffian), can be justified for semiconductor lasers since the laser emission process can be considered to be dominated by the equilibration time of injected carriers which is approximately 0.1 ps [11]. This is far shorter than any time scale of the dynamical processes in question.

2.3 Laser Fluctuation Spectra

In order to quantify the various fluctuation processes in semiconductor lasers it is appropriate to calculate correlation spectra between the dynamical variables. By separating Equation 2.3 into its real and imaginary parts and adding a carrier number rate equation we have the complete set of semiconductor laser rate equations. These are given by

$$\frac{dS(t)}{dt} = (G - \frac{1}{\tau_p})S(t) + \beta R^{SP} + F_S(t) \tag{2.7}$$

$$\frac{d\phi(t)}{dt} = \frac{\alpha}{2}(G - \frac{1}{\tau_p}) + F_\phi(t) \tag{2.8}$$

$$\frac{dN(t)}{dt} = C - GS(t) - \frac{N(t)}{\tau_N} + F_N(t) \tag{2.9}$$

where R^{SP} is the spontaneous emission rate, β is the fraction of spontaneous emission coupled into the lasing mode, C is the number of injected carriers per second (I/e), and τ_N is the carrier spontaneous recombination lifetime. The rate equations are now expanded in the small signal regime using the following approximations:

$$S(t) = <S> + s(t) \tag{2.10}$$

$$N(t) = <N> + n(t) \tag{2.11}$$

$$G = <G> + G_N n(t) + G_S s(t) \tag{2.12}$$

where $G_{X_i} = \frac{\partial G}{\partial X_i}$ and $< X >$ denotes a time averaged quantity. With these expansions the small signal rate equations now become

$$\dot{s}(t) = G_N n(t) <S> - \Gamma_S s(t) + F_S(t) \tag{2.13}$$

$$\dot{\phi} = \frac{\alpha}{2} G_N n(t) + F_\phi(t) \tag{2.14}$$

$$\dot{n} = -\Gamma_N n(t) - G s(t) + F_N(t) \tag{2.15}$$

$$\begin{aligned} \frac{d\phi(t)}{dt} &= \frac{\alpha}{2}(G - \frac{1}{\tau_p}) + F_\phi(t) && (2.8) \\ \frac{dN(t)}{dt} &= C - GS(t) - \frac{N(t)}{\tau_N} + F_N(t) && (2.9) \end{aligned}$$

where R^{SP} is the spontaneous emission rate, β is the fraction of spontaneous emission coupled into the lasing mode, C is the number of injected carriers per second (I/e), and τ_N is the carrier spontaneous recombination lifetime. The rate equations are now expanded in the small signal regime using the following approximations:

$$\begin{aligned} S(t) &= <S> + s(t) && (2.10) \\ N(t) &= <N> + n(t) && (2.11) \\ G &= <G> + G_N n(t) + G_S s(t) && (2.12) \end{aligned}$$

where $G_{X_i} = \frac{\partial G}{\partial X_i}$ and $< X >$ denotes a time averaged quantity. With these expansions the small signal rate equations now become

$$\begin{aligned} \dot{s}(t) &= G_N n(t) <S> - \Gamma_S s(t) + F_S(t) && (2.13) \\ \dot{\phi} &= \frac{\alpha}{2} G_N n(t) + F_\phi(t) && (2.14) \\ \dot{n} &= -\Gamma_N n(t) - G s(t) + F_N(t) && (2.15) \end{aligned}$$

where

$$\begin{aligned} \Gamma_S &= \frac{\beta R^{SP}}{< S >} + G_S && (2.16) \\ \Gamma_N &= \frac{1}{\tau_N} + G_N < S > . && (2.17) \end{aligned}$$

From Equations 2.13 and 2.15 one can see that Γ_N and Γ_S are the self-damping rates of the carrier and photon number fluctuations, respectively. (By self-damping rates, we refer to the effective damping rate in the absence of fluctuations in variables other than the one in question.) Physically, Γ_N consists of carrier recombination (via τ_N) and a reduction in the stimulated emission rate (via G_N). Similarly, the photon number is damped through spontaneous emission as well as nonlinear gain represented through G_S.

At this point, the system of three coupled differential equations can be readily solved via Fourier transformation methods. Designating a transformed variable with a tilde, we have

$$\begin{bmatrix} \tilde{s}(\Omega) & \tilde{\phi}(\Omega) & \tilde{n}(\Omega) \end{bmatrix} \begin{bmatrix} i\Omega + \Gamma_S & 0 & -G_N < S > \\ 0 & i\Omega & 0 \\ < G > & \frac{-\alpha}{2} G_N & i\Omega + \Gamma_n \end{bmatrix} = \begin{bmatrix} \tilde{F}_S(\Omega) & \tilde{F}_\phi(\Omega) & \tilde{F}_N(\Omega) \end{bmatrix} \tag{2.18}$$

where Ω is the frequency variable of the Fourier transformation. The transformed variables can be solved for by application of Cramer's rule and thereafter inverse transformed to obtain the time-dependent quantities. However, the algebraic solution of the transformed variables alone enables the calculation of various laser field spectra.

2.3.1 Correlations of the Langevin Forces

In general, the laser field spectra will be of the form

$$Spectra \sim < X_i(\Omega) X_j(\Omega) > \tag{2.19}$$

where $X_i(\Omega)X_j(\Omega)$ represents a particular combination of $\tilde{s}(\Omega)$, $\tilde{\phi}(\Omega)$, and $\tilde{n}(\Omega)$. Since these variables are functions of the Langevin forces $\tilde{F}_i(\Omega)$, their correlations will be necessary. Here we present only a brief and sufficient synopsis of these properties. A more complete treatment can be found in the works of M.Lax [6,7,8,9,11].

The system of equations 2.13-2.15 represents a form of the general Langevin system of equations given by

$$\frac{d\psi_i(t)}{dt} = \Psi_i(t) + F_i(t) \tag{2.20}$$

where the quantity $\Psi_i(t)$ is known as the drift vector and $F_i(t)$ is the Langevin force with diffusion coefficient D_{ij} as defined in Equation 2.6. The drift and diffusion terms can be understood on somewhat physical grounds by considering the Fokker-Planck equation for the time dependent probability $P(\psi, t)$ given as

$$\frac{\partial P}{\partial t} = -\frac{\partial}{\partial \psi}(\Psi P) + \frac{\partial^2}{\partial \psi^2}(DP). \tag{2.21}$$

The diffusion coefficient D (which in the general case can be time dependent) describes the diffusion of the probability $P(\Psi(t), t)$ while $\Psi(t)$ describes the *counteraction* of the drift vector on this diffusion process. In order to determine the diffusion coefficients, we consider a fluctuation process in which the dynamical variable $\psi_i(t)$ undergoes fluctuations at an average rate ρ_i with the magnitude of the fluctuation equal to η_i. In can be shown that in this case the diffusion coefficients are given as [6]

$$2D_{\psi_i\psi_i} = \rho_i \int g_i(\eta_i){\eta_i}^2 d\eta_i \qquad (2.22)$$

$$= \rho_i < {\eta_i}^2 > \qquad (2.23)$$

where g_i is the distribution function of the fluctuation amplitude.

Beginning with the phase equation we have

$$2D_{\phi\phi} = \rho_\phi < \Delta\phi^2 > \qquad (2.24)$$

The phase fluctuation $\Delta\phi$ and its corresponding time averaged quantity can be found from Figure 2-1 to be equal to

$$\Delta\phi = \frac{\sin\delta}{\sqrt{S}} \qquad (2.25)$$

$$< \Delta\phi^2 > = < \frac{\sin^2\delta}{S} > \qquad (2.26)$$

$$= \frac{1}{2 < S >} \qquad (2.27)$$

We have only included the contribution of ϕ' since we are interested only in the effects of spontaneous emission. Gain saturation plays no role in the Langevin correlation of the phase. Since phase fluctuations are driven by spontaneous emission, it follows from Equation 2.23

$$2D_{\phi\phi} = \frac{R^{SP}}{2S} \tag{2.28}$$

In discussing the fluctuations in photon and carrier number we could apply a similar treatment as above for determining the diffusion coefficients, however a somewhat different approach proves to be more insightful. When discussing fluctuations that change a population in unit increments of plus or minus one, Equation 2.22 can be modified. Considering the two processes of generation and dissipation of the variable $\psi(t)$ the distribution function $g(\eta)$ now becomes

$$g(\eta) = prob(generation)\delta(\eta - 1) + prob(dissipation)\delta(\eta + 1) \tag{2.29}$$

Carrying through the integration in Equation 2.22 it can easily be shown that

$$2D_{\psi_i(t)\psi_i(t)} = (\mathcal{G}_{ii} + \mathcal{D}_{ii}) \tag{2.30}$$

where $\mathcal{G}_{ii}$ and $\mathcal{D}_{ii}$ represent the rates of generation and dissipation, respectively, of the populations for ψ_i.

Beginning with the photon number rate equation (Equation 2.7) we see that gain saturation provides the drift vector counteraction ($\mathcal{G} = G, \mathcal{D} = \frac{1}{\tau_p}$) on photon population fluctuations caused by spontaneous emission. From Equation 2.30 we obtain

$$\begin{aligned} 2D_{SS} &= \mathcal{G}_{SS} + \mathcal{D}_{SS} && (2.31) \\ &= 2G < S > && (2.32) \\ &= 2R^{SP} < S > && (2.33) \end{aligned}$$

where Equation 2.33 is obtained by noting that the stimulated emission rate $G < S >$ is essentially equal to $R^{SP} < S >$ above threshold.

In order to obtain the diffusion coefficient for fluctuations in the carrier number, we write the generation and dissipation rates as

$$\begin{aligned} \mathcal{G}_{\mathcal{N}\mathcal{N}} &= \mathcal{A} < \mathcal{S} > && (2.34) \\ \mathcal{D}_{\mathcal{N}\mathcal{N}} &= \frac{< N >}{\tau_N} + G < S > && (2.35) \end{aligned}$$

where $\mathcal{A}$ is the rate of absorption.

Similar to the calcuation above, we obain

$$2D_{NN} = 2(R^{SP} < S > -G) + \frac{< N >}{\tau_N} \tag{2.36}$$

The remaining diffusion coefficients can be found through the same procedure [11]. The results are listed in Table 2.1.

$2D_{SS}$	$2R^{SP} < S >$
$2D_{\phi\phi}$	$\frac{R^{SP}}{2<S>}$
$2D_{NN}$	$2\left\lvert R^{SP} < S > -G \right\rvert + \frac{<N>}{\tau_N}$
$2D_{SN}$	$-2R^{SP} < S >$
$2D_{S\phi}$	0
$2D_{N\phi}$	0

Table 2.1: Langevin diffusions coefficients for semiconductor lasers

Intensity Noise Spectrum

Having found the necessary correlations between the Langevin forces we can now calculate the various laser correlation spectra. We define a quantity known as the relative intensity noise (RIN) as

$$RIN = \frac{< \Delta P^2 >}{< P >^2} \tag{2.37}$$

where P is the average power in the cavity. In order to obtain the fluctuation spectrum of the intensity of the optical field, one can equivalently determine the fluctuation spectrum of the photon number S. In terms of S this power is given as

$$P = h\nu \frac{c}{2nL} \ln \left[\frac{1}{r_1 r_2} S \right] \tag{2.38}$$

where $c/2nL$ is the cavity free spectral range and r_1 and r_2 are the facet reflectivities. In terms of the previously defined small quantities the expression for the RIN now becomes (in a given bandwidth Δf)

$$(RIN)_{\Delta f} = 2\Delta f \frac{< |s(\Omega)|^2 >}{< S >^2} \tag{2.39}$$

The factor of 2 arises from the integration over both positive and negative frequencies in the Fourier transform.

Solving for the photon number fluctuation we have

$$\tilde{s}(\Omega) = \frac{[(i\omega + \Gamma_N)\tilde{F}_S + G_N < S > \tilde{F}_N]}{(\Omega_r + \Omega - i\overline{\Gamma})(\Omega_r - \Omega + i\overline{\Gamma})} \tag{2.40}$$

where we have defined the relaxation oscillation resonance frequency Ω_r^2 and an average damping rate $\overline{\Gamma}$ as

$$\begin{aligned} \Omega_r^2 &= (G + G_S < S >)(G_N < S >) - \frac{(\Gamma_N - \Gamma_S)^2}{4} && (2.41) \\ \overline{\Gamma} &= \frac{1}{2}(\Gamma_N + \Gamma_S) && (2.42) \end{aligned}$$

We can now apply Equation 2.39 and obtain an expression for the relative intensity noise. It is instructive to separate this fluctuation spectrum into sections as

$$RIN = (RIN)^{SS} + (RIN)^{NN} + (RIN)^{SN} \tag{2.43}$$

where each part corresponds to its respective correlation process. Solving Equation 2.39 yields

$$RIN = \frac{2R^{SP}(RIN^{SS} + RIN^{NN} + RIN^{SN})}{< S > [(\Omega_r^2 - \Omega^2)^2 + (2\Omega\overline{\Gamma})^2]} \qquad (2.44)$$

$$RIN^{SS} = \Gamma_N^2 + \Omega^2 \qquad (2.45)$$

$$RIN^{NN} = {G_N}^2 < S >^2 (1 + \frac{< N >}{\tau_N R^{SP} < S >}) \qquad (2.46)$$

$$RIN^{SN} = -2R^{SP}\Gamma_N G_N < S > \qquad (2.47)$$

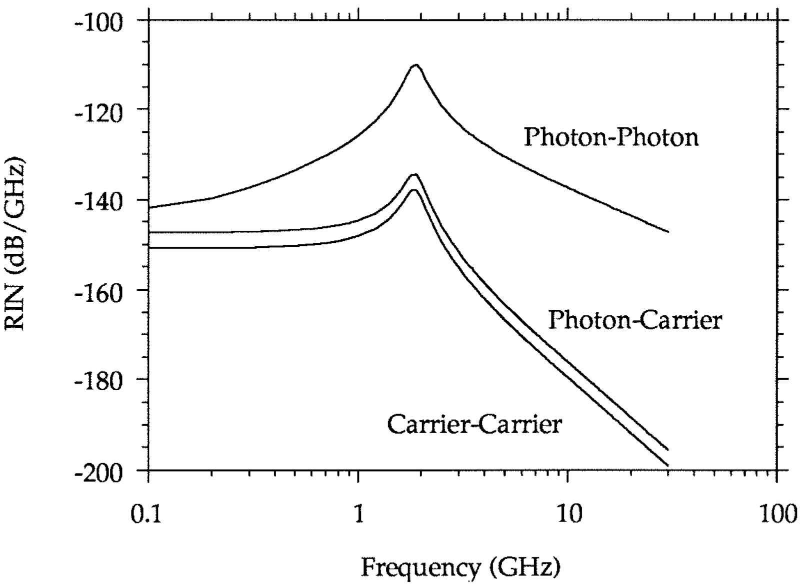

Figure 2-2: Separate contributions of the relative intensity noise spectrum (RIN) as a function of frequency. The photon-carrier contribution shown actually contributes a reduction in RIN as shown in Equation 2.47

It should be noted that the various correlations are all positive except for the cross correlation of the carrier-photon term. This correlation actually reduces the RIN which can be understood as a consequence of gain saturation above threshold.

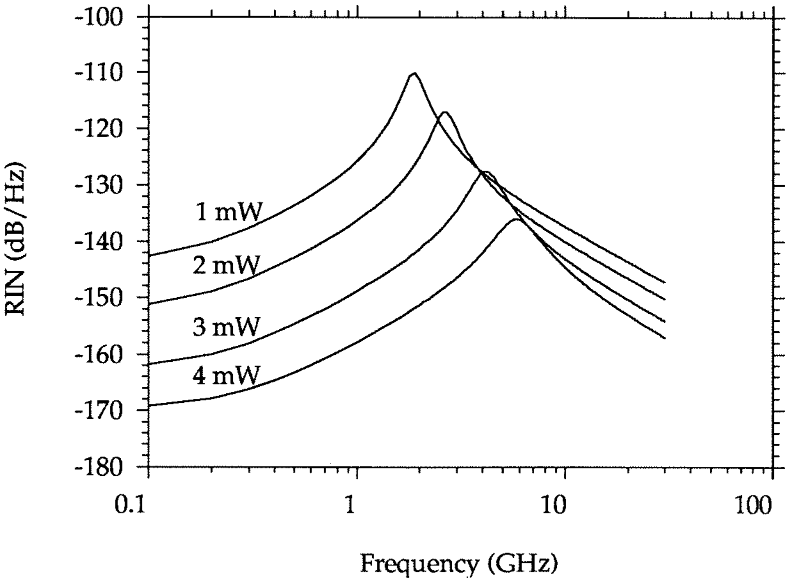

Figure 2-3: Dependence of RIN on the output power

It is instructive to plot the separate contributions of RIN as shown in Figure 2-2. The dominant contribution is shown to be due to the photon-photon correlations while the carrier-carrier and carrier-photon contributions can be safely neglected in most cases. This figure shows the familiar resonance peak at Ω_r and a decrease of the RIN level by 20 dB/decade above this resonance.

As the photon number $< S >$ increases the RIN should decrease accordingly as shown in Equation 2.44. In Figure 2-3 it is shown that not only does RIN decrease with output power but the relaxation resonance frequency also moves to higher frequencies.

In addition to decreasing RIN through an increase in the output power, it seems intuitive that any negative damping on the photon fluctuations should also decrease RIN. This should be provided by a nonlinear gain mechanism since this provides a direct damping on the photon population (see Equation 2.13). In Figure 2-4 we

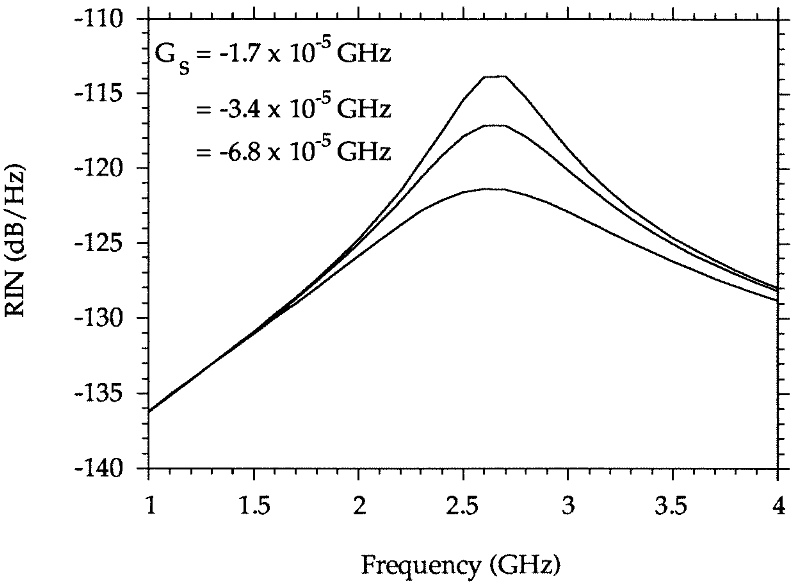

Figure 2-4: Dependence of RIN on the magnitude of the nonlinear gain coefficient

show the RIN level in the vicinity of the relaxation resonance at various levels of the nonlinear gain. The decrease in RIN with G_S can be understood as a decrease in the Q-factor of the oscillation with the corresponding increase in the damping coefficient.

Frequency Noise Spectrum

In addition to the fluctuations in the amplitude of the laser field, fluctuations in frequency are also of considerable interest. The frequency fluctuation spectrum is defined as

$$S_{\dot{\phi}}(\Omega) = \left\langle |\Omega\tilde{\phi}(\Omega)|^2 \right\rangle \tag{2.48}$$

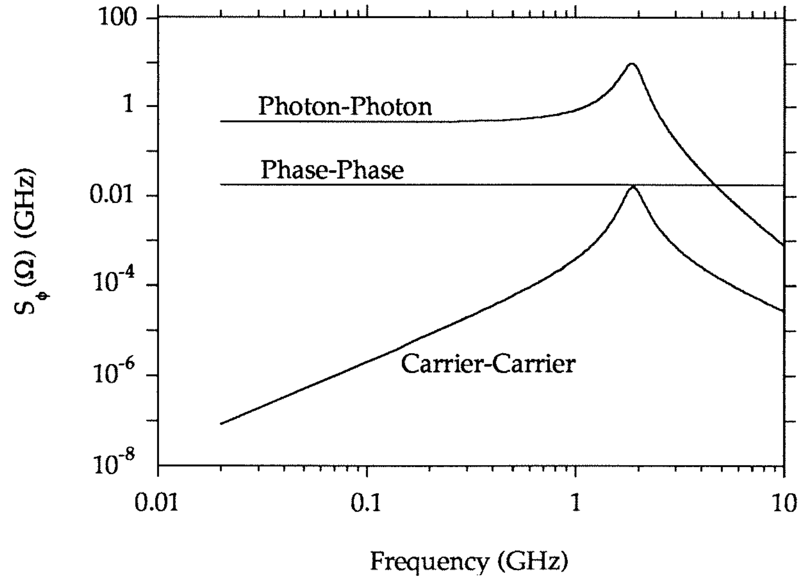

Figure 2-5: Frequency noise spectrum with various correlation contributions

From Equation 2.18 the phase fluctuation is found to be

$$\tilde{\phi}(\Omega) = \frac{1}{i\Omega}\left(\tilde{F}_{\phi} + \frac{\alpha}{2}G_N\tilde{n}\right) \tag{2.49}$$

Substitution of Equation 2.49 into 2.48 yields

$$\begin{aligned} S_{\dot{\phi}}(\Omega) \;=\; & \frac{R_{SP}}{2<S>} + \frac{\alpha^2 {G_N}^2}{2D^2}\Big[(\Gamma_S^2 + \Omega^2)R_{SP} <S> + R_{SP} <S> \cdot \\ & (G + G_S <S>)^2 + 2R_{SP} <S> \Gamma_S(G + G_S <S>)\Big] \end{aligned} \tag{2.50}$$

where D is defined as the denominator found in the bracketed expression for RIN in Equation 2.44.

As with the treatment of the relative intensity noise, one can examine the indi-

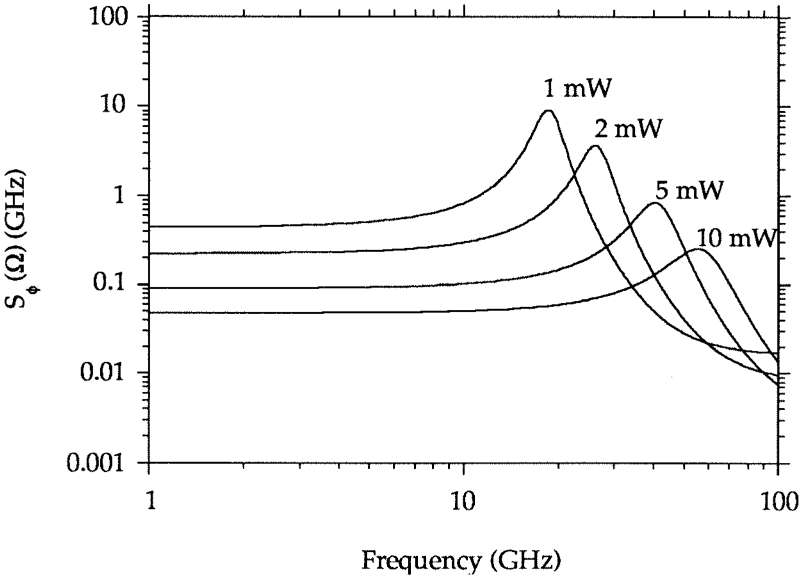

Figure 2-6: Dependence of frequency noise spectrum on the output power.

vidual contributions to the frequency fluctuation spectrum arising from the various correlations. These can be written as

$$S_{\dot\phi}^{\phi\phi} = \frac{R^{SP}}{2<S>} \tag{2.51}$$

$$S_{\dot\phi}^{SS} = \frac{\alpha^2 G_N^2}{2D^2}(G + G_S <S>)^2 R^{SP} <S> \tag{2.52}$$

$$S_{\dot\phi}^{NN} = \frac{\alpha^2 G_N^2}{2D^2}(\Gamma_S^2 + \Omega^2) R^{SP} <S> \tag{2.53}$$

These three contributions are plotted as a function of frequency in Figure 2-5. The phase contribution is simply the quantum noise arising from spontaneous emission events. Its noise power is independent of frequency (white). The other two contributions are a result of the dependence of the phase on carrier density (through the α parameter). The dominant mechanism is the correlation term of the photon number.

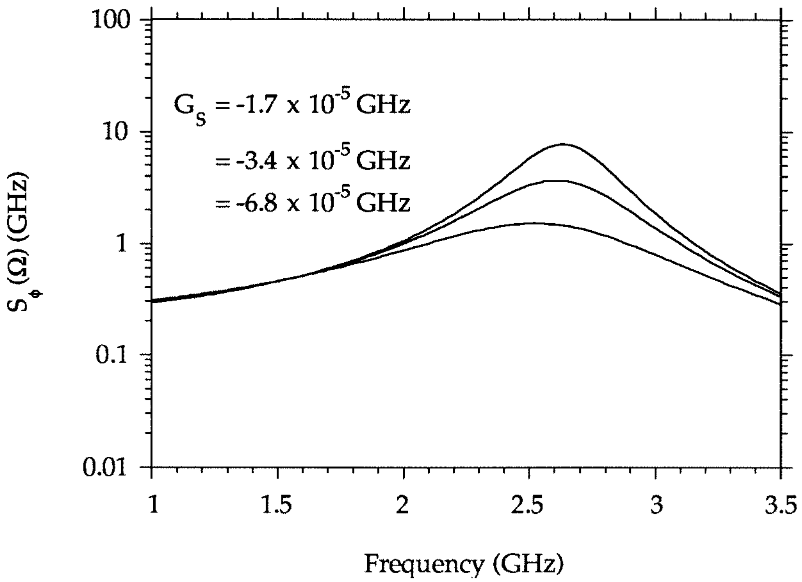

Figure 2-7: Dependence of the frequency noise spectrum on the magnitude of the nonlinear gain coefficient

This arises from the fact that carrier density fluctuations are induced by spontaneous emission and through the amplitude/phase coupling, refractive index changes occur which lead to further phase changes. The ratio of the magnitudes of these two noise sources is equal to α^2.

We can approximate this expression by noting that G is typically much larger that Γ_S or Ω. With these approximations the expression for the frequency fluctuation spectrum becomes

$$S_{\dot{\phi}}(\Omega) = \frac{R_{SP}}{2 < S >}\left[1 + \frac{\alpha^2 \Omega_r^4}{(\Omega_r^2 - \Omega^2)^2 + (2\Omega\overline{\Gamma})^2}\right] \tag{2.54}$$

From this expression one can clearly see the two distinct contributions to the frequency noise arising from spontaneous emission. As discussed previously (see Figure 2-1), the initial spontaneous emission event contributes $R_{SP}/(2 < S >)$ to the frequency noise while the delayed phase change due to the coupling of the carrier density and the refractive index produces the second term in Equation 2.54. This second term, whose "scaling factor" is the linewidth enhancement factor α, introduces as frequency dependence to the noise spectrum. Random spontaneous emission events produce a white noise distribution while the secondary amplitude/phase coupling events lead to an enhancement of the noise in the vicinity of the relaxation resonance frequency Ω_r.

In addition to its frequency dependence, the frequency noise spectrum decreases with increasing power. These results are shown in Figure 2-6. An increase in power not only decreases the magnitude of the FM noise but also extends the resonance frequency which follows directly from Equation 2.40. Furthermore as with the relative intensity noise, increasing the damping of gain fluctuations will also decrease the enhanced frequency noise at the relaxation resonance frequency. This behavior is shown in Figure 2-7 for various values of the nonlinear gain coefficient.

At this point it is worth noting that other noise sources exist which contribute to $S_{\dot{\phi}}(\Omega)$. The frequency noise spectrum calculated in Equation 2.54 is correct from the point of view of the rate equations being used in this treatment. However, in practice there are further frequency noise sources such as temperature fluctuations and $1/f$ noise of often unknown origins. These sources typically dominate the frequency noise spectrum at lower frequencies and must be addressed for such applications.

From the frequency noise spectrum one can determine the spectral linewidth of the optical field. A frequently employed definition of the spectral linewidth is

$$\Delta\omega =_{\Omega\rightarrow 0} S_{\dot{\phi}}(\Omega) \tag{2.55}$$

From Equation 2.54 one obtains

$$\Delta\nu = \frac{R^{SP}}{4\pi < S >}\left(1+\alpha^2\right) \tag{2.56}$$

The first term of this expression is the familiar Schawlow-Townes linewidth formula [21]. In a semiconductor laser the linewidth broadening arises from the secondary amplitude/phase changes discussed above and in Figure 2-1. This expression also gives the familiar $1/ < S >$ dependence on the spectral linewidth. While this dependence is observed at low output powers. at higher output powers the linewidth saturates or even rebroadens with increasing power [22].

2.3.2 Frequency Chirp

In our treatment of frequency noise and the spectral linewidth above, fluctuations or direct changes in the injection current were neglected and only spontaneous emission driven effects were considered. However, for the purposes of modulation the changes in frequency with changes in injection current need to be addressed. Changes in frequency with injection current, an effect known as frequency chirp, can be broadly classified into two categories; dynamic and adiabatic. Dynamic chirp refers to the

$\frac{1}{L}\partial L/\partial T$	$5.4 \cdot 10^{-6} K^{-1}$
$\partial n/\partial T$	$5.4 \cdot 10^{-6} K^{-1}$

Table 2.2: Temperature coefficients of InGaAsP lasers

change in frequency caused by a change in carrier density under current modulation. On the other hand, adiabatic chirp is a low frequency effect (including DC) which is a consequence of factors other than amplitude/phase coupling.

One of the most common causes of adiabatic chirp is a change in the laser temperature. As the injection current is varied, the temperature of the semiconductor laser is also varied due to resistive heating. This temperature change has two effects; a change in the cavity length and a change in the refractive index. For InGaAsP lasers operating at 1.5 μm, the corresponding coefficients are given in Table 2.2[5].

These coefficients lead to a frequency chirp of -11 GHz/K. This chirp is relatively constant at low frequencies however decreases above approximately 10 MHz due to the finite thermal conductivity of the semiconductor material. Another mechanism for adiabatic chirp is inhomogeneous current injection. These effects are discussed in Chapter 4.

Above the cutoff frequency adiabatic chirp, the effects of amplitude / phase coupling dominate the chirp. In order to model the dynamic chirp one can use the expression for $\tilde{\phi}(\Omega)$ (see Equation 2.18). Through the expression

$$\delta\dot{\phi} = \frac{1}{2\pi}\int_{-\infty}^{\infty} i\Omega\tilde{\phi}(\Omega)e^{i\Omega t}d\Omega \tag{2.57}$$

the dynamic chirp can be calculated ($\delta\omega = \delta\dot{\phi}$). Using the rate equations, modulation of the injection current C can be shown to lead to a variation in the carrier density given by [2]

$$\tilde{n}(\Omega) = \frac{(\Gamma_S + i\Omega)\tilde{C}(\Omega)}{(\Omega_r + \Omega - i\Gamma)(\Omega_r - \Omega + i\Gamma)} \tag{2.58}$$

Through a substitution of this expression into the equation for the phase deviation (Equation 2.18), the dynamic chirp can be obtained. For the case of sinusoidal modulation (i.e., $C(t) = C_o \sin\Omega_m t$), the (maximum) dynamic chirp is given as

$$\delta\omega = \frac{\alpha c_o G_N}{2e}\sqrt{\left[\frac{\Omega_m^2 + \Gamma_S^2}{(\Gamma^2 + \Omega_r^2 - \Omega_m^2)^2 + 4\Omega_m^2\Gamma^2}\right]} \tag{2.59}$$

It should be noted that the dynamic chirp is highly dependent upon the device structure and material used. Typical values for dynamic chirp in InGaAsP lasers operating at 1.3 μm are $1\mathring{A}$ for a 50 mA peak-peak modulation [4]. However, the use of multisection laser cavities which enable inhomogeneous current injection offer possibilities in achieving extremely low chirp lasers. It will be shown in Chapters 3 and 4 that composite cavity laser structures allow the laser to operate with reduced chirp, spectral linewidth, and frequency jitter.

References

[1] C.H.Henry, *Coherence, Amplification, and Quantum Effects in Semiconductor Lasers*, Edited by Y.Yamamoto, pp.5-76.

[2] G.Agrawal and N.Dutta, *Semiconductor Lasers*, Van Nostrand Reinhold, New York, 1993.

[3] G.Agrawal, *Fiber Optic Communication Systems*, John Wiley and Sons, New York, 1992.

[4] N.K.Dutta, N.A.Olsson, L.A.Koszi, P.Besomi, and R.B.Wilson, *J. Appl. Phys.*, vol.56, p.2167, 1984.

[5] C.H.Henry, *IEEE Journal of Quantum Electron.*, QE-19, p.1391, 1983.

[6] M.Lax, *Rev. Mod. Phys.*, vol.38, p.541, 1966.

[7] M.Lax, *Phys. Rev.*, vol.160, p.290, 1967.

[8] M.Lax, *IEEE Journal Quantum Electron.*,vol.QE-3, p.37, 1967.

[9] M.Lax, *IEEE Journal Quantum Electron.*,vol.QE-3, p.47, 1967.

[10] K.Petermann, *Laser Diode Modulation and Noise*, Kluwer Academic, Boston, 1992.

[11] Y.Yamamoto, *Coherence, Amplification, and Quantum Effects in Semiconductor Lasers*, John Wiley and Sons, New York, 1991.

[12] Y.Yamamoto, S.Machida, and O.Nilsson, *Phys. Rev. A*, vol.34, p.4025, 1986.

[13] J.Kitching, *Quantum Noise Reduction in Semiconductor Lasers using Dispersive Optical Feedback*, Ph.D. Thesis, California Institute of Technology, 1995.

[14] A.Yariv, *Quantum Electronics*, John Wiley and Sons, New York,1989.

[15] J.M.Iannelli, YShevy, J.Kitching, and A.Yariv, *IEEE Journal Quantum Electron.*, QE-29, p. 1993.

[16] K.Vahala and A.Yariv, *IEEE Journal Quantum Electron.*, QE-19, p.1096, 1983.

[17] K.Vahala and A.Yariv, *IEEE Journal Quantum Electron.*, QE-19, p.1102, 1983.

[18] K.Vahala. L.C.Chiu, S.Margalit, and A.Yariv, *Appl. Phys. Lett.*, vol.42, p.631, 1983.

[19] M.Ohtsu, *Highly Coherent Semiconductor Lasers*, Artech House, Boston, 1992.

[20] C.Harder, K.Valaha, and A.Yariv, *Appl. Phys. Lett.*, vol.42, p.328, 1983.

[21] A.L.Schawlow and C.H.Townes, *Phys. Rev.*, vol.112, p.1940, 1958.

[22] M.W.Fleming and A.Mooradian, *Appl. Phys. Lett.*, vol.38, p.511, 1981.

Chapter 3

Optical Feedback and Noise Reduction in Semiconductor Lasers

3.1 Introduction

Various methods have been proposed for reducing the spectral linewidths of semiconductor lasers. A common theme throughout many of these methods is an alteration of the loss function of the laser so as to provide negative feedback on the fluctuating phase. In particular, incorporating a dispersive (i.e., frequency dependent) loss mechanism in the laser cavity can lead to a dramatic quenching of the spectral linewidth. Ironically, the foundation upon which this technique relies is the α parameter which was previously shown to provide an additional contribution to the phase noise. Since amplitude changes are coupled with phase changes, a dispersive loss can be used to reduce the linewidth by producing changes in the field's amplitude and phase which correct for the initial phase fluctuation. The key quantities in the technique are the slopes of the loss rate and the accompanying refractive index with frequency. The proper slope produces negative feedback on phase fluctuations.

The dispersive loss technique can be implemented using various schemes of optical feedback, such as the reflection from an external cavity. The external feedback serves as a modification to the loss (gain) of the laser cavity. In an external cavity laser, one of the facets is used with an external mirror to compose a coupled-cavity system thereby rendering the facet's effective reflectivity (i.e., laser loss rate) frequency-dependent [1]. It is important to distinguish between internal and external losses. The external cavity can possess losses of its own but the loss that the active laser perceives will in general be quite different. In fact, in a traditional external cavity laser the external loss is comprised of solely dispersive phase changes where as the internal loss is a combination on dispersive phase and amplitude changes owing to the coupling of the fields at the laser facet. Both mechanisms have been shown to be instrumental in reducing the spectral linewidth.

There is a tradeoff, however, in ordinary external cavity systems between linewidth reduction and effective bandwidth. Relatively short cavities, having large effective bandwidths, can produce damping of the relaxation oscillations but leave much to be desired in terms of linewidth reduction [2]. In order to achieve substantial reduction in the spectral linewidth one needs to employ long cavities and operate at relatively high feedback levels. Such conditions often lead to either mode hopping or multimode operation due to the closely spaced external cavity modes [3].

A frequently used technique is the formation of an external cavity with a high-Q confocal Fabry Perot (CFP) cavity acting as a reflector [14]. This method performs quite well in terms of noise reduction and mode discrimination by "locking" the laser's frequency to the CFP reflection resonance. However, since the dispersive loss is related to the resonant reflection from the CFP cavity, variations in the locking frequency can occur from unavoidable thermal and mechanical instabilities.

In order to overcome the problem of instabilities and still maintain sufficient linewidth reduction and frequency discrimination, the diode laser can be frequency locked to an atomic transition within the external cavity geometry. A simplified diagram of this system is shown in Figure 3-1. An atomic cesium cell is placed between a pair of cross polarizers within an external cavity formed by a plane mirror. Utilizing the resonant Faraday rotation within the cell, reflected light is injected back into the diode laser only when the laser frequency is in close proximity (see section 3.2.4) of the atomic transition. Due to the small bandwidth of the reflection, small frequency variations in the laser field cause the dispersive loss to produce, in response, large changes in the field's amplitude and/or phase. These changes are then fed back to the diode laser via the external cavity.

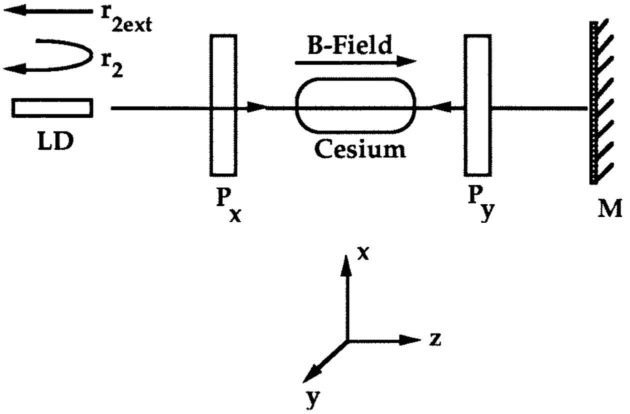

Figure 3-1: External cavity geometry employing faraday rotation in atomic cesium. LD:laser diode, M:external mirror, P:linear polarizer.

3.2 Theory of Dispersive Optical Feedback

3.2.1 Van der Pol Analysis

To describe the effects of the dispersive loss we follow a Van der Pol analysis in which the field intensity adiabatically follows the inversion density [16]. For calculations of spectral linewidth and chirp this assumption is justified. This analysis assumes that the loss is distributed internally within the laser cavity. Although the specific feedback mechanisms we will consider are external to the (active) cavity, this calculation can be shown to still provide the correct result through a rate equation analysis specific to this this system (see Appendix A).

We begin by writing the electric field as

$$E(t) = [A_o + \delta(t)] \exp i(\omega_m t + \phi(t)) \tag{3.1}$$

where A_o is the steady-state field amplitude, δ and ϕ are the small signal amplitude and phase ($< \phi >_t = 0$, in which $<>_t$ indicates temporal averaging), respectively, and ω_m is the lasing frequency. As shown in [16] the coupled rate equation for amplitude and phase is given by

$$2i\omega_m(\dot{\delta}+iA_o\dot{\phi})+\frac{2{A_o}^2\chi^{(3)}}{\mu^2}(2i\omega_m\dot{\delta}-{\omega_m}^2\delta)+({\omega_n}^2-{\omega_m}^2+i\frac{\omega_m}{\tau_p}-(\chi^{(1)}+{A_o}^2\chi^{(3)}\frac{{\omega_m}^2}{\mu^2})A_o = \Delta \tag{3.2}$$

where the complex susceptibility χ is expressed as a non-linear function of the lasing field by $\chi(E) = \chi^{(1)} + \chi^{(3)}|E|^2$. The cold cavity resonant frequency is given by ω_n, the nonresonant refractive index by μ, and the photon lifetime by τ_p. Δ is taken to be a Langevin noise source representing spontaneous emission see section 2.3.1. Following [17] the dispersive loss is modeled by a frequency-dependent loss rate as

$$\frac{1}{\tau_p} = \frac{1}{\tau_{po}} + 2C\dot{\phi} \tag{3.3}$$

where C is a constant representing the slope of the loss curve, and the instantaneous lasing frequency is given by $(\omega_m + \dot{\phi})$. Since corrections to the loss rate are taken to occur instantaneously, the results of this analysis are valid only for frequencies smaller than the inverse of the longest response time of the system.

This ansatz describes changes in the field's amplitude due to the dispersive loss but not changes in the field's phase. To further take into account the effects of phase changes in the loss rate, C is defined as a complex quantity given by $C = C_r + iC_i$. Using this form in Equation 3.3 we obtain a set of modified Van der Pol equations for the amplitude and phase

$$\dot{\delta} + \omega_1 \delta + A_o C_r \dot{\phi} = \frac{\Delta_i}{2\omega_1} \tag{3.4}$$

$$A_o(1 + C_i)\dot{\phi} - \alpha\omega_1 \delta = -\frac{\Delta_r}{2\omega_m} \tag{3.5}$$

where the quantities ω_1 and α are defined as

$$\omega_1 = -\frac{{\chi_i}^{(3)} {A_o}^2}{\mu^2}\omega_m \tag{3.6}$$

$$\alpha = \frac{{\chi_r}^{(3)}}{{\chi_i}^{(3)}} \tag{3.7}$$

In Equation 3.2 one can observe that the photon lifetime enters the rate equation on the same footing as the complex susceptibility. Therefore, the dispersive loss can be more naturally described through modifications in χ as opposed to a complex lifetime. Assuming the effects of the dispersive loss are well within the linear regime (i.e., ignoring the effects of saturation in the loss mechanism described through $\chi^{(3)}$)

we can substitute

$$\chi_r{}^{(1)} \;\Rightarrow\; \chi_r{}^{(1)} + \frac{2C_i\mu^2}{\omega_m}\dot{\phi} \tag{3.8}$$

$$\chi_i{}^{(1)} \;\Rightarrow\; \chi_i{}^{(1)} - \frac{2C_r\mu^2}{\omega_m}\dot{\phi} \tag{3.9}$$

We see that frequency-dependent amplitude and phase changes are described by C_r in $\chi_i{}^{(1)}$ and C_i in $\chi_r{}^{(1)}$, respectively. Physically, C_r represents a frequency-dependent loss and C_i a frequency-dependent refractive index change in the semiconductor laser cavity.

To calculate the field spectrum linewidth we first calculate the autocorrelation function of the phase. This is readily obtained through Laplace transformation of δ and ϕ in Equation 3.4 and 3.5 resulting in

$$< \phi(t_1)\phi(t_2) >= \frac{W}{4A_o{}^2\omega_m{}^2}\frac{(1+\alpha^2)}{(1+\alpha C_r + C_i)^2} min(t_1, t_2) \tag{3.10}$$

The field autocorrelation function is now written as

$$< E^*(t)E^*(t+\tau) >= A_o{}^2 \exp -\frac{< \phi^2(\tau) >}{2} \exp i\omega_m\tau + c.c. \tag{3.11}$$

where c.c. refers to the complex conjugate. After combining Equation 3.10 and Equation 3.11 and applying the Wiener-Khintchine theorem, we obtain a Lorentzian field spectrum with a spectral linewidth given by

$$\Delta\nu = \Delta\nu_{S.T.}\frac{(1+\alpha^2)}{(1+\alpha C_r + C_i)^2} \tag{3.12}$$

$$= \Delta\nu_{S.T.}\frac{(1+\alpha)^2}{Q^2} \tag{3.13}$$

where $\Delta\nu_{S.T.}$ is the Schawlow-Townes linewidth (see Equation 2.56) and $Q \equiv (1 + \alpha C_r + C_i)$. It should be stressed that C_r and C_i describe the frequency-dependent amplitude and refractive index changes within the diode cavity. These will be referred to as the internal dispersive losses. The above treatment therefore applies to an arbitrary laser configuration, one of which is the present scheme of external optical feedback.

As shown in Equation 3.13, the field corrections made by the dispersive loss are twofold. An initial phase fluctuation causes a frequency shift in the laser field. On one hand, the dispersive will behave as a frequency discriminator and produce, in response, an amplitude change in the field described by C_r. Through the α parameter this amplitude change corrects for the initial phase fluctuation. On the other hand, the frequency shift in the laser field will cause the dispersive loss to produce, in response, a phase change in the field which will directly correct for the phase fluctuation. This process is described by C_i. Either separately or in unison, the two mechanisms reduce the rate of phase diffusion thereby reducing the spectral linewidth. Although frequency-dependent amplitude and refractive index changes both play a role in linewidth reduction, amplitude changes are weighted more heavily (for

$\alpha > 1$) since C_r is multiplied by α.

3.2.2 Static Operating Conditions

In order to obtain expressions for C_r and C_i we need to investigate the operating conditions for our particular system. We must account for the coherent addition of an optical field from the external cavity to the complex amplitude $A(t)$ defined in Equation 2.2. This results in a modified version of Equation 2.3 (without the Langevin driving force) given as [5]

$$\dot{A}(t) = \frac{1 - i\alpha}{2}(G - \frac{1}{\tau_p})A(t) - i(\omega_m - \Omega)A(t) + \kappa A(t - \tau)e^{-i\phi} \tag{3.14}$$

where κ is the feedback coupling rate defined by

$$\kappa = \pi r / F\tau_d \tag{3.15}$$

with F and τ_d being the diode cavity finesse and roundtrip time, respectively, and r is the external cavity reflectivity. The external cavity phase shift is given by $\Phi = \omega_m \tau$, $\tau = 2L/c$, being the external cavity roundtrip time, and Ω is the lasing frequency without feedback.

The dispersive loss element in the external cavity is now modeled through a modification of κ and τ as

$$\kappa = \kappa(\omega) = \kappa(\omega_m) + \left.\frac{\partial\kappa}{\partial\omega}\right|_{\omega=\omega_m} \dot{\phi} \tag{3.16}$$

$$\tau = \tau(\omega) = \tau_o + \left.\frac{\partial\phi'}{\partial\omega}\right|_{\omega=\omega_m} \tag{3.17}$$

where ϕ' is the phase shift due to the cesium ($\Phi = \omega_m\tau_o + \phi'$) and now $\tau_o = 2L/c$.

Substituting Equation 3.17 into Equation 3.14 and separating real and imaginary parts yields

$$\dot{S}(t) = (G - \frac{1}{\tau_p}S(t) + 2\left[\kappa(\omega_m) + \frac{\partial\kappa}{\partial\omega}\dot{\phi}\right]\sqrt{S(t-\tau)S(t)}\cos\left[\Phi + \delta\varphi\right] \tag{3.18}$$

$$\dot{\phi}(t) = \frac{\alpha}{2}(G - \frac{1}{\tau_p}) - (\omega_m - \Omega) - \left[\kappa(\omega_m) + \frac{\partial\kappa}{\partial\omega}\dot{\phi}\right]\sqrt{\frac{S(t-\tau}{S(t)}}\sin\left[\Phi + \delta\varphi\right] \tag{3.19}$$

where $\delta\varphi = \varphi(t) - \varphi(t-\tau)$. In the steady-state these equations give the operating conditions for the stimulated emission rate (gain) as

$$\Delta G = G - \frac{1}{\tau_p} \tag{3.20}$$

$$= -2\kappa(\omega_m)\cos\Phi \tag{3.21}$$

and the lasing frequency as

$$\Delta\omega = \omega_m - \Omega \tag{3.22}$$

$$= -\kappa(\omega_m)\sqrt{1+\alpha^2}\sin\left(\Phi + \arctan\alpha\right) \tag{3.23}$$

With the exception of the additional phase shift from the cesium, ϕ' (contained in Φ), these equations are identical to those derived for an external cavity with no added losses.

Using the above results we can now obtain C_r and C_i for this system. Since the gain (loss) can be written as $G = \omega_m \chi_i / \mu^2$, C_r can be obtained from the slope of the loss curve as

$$\begin{aligned} C_r &= \left. \frac{1}{2} \frac{\partial(1/\tau_p)}{\partial\omega} \right|_{\omega=\omega_m} && (3.24) \\ &= \left. \frac{\partial\kappa}{\partial\omega} \right|_{\omega=\omega_m} \cos\Phi - \kappa(\omega_m)\tau(\omega)\sin\Phi && (3.25) \end{aligned}$$

To derive C_i, the phase shift in the laser diode is written as $\Delta\varphi = \omega_m \tau_c \chi r / 2\mu^2$. This phase shift can also be obtained intuitively from the vector model of the complex amplitude as $\Delta\varphi = \kappa\tau_c \sin\Phi$. Therefore, we find from Equation 3.8 that

$$\begin{aligned} C_i &= \left. \frac{\partial[\kappa(\omega)\sin\Phi]}{\partial\omega} \right|_{\omega=\omega_m} && (3.26) \\ &= \left. \frac{\partial\kappa}{\partial\omega} \right|_{\omega=\omega_m} \sin\Phi + \kappa(\omega_m)\tau(\omega_m)\cos\Phi && (3.27) \end{aligned}$$

As discussed above, C_r represents the frequency-dependent loss (internal) of the laser diode. It is seen in Equation 3.25 that not only does the external loss (cesium vapor) contribute through $(\partial\kappa/\partial\omega)_{\omega=\omega_m} \cos\Phi$ but the effect of coupling between the two cavities adds the term $\kappa(\omega_m)\tau(\omega)\sin\Phi$. Physically, this additional term represents the amplitude dependence on Φ obtained from summing the internal and external (feedback) electric fields at the laser facet. Similarly, the frequency-dependent refractive index in the laser cavity, represented by C_i, contains the contribution from the external cavity through $\kappa(\omega_m)\tau(\omega)\cos\Phi$ and the additional term $(\partial\kappa/\partial\omega)_{\omega=\omega_m}\sin\Phi$ due to the coupling of the internal and external fields.

Combining these results, we obtain for the all important Q factor

$$Q = 1 + \sqrt{1+\alpha^2}\left\{\kappa(\omega_m)\tau(\omega)\cos\left(\Phi + \arctan\alpha\right) + \left.\frac{\partial\kappa}{\partial\omega}\right|_{\omega=\omega_m}\sin\left(\Phi + \arctan\alpha\right)\right\} \tag{3.28}$$

3.2.3 Adiabatic Chirp Reduction

Amplitude to phase coupling in semiconductor laser manifests itself not only in enhancement of the spectral linewidth but also in FM generation under current modulation. Frequency changes due to changes in injection current (chirp) are a direct consequence of the α parameter but can be reduced by the dispersive loss mechanism. Using Equation 3.23 it is easily shown that the frequency chirp ($\Delta\omega$) due to changes in injection current (ΔE) is reduced by

$$\begin{aligned}
\frac{\partial\omega/\partial E}{\partial\Omega/\partial E} &= \frac{\partial\omega}{\partial\Omega} \\
&= \frac{1}{1 + \sqrt{1+\alpha^2}\left\{\kappa(\omega_m)\tau(\omega)\cos\left(\Phi + \arctan\alpha\right) + \left.\frac{\partial\kappa}{\partial\omega}\right|_{\omega=\omega_m}\sin\left(\Phi + \arctan\alpha\right)\right\}} \\
&= \frac{1}{1 + \alpha C_r + C_i} = \frac{1}{Q}
\end{aligned} \tag{3.29}$$

Similarly, we can determine the frequency chirp due to changes in cavity length as

$$\frac{\partial\omega}{\partial L} = -\frac{4\pi}{\lambda}\frac{\kappa(\omega_m)\tau(\omega)\cos\left(\Phi + \arctan\alpha\right)}{Q} \tag{3.30}$$

Therefore, the frequency locking stability of this system relative to an ordinary external cavity system is much better. As was verified experimentally, the reduction in frequency "jitter" can be more than an order of magnitude greater than that of a resonably sized external cavity (0.5 m).

3.2.4 Numerical Simulations of Dispersive Feedback

In order to investigate the characteristics of a semiconductor laser locked to the dispersive loss, one can numerically solve for various quantities as a function of the lasing frequency using the above equations. The approach of our algorithm is shown in Figure 3-2. Solutions to the frequency pulling equation 3.23 are shown graphically as the intersection of $(\omega - \Omega)$ and B(ω), the right-hand side of Equation 3.23. The gain at this frequency is compared to the gain without feedback ($\Delta G = 0$) and if it is less, lasing occurs at this frequency. In Figure 3-2 the gain condition is represented by the function $G(\omega)$. This function describes the difference between the required stimulated emission rate into the lasing mode with and without optical feedback (see Equation 3.21, where $G(\omega) = \Delta G$) necessary to obtain lasing (i.e., zero net gain). As would be expected, near the cesium resonance $G(\omega)$ becomes negative indicating that less stimulated emission is required to lase compared to the case of no optical feedback.

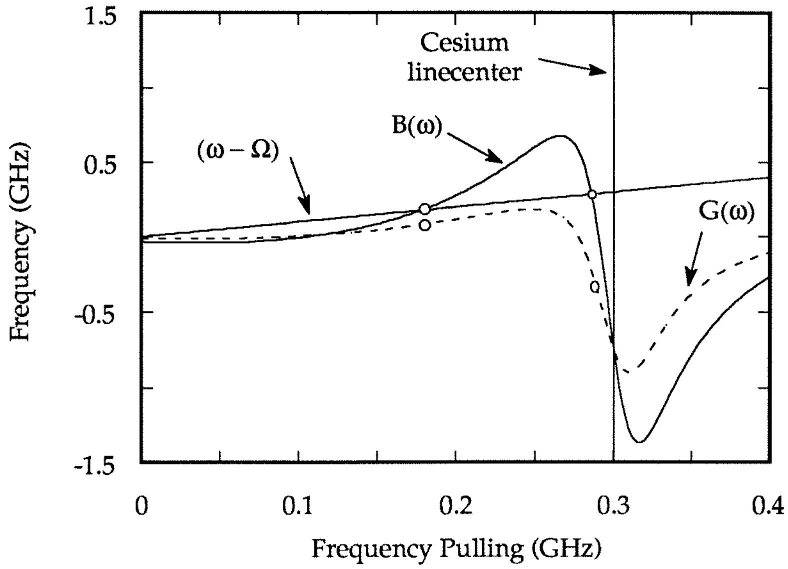

Figure 3-2: Graphical interpretation of the algorithm used in modeling a semiconductor laser locked to a dispersive loss. $B(\omega)$ equals the right-hand side of Equation 3.23 and $G(\omega)$ (dotted) equals the variation in gain given by Equation 3.21. Offset frequency $(\omega_o - \Omega) = 300$ MHz, where ω_o is the dispersive loss linecenter frequency, and κ_{max} = 1.0 GHz.

As a simplistic first-order model of the cesium dispersive loss we assume a four-level system in the presence of a uniform magnetic field (applied along the propagation axis). Although the actual ground state (F=4) and excited state (F=5) possess 9-fold and 11-fold degeneracies, respectively, we approximate both levels as being 2-fold degenerate. In addition to the dispersive loss, other factors in the external cavity affect the loss rate. These cavity losses include losses from optical components as well as losses due to the inefficiency of coupling the feedback field into the lasing mode.

Absorption in the atomic vapor is neglected in calculating the rotation but is taken into account in the cavity loss (including saturation effects). In Equation 3.14 the external cavity was characterized by a feedback coupling rate defined as $\kappa = \pi r / F \tau_d$ where r is the external mirror reflectivity, and a phase shift Φ. With the Faraday rotation we assumed κ to be frequency-dependent and added a phase shift ϕ' (due to the cesium) to Φ. We now take r and $\phi\prime$ as

$$\begin{aligned} r(\omega) &= \frac{\omega L_{Cs}}{c}(n_+ - n_-) & (3.31) \\ \phi'(\omega) &= \frac{\omega L_{Cs}}{c}\frac{(n_+ + n_-)}{2} & (3.32) \end{aligned}$$

where L_{Cs} is the length of the cesium cell, and n_+ and n_- are the refractive indices of σ_+ and σ_- circularly polarized light, respectively. This simple model ignores the basic phyical mechanisms which give rise to the doppler-free reflection. A full analysis of the multi-level system is provided in the Appendix.

Figure 3-3 shows the calculated quantities $\kappa(\omega)$ and $\phi'(\omega)$ as a function of frequency. As previously stated, κ is symmetric in frequency about the cesium linecenter while ϕ' is anti-symmetric. In the neighborhood of the linecenter, $(\partial \phi' / \partial \omega)_{\omega = \omega_m}$ is positive and relatively constant while $(\partial \kappa / \partial \omega)_{\omega = \omega_m}$ changes sign across the line. As discussed in [17], the sign of the slope of the loss curve determines whether the linewidth reduction or enhancement will occur. At first, one would expect reduction to be greater on the positive frequency side of $\kappa(\omega)$ (noting that κ actually behaves as a frequency-dependent gain to the diode rather than a loss). However, Equa-

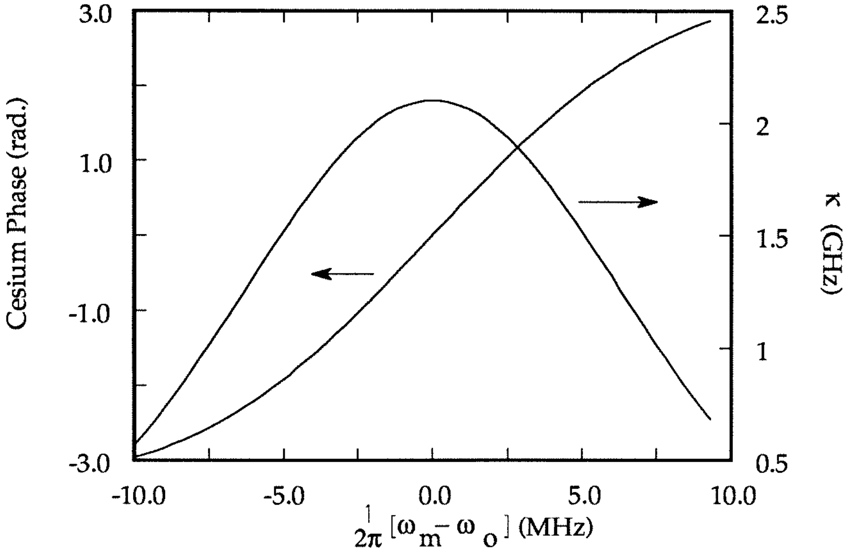

Figure 3-3: Cesium dispersive loss quantities $\kappa(\omega)$ and $\phi'(\omega)$ as calculated from the approximate model described in the text. Applied magnetic field = 1 G, temperature = 60°C, power broadened transition linewidth = 30 MHz, Output intensity = 50 mW/cm^2, Length of Cesium = 5 cm, Saturation Intensity = 1 mW/cm^2.

tion 3.28 shows that not only is the sign of $(\partial\kappa/\partial\omega)_{\omega=\omega_m}$ important but so is the sign of $\sin(\Phi + \arctan\alpha)$. Therefore, reduction can occur on either side of $\kappa(\omega)$ depending on the sign of the frequency pulling as defined in Equation 3.23.

We have considered the situation in which the lasing frequency is varied via a change in external cavity length. As shown in Equation 3.30, a variation in the on-axis position of the external mirror will pull the lasing frequency away from ω. This behavior is used to scan the lasing frequency over the dispersive loss to observe the noise reduction. In addition to frequency pulling, we now define an offset frequency as the difference between the atomic cesium linecenter and the lasing frequency without feedback, i.e., $(\omega_o = \Omega)$. This quantity is shown to be important in determining the

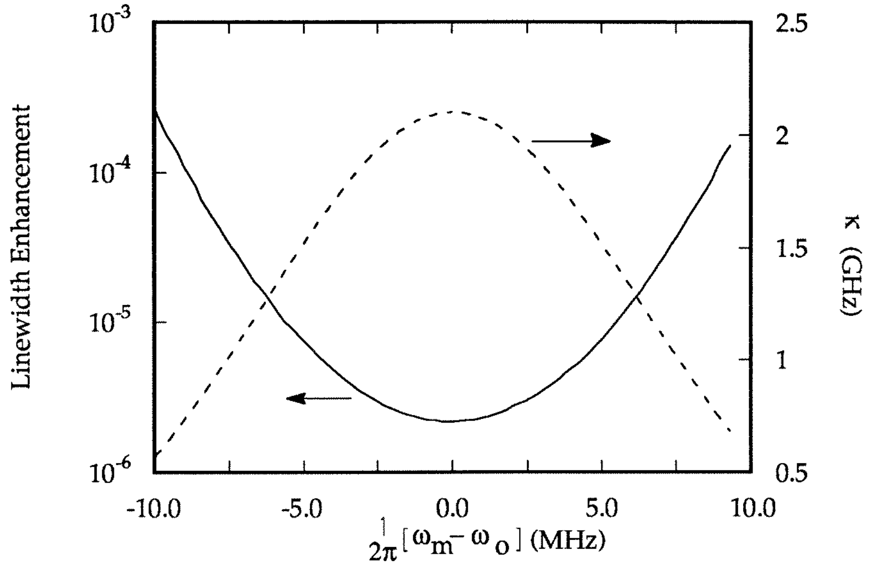

Figure 3-4: Linewidth enhancement and feedback coupling rate $\kappa(\omega)$ versus lasing frequency. Offset Frequency = 0 MHz, κ_{max} = 2.1 GHz.

different roles of C_r and C_i in the noise reduction process.

In Figure 3-4 the linewidth enhancement and the amplitude of the feedback field are plotted versus the lasing frequency. As shown in the figure, the linewidth reaches a minimum when lasing is at the top of the dispersive line. At this point the refractive index changes in the external loss are maximum while the amplitude changes are minimum. As discussed in [2] for the case of locking to a high-Q CFP cavity, the phase corrections from the cesium can be viewed as increasing the effective time constant of the feedback system. Since the dispersive loss can be very narrow in our technique ($\approx$17 MHz bandwidth measured for the Doppler-free reflection [9]), under our operating conditions $(\partial\phi'/\partial\omega)_{\omega=\omega_m}$ can be much larger and in fact dominate

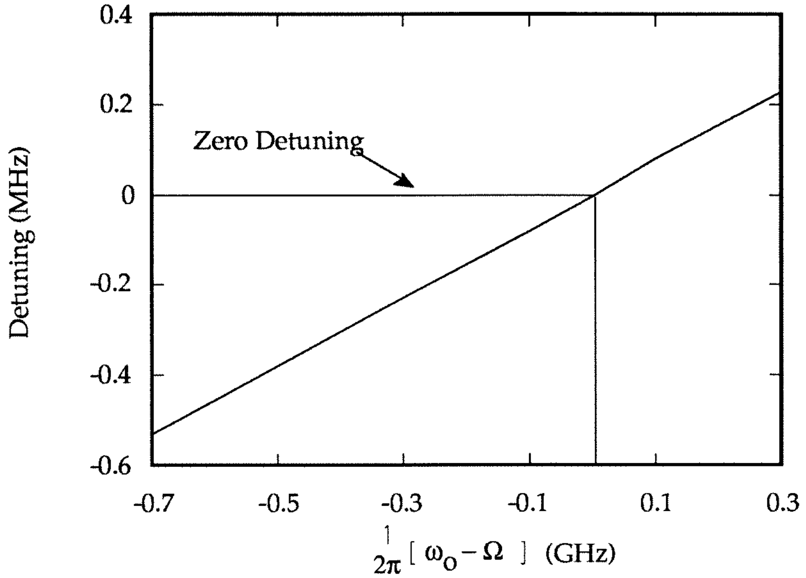

Figure 3-5: Position of minimum linewidth relative to the cesium linecenter as a function of offset frequency. The position of zero detuning is marked on the graph. $\kappa_{max} = 2.1$ GHz.

in the expression for $\tau(\omega)$. In contrast to the ordinary external cavity laser, this system relies more on the frequency dependence of the optical feedback than on its magnitude. It can therefore produce large reduction at low feedback levels alleviating the problems of mode hopping.

Although the dominant effect in the reduction process is seen to be the frequency-dependent refractive index changes in the external loss, the amplitude changes described through $(\partial\kappa/\partial\omega)_{\omega=\omega_m}$ can also play a role. In Figure 3-5 the position of minimum linewidth relative to the cesium linecenter (detuning) is plotted as a function of offset frequency. At large offset frequencies minimum linewidth operation occurs slightly to the side of the dispersive loss linecenter indicating that amplitude

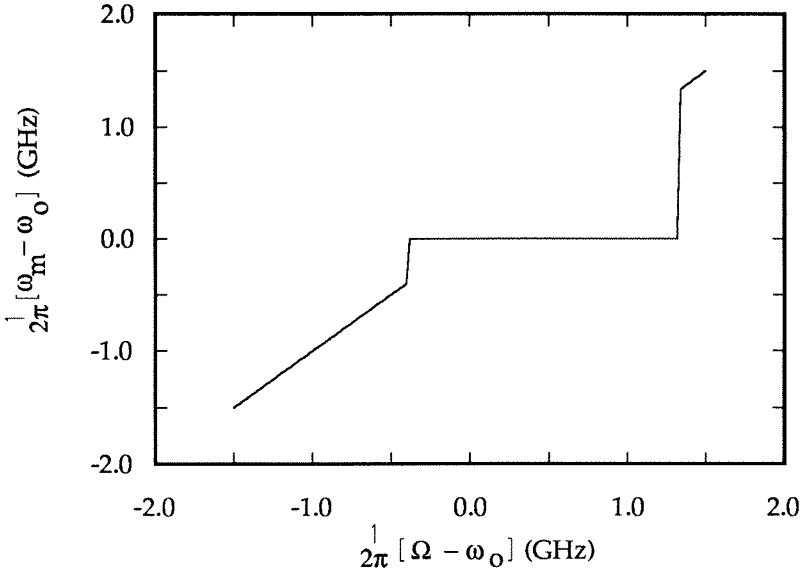

Figure 3-6: Reduction in adiabatic chirp. Chirp reduction is given by the slope of the curve. Both frequencies are relative to the dispersive loss linecenter frequency, ω_o.

changes are now contributing to the reduction.

In addition to linewidth reduction, frequency stability with respect to changes in injection current (chirp) is also improved using the dispersive loss. In Figure 3-6 we show the actual lasing frequency ω_m plotted as a function of the lasing frequency without feedback, Ω. From the figure we see that if the lasing frequency is far from the cesium linecenter it follows the injection current as if there were no feedback present. However, in the neighborhood of the dispersive loss (in this case, within approximately 10-20 spectral bandwidths of the cesium resonance) the frequency locks and the chirp is reduced by $1/Q$. In addition, the chirp reduction is seen to be maximum near the top of the cesium line as would be expected from Equation 3.29.

3.3 Experimental Results on Linewidth Reduction Using Dispersive Optical Feedback

As discussed previously, the atomic transition in cesium at 852.1nm is used as a frequency reference and discriminator in the optical feedback system. This particular transition is useful for a variety of reasons. Its oscillator strength is one of the largest of all the existing transitions in atomic cesium. Moreover, 852.1 nm is in relative proximity to the lasing wavelengths of commercially available lasers. Precise tuning of the laser's frequency to the transition energy can be accomplished via injection current and temperature means.

One potential drawback of utilizing an atomic vapor as a frequency reference is the effect of doppler broadening on the feedback bandwidth. An effective method of circumventing these limitations is to use an overlapping and counter-propagating pump/probe beam arrangement. A sufficiently strong pump beam can selectively bleach the absorption and refractive index which are then detected with the weak probe beam (see Appendix B).

3.3.1 Experimental Apparatus

As shown in Figure 3-1, a cesium cell is placed between two crossed polarizers each having an extinction ratio of $1 : 10^4$. The length of the cesium cell used was 5 cm and its temperature was maintained at 50 ^oC. The applied axial magnetic field is applied through a pair of Helmholtz coils with a uniformity across the cell of 2 percent. The external cavity is formed by the laser's output facet and a mirror placed 40.5 cm away. The laser used was a Hitachi HLP1400 CSP (channel substrate planar) Fabry-Perot laser. It was operated at 120 mA ($i_{threshold} = 58$ mA) with an output power of 12.5 mW and a collimated spot size of $0.25cm^2$.

This arrangement produced a Doppler-free reflection with a FWHM of 17 MHz utilizing the $F = 4 \rightarrow F' = 5$ transition at 852.1 nm. The phase of the feedback field was controlled by means of a piezoelectric transducer upon which the back mirror was mounted. The magnitude of the feedback was varied through the use of a continuously variable neutral density filter. The highest level of feedback attained for the Doppler-free signal was -35 dB utilizing a magnetic field of 1 Gauss. At larger magnetic fields, the reflection became broader with a FWHM of approximately 200 MHz. A 30 percent beam splitter was inserted within the cavity for monitoring the field spectrum and measuring the spectral linewidth. Spectral linewidths were measured in one of two ways. For linewidths of approximately 1 MHz and larger, a scanning Fabry-Perot interferometer was employed. The cavity finesse was ≈ 10,000 and the free spectral range was 6 GHz yielding a resolution of approximately 600 kHz. For smaller linewidths, a self-delayed heterodyne measurement was used [8] (see Figure 3-7. In this technique, the optical field is split into two components, one component is delayed for a time longer than the laser's coherence time, and the two are then recombined. Since the two signals are phase incoherent with each other, heterodyne detection can be carried out. A 5 km length delay line was used in these experiments which yielded a measurement resolution of 6.4 kHz.

3.3.2 Linewidth Reduction

With the application of optical feedback, the spectral linewidth is dramatically reduced below its solitary (i.e., without external feedback) value. A maximum reduction of a factor of 2000 was measured from $\Delta\nu = 20$ MHz to $\Delta\nu = 10$ kHz (see Figure 3-8). While this is a substantial reduction, it is far below what would be predicted from Equations 3.13 and 3.28. For the feedback conditions used, the theory predicts a reduction by a factor of 10^6. Such a discrepency cannot be explained by the limited resolution of the measurement apparatus. In Figure 3-8 the beat note spectra are plotted for two different feedback configurations. Curve (a) represents the minimum linewidth obtainable with this arrangement ($\Delta\nu = 10$ kHz). Curve (b) is the spectrum of simply utilizing the external cavity without the cesium; i.e., a simple external cavity laser with identical length as that in curve (a). From this figure two points are evident. First, the cesium arrangement is clearly superior in linewidth reduction compared to the external cavity. This can be shown using the theory described above. However, more important is the functional dependence of the spectra. Equation 3.11 gives the autocorrelation spectrum of the electric field of the laser. From this expression in can be easily shown that the field spectrum is a Lorentzian function. However, the dashed and solid fits of the data shown in Figure

3-8 represent curve fits to a Lorentzian function and a Lorentzian function raised to the 3/2 power, respectively. For narrow linewidths (a quantitative criterion is given in [6]), the laser field spectrum is described by a Lorentzian$^{3/2}$ function rather than a Lorentzian. The explanation of this lies in the dominating source of frequency noise. As alluded to briefly in Chapter 2, the source of frequency noise is usually taken as spontaneous emission events which produces a white noise spectrum at frequencies below the relaxation resonance frequency. However, at low frequencies ($\approx$ 10MHz and below) the dominant noise source is often one which produces a $1/f$ characteristic [10,11,12]. There have been various postulates on the origin of this noise source in semiconductor lasers, one of which is temperature fluctuations [13].

Regardless of the source of $1/f$ noise, its effects on the laser field spectrum under the influence of optical feedback can be determined (for a complete treatment of these effects, the reader is referred to [6]). It can be shown that for a semiconductor laser whose frequency noise spectrum is dominated by spontaneous emission, the frequency noise is reduced by optical feedback as

$$S_{\dot{\phi}}(\Omega) = \frac{S^{o}_{\dot{\phi}}(\Omega)}{Q^2} \tag{3.33}$$

where Q is the noise reduction factor defined in Equation 3.28 and $S^{o}_{\dot{\phi}}(\Omega)$ is the frequency noise spectrum without external feedback. This is simply a restatement of the results presented above. It is irrespective of the type of noise source. However, when the field spectrum is calculated for the case of white noise and $1/f$ noise, it is found that [6]

$$\Delta\omega_{white} = S_{\dot{\phi}}(\Omega) \tag{3.34}$$

$$\Delta\omega_{1/f} = \sqrt{\frac{S_{\dot{\phi}}(1)}{\pi}} \tag{3.35}$$

Therefore, in lasers dominated by $1/f$ noise, optical feedback is not as effective as it is in lasers dominated by white noise. Furthermore, calculations show that the field spectrum behaves as Lorentzian and Lorentzian$^{3/2}$ for white noise and $1/f$ noise, respectively [6].

Since the linewidth is reduced as the square root of $S_{\dot{\phi}}$, $\Delta\nu$ should be reduced as $1/Q$. In order to verify the $1/Q$ dependence of the spectral linewidth for narrow linewidth semiconductor lasers dominated by $1/f$ noise, one can measure the linewidth reduction with respect to feedback power. From Equation 3.28 the linewidth reduction factor Q depends inversely on the quantity κ. From Equation 3.15 in can be further seen that Q depends inversely on the square root of the feedback power since the reflectivity r in the expression for κ is an *amplitude* reflectivity. In Figure 3-9 is plotted the inverse of the spectral linewidth versus [feedback power]$^{1/2}$. As shown, linewidth reduction behaves as $1/Q$ as predicted. It should be noted that for larger linewidths, the reduction would return to a $1/Q^2$ dependence.

The two curves in Figure 3-9 also show the effectiveness for linewidth reduction of the cesium arrangement versus the external cavity. Curve (a) was taken for the cesium arrangement with the lasing frequency at the cesium linecenter. The frequency dependent losses will therefore be purely phase losses since $\partial\kappa/\partial\omega = 0$ at linecenter. From the slope of these two curves one can determine the factor $(\partial\phi'/\partial\omega + \tau)$ for both cases. In the external cavity this quantity is simply equal to τ. For the cesium arrangement curve (a) yields a value of $(\partial\phi'/\partial\omega + \tau)/\tau = 16 \pm 1$. As discussed in [2], the effects of the cesium can be thought of as an "effective" delay which in this case is a factor of 16 more than the empty external cavity delay τ.

In order to independently confirm the value of $(\partial\phi'/\partial\omega + \tau)$, one can perform a measurement of the frequency pulling as a function of the external mirror position (through a modulation of the piezoelectric voltage). From Equation 3.23 it is straightforward to show that

$$\frac{\partial\omega}{\partial\Phi} = \frac{\sqrt{1+\alpha^2}\kappa(\omega)}{1+\sqrt{1+\alpha^2}(\partial\phi'/\partial\omega+\tau)\kappa(\omega)} \tag{3.36}$$

From this measurement we obtain a value of $(\partial\phi'/\partial\omega + \tau)/\tau = 13 \pm 2$ which is within one standard deviation of the previous result.

To further show that the frequency-dependent dispersion of the cesium resonance is the primary contributor to the Q factor, we measured the laser linewidth as a function of the detuning of the lasing frequency from the cesium linecenter. In all measurements zero frequency pulling was maintained (see Equation 3.23). In Figure 3-10, the linewidth is plotted as a function of the detuning from linecenter as is the quantity $\Delta\nu\kappa^{-1}$. Curve (a) shows that indeed the minimum linewidth occurs at the linecenter of the cesium. However, this could be not only as result of the

$(\partial\phi'/\partial\omega + \tau)$ factor in Q but also a result of the reduction of $\kappa(\omega)$ as one moves off linecenter. Therefore, in curve (b) is plotted $\Delta\nu\kappa^{-1}$ which should eliminate the effects of a varying $\kappa(\omega)$ in the measurement. If the effects of linewidth reduction were solely due to the feedback amplitude curve (b) would be a constant. However, curve (b) agrees with a derivative of a dispersive lineshape which has been derived from a Lorentzian $\kappa(\omega)$. It is also worth noting that at nonzero frequency pulling the frequency dependent amplitude effects also contribute to the phase effects. In fact it has been found that a small frequency pulling such that lasing was slightly off linecenter gave rise to a 30 percent improvement in linewidth reduction.

3.4 Conclusions

In summary, a Van der Pol analysis has been carried out for a semiconductor laser with dispersive loss. To account for both amplitude and phase changes induced by the external loss mechanism, the internal laser loss rate is modeled through modifications to the complex susceptibility. It is shown that the linewidth reduction behaves as $1/Q^2$ where Q is a factor defined in terms of the geometry-specific operating conditions of the semiconductor laser. In addition, adiabatic chirp is shown to decrease as $1/Q$. Although the analysis assumes the loss to be uniformly distributed throughout the laser, the results for linewidth reduction are also correct if the loss is introduced through a form of external feedback, as is the case in our method. This validity of the Van der Pol analysis is shown by carrying out the calculation using the rate equations specific for our external loss (see Appendix A). Using an approximate model of the cesium dispersive loss, we calculated linewidth reduction and chirp reduction as a function of lasing frequency. The dominant mechanism of noise reduction was found to be the frequency-dependent phase changes produced by the atomic vapor. However, under certain operating conditions, the vapors frequency-dependent amplitude changes were also shown to play a role in the reduction process.

An experimental arrangement of external feedback utilizing faraday rotation in an atomic cesium vapor was investigated. Frequency noise reduction well below the Schawlow-Townes limit for a solitary laser is demonstrated. Our analysis indicates that the quantum limit of the linewidth as a sole result of spontaneous emission is reduced by a factor of 10^6. However, owing to the important contribution of $1/f$ noise, the reduction of the laser linewidth is only by a factor of 2000. It was demonstrated that the operative mechanism in this dramatic effect is primarily the concerted action of frequency-dependent internal loss and amplitude / phase coupling. An additional, smaller contribution is due to internal frequency-dependent dispersion.

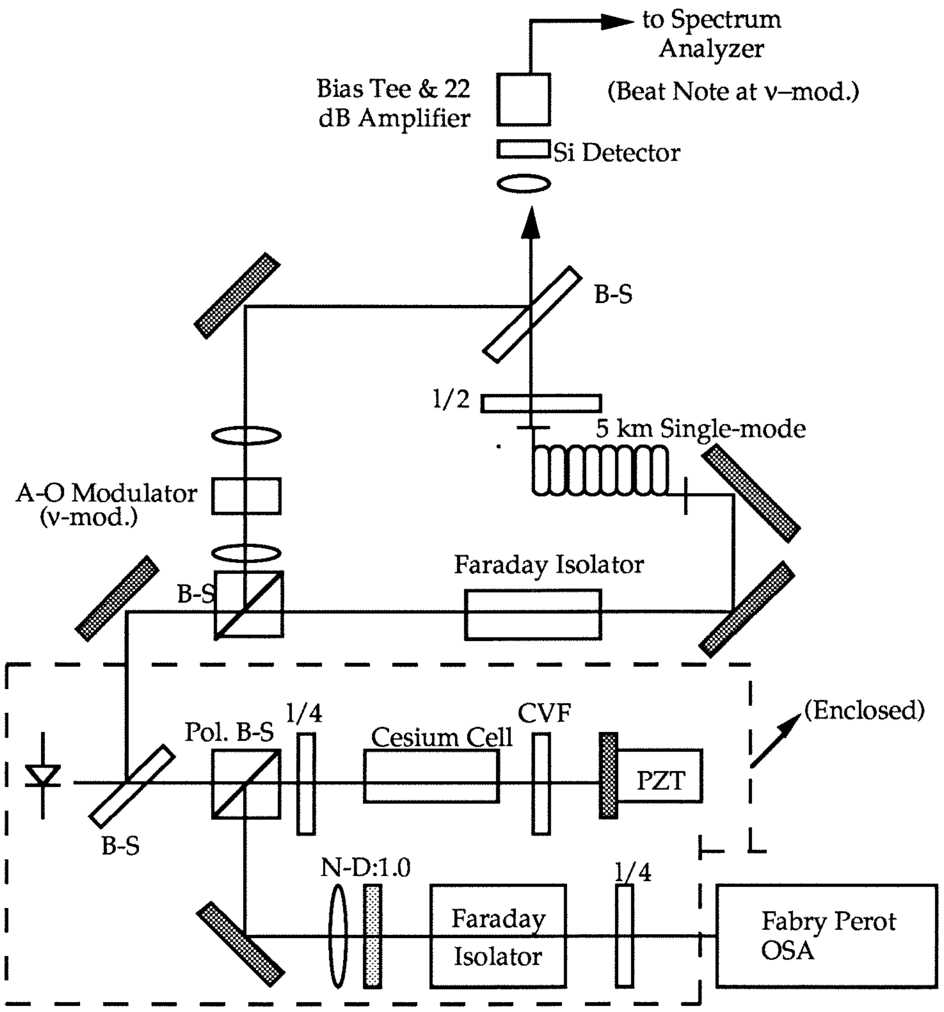

Figure 3-7: Experimental set-up for measuring spectral linewidth using a self-delayed heterodyne detection scheme.

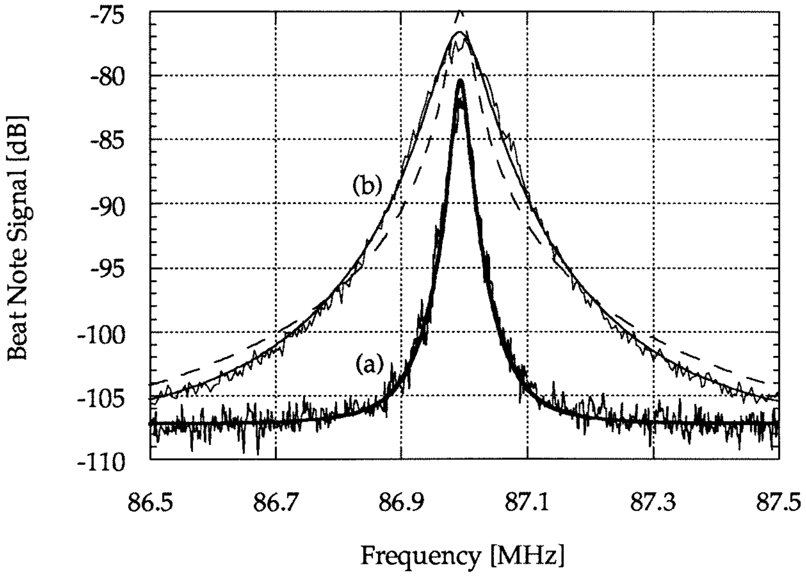

Figure 3-8: Beat note spectrum with the self-delayed heterodyne measurement scheme. Curve (a) is the minimum linewidth obtained, with the solid curve being the best fit to a Lorentzian raised to the power 1.5. Curve (b) is another beat note spectrum with the dashed curve being a best fit to a Lorentzian lineshape.

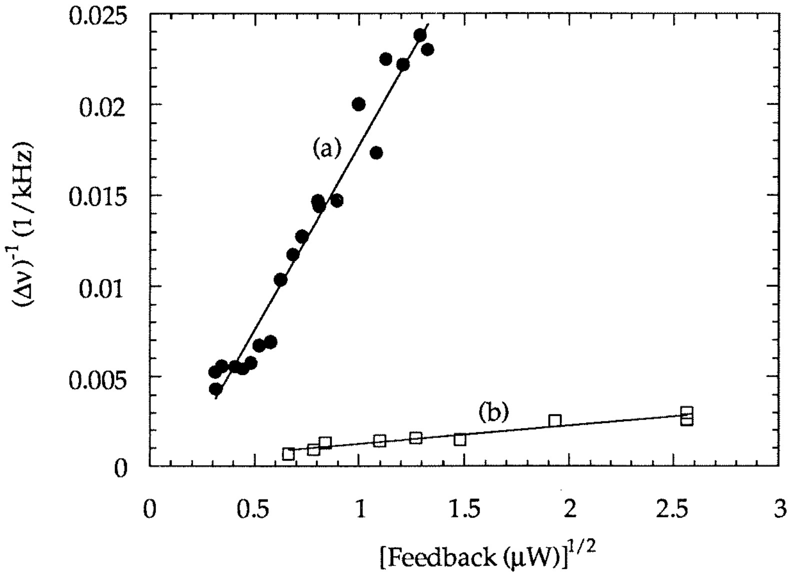

Figure 3-9: $1/\Delta\nu$ as a function of the square root of the feedback level with the linewidth measured at the top of the Faraday signal with zero frequency pulling (curve (a)) and an empty cavity (curve (b)).

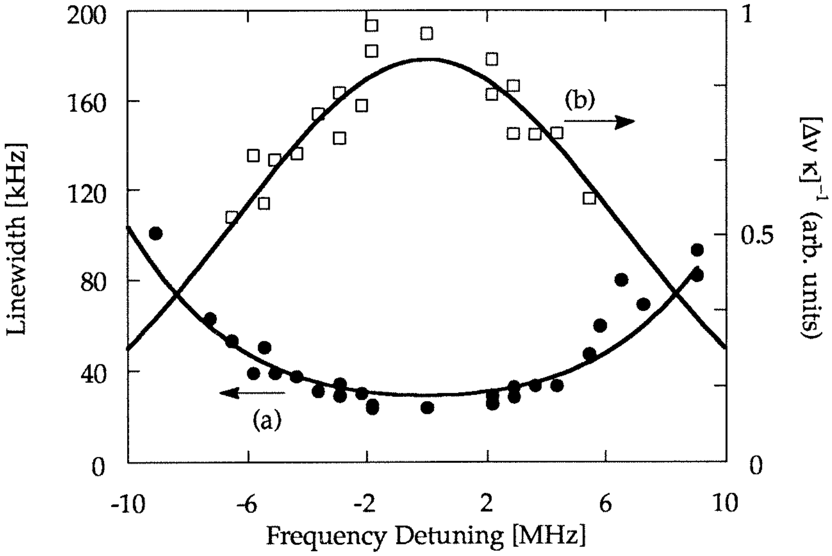

Figure 3-10: Points on curve (a), the laser linewidth as a function of detuning from the peak of the Faraday signal. Points on curve (b), $[\Delta\nu\kappa(\omega)]^{-1}$ as a function of detuning; the solid curve is a fit to a derivative of a dispersive lineshape.

References

[1] R.Lang and K.Kobayashi, *IEEE J. Quantum Electron.*, vol.QE-16, p.347, 1980.

[2] D.R.Hjelme, A.R.Mickelson, and R.G.Beausoleil, *IEEE J. Quantum Electron.*, vol.QE-27, p.352, 1991.

[3] L.Goldberg, H.Taylor, A.Dandridge, J.Weller, and R.O.Miles, *IEEE J. Quantum Electron.*, vol.QE-18, p.555, 1982.

[4] B.Dahmani, L.Hollberg, and R.Drullinger, *Opt. Lett.*, vol.12, p.876, 1987.

[5] G.P.Agrawal, *IEEE J. Quantum Electron.*, vol.QE-20, p.468, 1984.

[6] J.Kitching, Y.Shevy, J.Iannelli, and A.Yariv, *J. Lightwave Technol.*, vol.11, p.1526, 1993.

[7] J.Iannelli, Y.Shevy, J.Kitching, and A.Yariv, *IEEE J. Quantum Electron.*, vol.QE-29, p.1253, 1993.

[8] T.Okoshi, K.Kikuchi, and A.Nakagama, *Electron. Lett.*, vol.16, p.630, 1980.

[9] Y.Shevy, J.Iannelli, J.Kitching, and A.Yariv, *Opt. Lett.*, vol.17, p.661, 1992.

[10] C.M.Van Cliet, *Solid State Elec.*, vol.34, p.1, 1991.

[11] M.S.Keshner, *Proc. IEEE*, vol.70, p.212, 1982.

[12] F.N.Hooge, T.G.M.Kleinpenning, and L.K.J.Vandamme, *Rep. Prog. Phys.*, vol.44, p.479, 1981.

[13] R.Lang, K.J.Vahala, and A.Yariv, *IEEE J. Quantum Electron.*, vol.QE-21, p.443, 1985.

[14] B.Dahmani, L.Hollberg, and R.Drullinger, *Opt. Lett.*, vol.12, p.876, 1987.

[15] Ph.Laurent, A.Clarion, and Ch.Breant, *IEEE J. Quantum Electron.*, vol.25, p.1131, 1989.

[16] K.Vahala and A.Yariv, *IEEE Journal Quantum Electron.*, QE-19, p.1096, 1983.

[17] A.Yairv, R.Nabiev, and K.Vahala, *Opt. Lett.*, vol.15, p.1359, 1990.

Chapter 4

Modulation Properties of Multisection Distributed Feedback Lasers

4.1 Introduction

In recent years, distributed feedback (DFB) lasers have enjoyed widespread application in the field of optical communications. Their applicability is due in large part to their unique spectral characteristics such as wavelength tunability [1], narrow spectral linewidth [2], and large side mode suppression [3]. Many of these attributes of DFB lasers have been improved upon through the use of multi-electrode structures which enable nonuniform current injection [5]. The introduction of a longitudinal variation in injection current is frequently used as a means of controlling the unavoidable axial variation in carrier density attendant upon the optical intensity variation, a phenomenon known as spatial hole burning [4]. Additionally, nonuniform current injection is often employed in multielement lasers for purposes of frequency tuning.

The ability to tune the lasing frequency in a multisection laser can be understood from the fact that the gain in any individual section is no longer fixed at threshold as in a single element device. Since the gain (and therefore the carrier density) is not fixed, neither is the refractive index thus leading to frequency tuning. This interplay between the gain and the refractive index is mediated by the α parameter. In a multisection laser, different injection current densities in different sections can lead to a low frequency (including DC) tuning sometimes referred to as adiabatic chirp. This phenomenon has been predicted on the basis of nonequal effective α parameters in multisection lasers [6].

4.2 Wavelength Tunability

One of the unique characteristics of multi-section DFB lasers is the ability to tune the lasing wavelength through current injection. As previously mentioned, the gain in an individual isolated section of the laser cavity need not be clamped as opposed to a single section laser. The only gain condition that must be met is the roundtrip gain being equal to unity. Since the gain may vary with injection current, the refractive index may vary accordingly since the two are coupled through the α parameter. These effects can produce wavelength tuning as well as wavelength switching.

In order to study these effects more quantitatively, one can calculate the roundtrip gain spectrum as a function of injection current distribution. Here, we only briefly outline the salient points of the calculation. For further details, the reader is referred to [20].

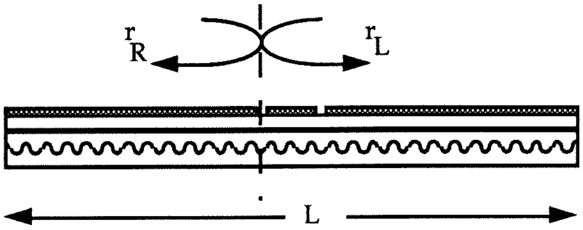

Figure 4-1: Model used for the calculation of DFB laser characteristics. The position of the reference plane shown (dashed line) is arbitrary.

The starting point for the analysis of threshold conditions, gain, wavelength tunability, etc., is the coupled mode equations. These equations can be written as

$$\frac{da}{d\zeta} = \left[\tilde{\gamma}(\zeta) - i\Delta\tilde{\beta}(\zeta)\right] a(\zeta) + \left[\tilde{\kappa}_n(\zeta) - i\tilde{\kappa}_\sigma(\zeta)\right] e^{-i\phi(\zeta)} b(\zeta) \tag{4.1}$$

$$\frac{db}{d\zeta} = \left[\tilde{\kappa}_n(\zeta) - i\tilde{\kappa}_\sigma(\zeta)\right] e^{+i\phi(\zeta)} a(\zeta) - \left[\tilde{\gamma}(\zeta) - i\Delta\tilde{\beta}(\zeta)\right] b(\zeta) \tag{4.2}$$

where the complex amplitudes of the forward and backward propagating fields are written as

$$E_F(z) = a(z)e^{-i\beta_o z} \tag{4.3}$$

$$E_B(z) = b(z)e^{+i\beta_o z} \tag{4.4}$$

In this notation, $\tilde{\zeta} = z/L, \tilde{\gamma} = \gamma(\zeta)L$ (where γ is the net amplitude gain), $\Delta\tilde{\beta}(\zeta) = \Delta\beta(\zeta)L$, and $\tilde{\kappa}_n(\zeta) = \kappa_n(\zeta)L$ ($\tilde{\kappa}_\sigma(\zeta) = \kappa_\sigma(\zeta)L$) are the normalized index (loss) coupling coefficients. These equations are now solved using a transfer matrix approach

[20]. The lasing condition requires that the roundtrip gain G be equal to unity (as well as a total phase shift be a multiple of 2π) which can be obtained by calculating the right and left reflection coefficients from a reference plane (see Figure 4-1) as

$$r_L = \frac{E_F^L(\zeta_o)}{E_B^L(\zeta_o)} \quad ; \quad r_R = \frac{E_B^R(\zeta_o)}{E_F^R(\zeta_o)} \tag{4.5}$$

The threshold condition now becomes

$$G(\omega, J) = r_L(\omega, J) r_R(\omega, J) = 1 \tag{4.6}$$

If one solves for the lasing condition, one obtains the gain and phase data as shown in Figure 4-2. In this figure the two lasing solutions are degenerate since the grating is uniform (without any phase shifts) as are the facet reflectivities and phases. In a typical DFB laser, this ideal "symmetry" would be broken by irregularities in the facet reflectivities and phases leading to single mode oscillation.

With this model of a DFB laser, one can investigate the effects of non-uniform current injection on the gain and lasing wavelength. For a test structure, we consider a three section DFB laser with the properties shown in Table 4.1.

The test laser is composed of three sections with lengths of 200 μm, 100 μm, and 200 μm symmetric about the center of the cavity (see inset of Figure 4-3). The two end sections are pumped equally while the center section is overpumped as well as underpumped with respect to the uniform pumping condition. As shown in Figure

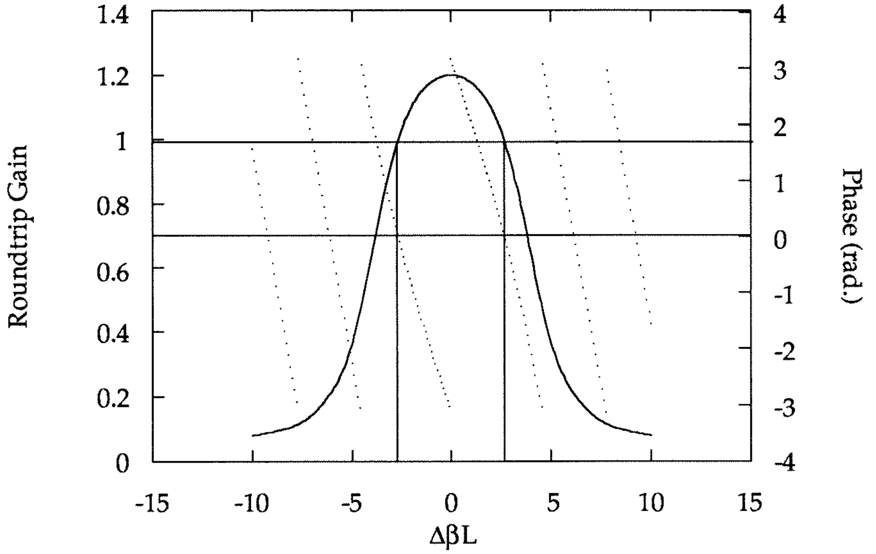

Figure 4-2: Calculated roundtrip gain and phase for a three section DFB laser with lengths of 200 μm, 100 μm, and 200 μm. Facet reflectivities = 0.0. Further model parameters are given in Table 4.1.

4-3, the variation in the injection current distribution causes a shift in the roundtrip gain spectrum thereby leading to a shift in the lasing mode wavelength. From the calculations shown one sees that overpumping the center section above the uniform condition leads to a selection of the negative degenerate mode of the DFB structure as well as a shift towards the stopband center. The exact opposite holds true for the underpumped case. Figure 4-4 shows the shift in the lasing mode as a function of the center section injection current. The amount of current in the center section is given as the ratio of the current *density* in the center section to that in either one of the two end sections (i.e., J_2 / [J_1 or J_3]).

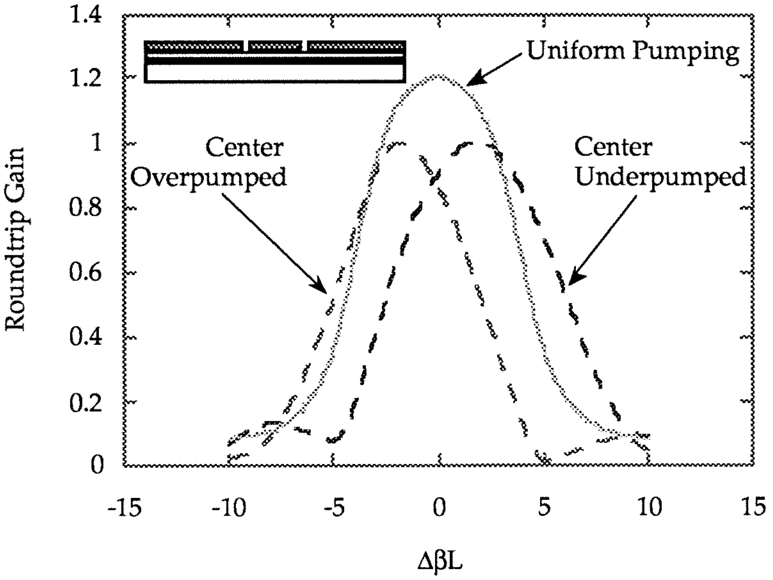

Figure 4-3: Roundtrip gain as a function of nonuniform injection current. The overpumped and underpumped conditions refer to R=1.2 and R=0.8 in Figure 4-6, respectively.

In addition to the changes in gain and lasing wavelength, altering the injection current obviously changes the optical power distribution in the cavity. This power distribution is given by [20]

$$P(\zeta) = P_F(\zeta) + P_B(\zeta) + 2C^2 Re\left[E_F(\zeta)E_B^*(\zeta)\right] \qquad (4.7)$$

where $P_{F,B}(\zeta)$ represent the forward and backward propagating power, respectively, and the last term represents the power in the standing wave. For the parameters used in the calculation above (see Table 4.1), one can calculate the power

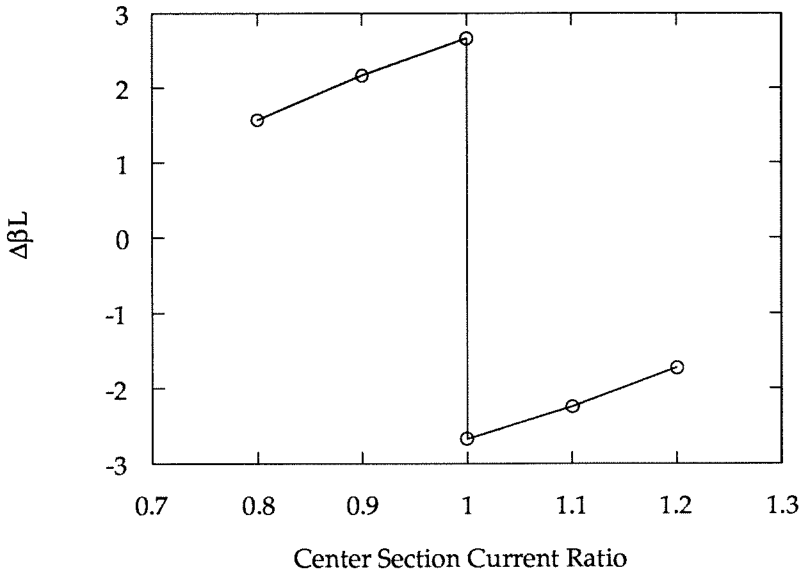

Figure 4-4: Shift in $\Delta\beta L$ of the lasing mode with nonuniform injection current. Current ratio is defined as in the ratio of center section current density to either end section current density.

distribution along the axis of the cavity. These distributions are shown in Figure 4-5. As before, one can investigate the effects of overpumping and underpumping the center section. In Figure 4-6 the power distribution is shown for uniform, underpumped, and overpumped conditions as in Figure 4-3. It is shown that for the overpumped condition, the optical power distribution is more (axially) uniform compared to either of the other two conditions. It has been suggested that these effects could be partly responsible for the linewidth saturation observed in the $1/<S>$ functional dependence. Such effects have been investigated in DFB lasers with inhomogeneous current injection with preliminary results showing confirmation [4].

Wavelength	1.3 μm	κL	1.0
L	500μm	Diff. Gain	1.0E16
r_1, r_2	0.0	α	5.0
βL	16640	Diff. index	0.0048
N_{trans}	2.5E18	α_{loss}L	4.0

Table 4.1: Parameters used in the modeling of three-section DFB laser

4.3 Dynamic Properties: Modulation and Chirp Analysis

In order to model the spectral dynamics of a multi-element semiconductor laser we follow the treatment found in Ref. [6]. The laser rate equations are expanded in the small signal regime about their steady-state operating conditions as in Chapter 2. However, unlike the treatment of laser noise in chapter 3, each individual section of the multi-element laser is treated individually and independently. For comparison with the present experiments, consider a laser employing two active sections with one section under AC modulation at a frequency $\Omega/2\pi$. In the following description, section two is DC pumped while section one is AC modulated as well as DC pumped (see Figure 4-9.) Carrying out a small signal analysis the FM/AM response ratio is given as [7]

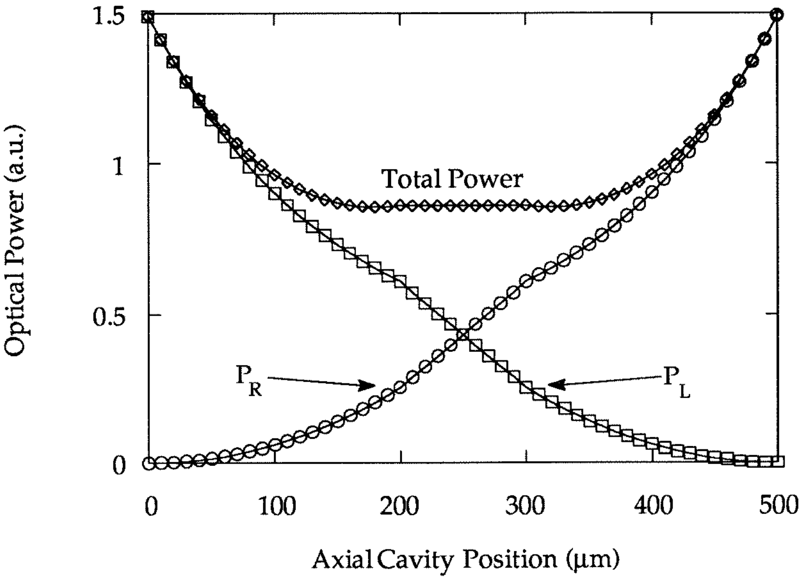

Figure 4-5: Optical power distribution for the three-section DFB laser described in Figure 4-2 and Table 4.1.

$$\frac{FM}{AM} = i\left(\alpha_{1eff} - \frac{i(\alpha_{1eff} - \alpha_{2eff}) - \omega_{2eff}^2}{\Omega/\tau_2}\right) \tag{4.8}$$

$$= i\alpha_{1eff}\left(1 - \frac{i\chi}{\Omega}\right) \tag{4.9}$$

where α_{1eff} and α_{2eff} are the effective α parameters in sections one and two, respectively, ω_{2eff} is the effective relaxation oscillation frequency in section two, and τ_2 is the effective carrier lifetime in section two defined as

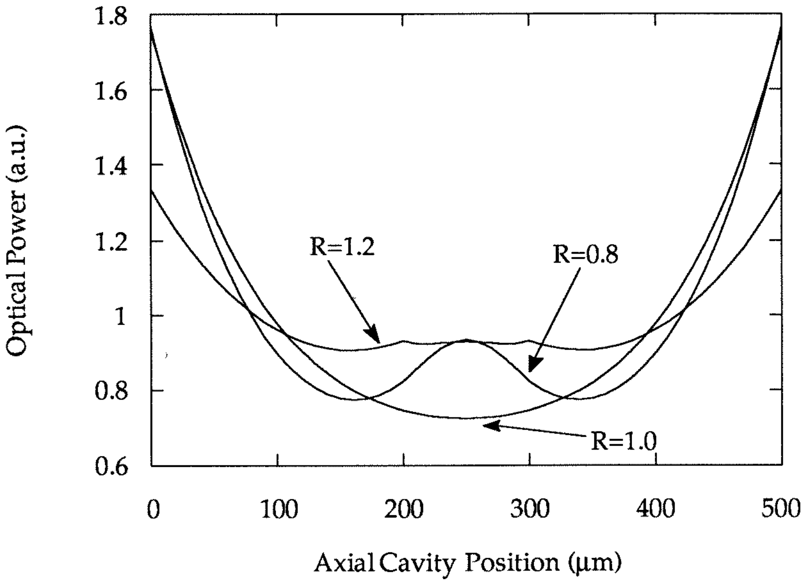

Figure 4-6: Optical power distribution for varying degrees of nonuniform injection current. The quantity R is defined as the ratio of the current *density* of the center section to that in either of the end sections.

$$\frac{1}{\tau_2} = \frac{1}{\tau_s} + \tilde{g}_2 \Gamma_2 p + g_2 p \frac{d\Gamma_2}{dn_2} \tag{4.10}$$

where τ_s is the spontaneous lifetime, g is the gain, $\tilde{g}$ is the differential gain, p is the photon density, and Γ is the fill factor defined in Ref. [6]. In obtaining Eq. 4.8 we have assumed that $1/\tau_2 >> \Omega$, an approximation valid for our experiments. The FM/AM response given in Eq. 4.8 is made up of two components. The first term represents the normal chirp associated with a semiconductor laser. The second term is an additional contribution from the different nature of the two sections of the laser.

This additional term introduces both a frequency and an output power dependence (through ω_{2eff}^2) to the FM/AM response.

The parameter χ defined in Eq. 4.9 is a quantity representing adiabatic chirp. We see that in the absence of adiabatic chirp (i.e., χ=0) the FM response is $\pi/2$ out of phase with the AM response and the ratio of the two is the effective α parameter in section one. Measurement of the FM/AM response therefore provides a direct measurement of α_{1eff}. Since the FM/AM response under these conditions is purely imaginary only a measurement of the modulus of the response is necessary. However, the incorporation of adiabatic chirp due to non-equal αparameters in the two sections complicates matters. The phase between the FM and the AM responses is obviously different from $\pi/2$ with the difference depending on χ. Therefore, measurements of both the modulus and the phase of the response function are necessary to determine the α-parameter (in addition to χ). Furthermore, the FM/AM response is now dependent on the modulation frequency and the photon density (through the effective lifetime).

In order to measure the modulus and phase of the FM/AM response a measurement similar to previous work can be carried out [11]. The experiment involves biasing the laser above threshold and superimposing a small RF current at frequency $\Omega/2\pi$. We write the electric field as

$$E(t) = E_o \left(1 + \frac{m}{2}\sin\Omega t + \phi\right)\cos\left(\omega t + \beta\sin\Omega t\right) \tag{4.11}$$

where E_o is the time-averaged value of $E(t)$, m is the intensity modulation index, β is the phase modulation index, and $(\pi/2 - \phi)$ is the phase angle between the frequency and amplitude response. (Note that in general ϕ=0 is not necessarily a solution as was the case without adiabatic chirp.) From Equation 4.11 we can write the FM/AM response as equal to $(2i\beta/m)e^{-i\phi}$. Together with Equation 4.8 this now yields

$$\frac{\beta}{m}\exp -i\phi = \frac{\alpha_{1eff}}{2}\left(1 - \frac{i\chi}{\Omega}\right) \tag{4.12}$$

We have assumed the frequency response originates solely from carrier density effects without contributions from current induced temperature changes which can produce FM at low modulation frequencies (see section 2.3.2). This assumption remains valid at the modulation frequencies used in these investigations.

For determining the FM/AM response one can directly measure the intensity modulation index m and observe the FM spectrum directly on a Fabry-Perot interferometer in order to determine β and ϕ provided m is already known. In the absence of adiabatic chirp the FM spectrum under modulation is symmetric. However, with adiabatic chirp (or other phenomena which can alter the $\pi/2$ relationship between FM and AM) the field spectrum can be shown to have asymmetric peaks. Writing the electric field as in Equation 4.11, it can be shown that the central mode intensity is given as [7,11]

$$|E(\omega)|^2 = \frac{E_o^2}{4}\left[J_0^2(\beta) + \frac{m^2}{4}J_1^2(\beta)\cos\phi^2\right] \tag{4.13}$$

and the intensity of the side modes is given as

$$\begin{aligned} |E(\omega \pm \Omega)|^2 &= \frac{E_o^2}{4}\left[J_1^2(\beta) + \frac{m^2}{16}\left[J_0^2(\beta) + J_2^2(\beta)\right]\right. && (4.14) \\ &- \frac{m^2}{8} J_0(\beta) J_2(\beta) \cos 2\phi \\ &\left.\pm \frac{m}{2} J_1(\beta)\left[J_0(\beta) + J_2(\beta)\sin\phi\right]\right] && (4.15) \end{aligned}$$

One sees that when the AM and FM responses are $\pi/2$ out of phase with each other, the sides bands are equal in size. However, if the phase difference is a value other than $\pi/2$, there exists an asymmetry in the FM spectrum and the magnitude of this asymmetry provides information on the underlying mechanism.

The coefficient χ in Equation 4.12 is shown to be proportional to the difference in the effective α parameters in the two active sections. The reason a nonzero χ leads to adiabatic chirp is due to the fact that gain changes in one section must be compensated for in the other section (i.e., $\Delta g_1 = -\Delta g_2$) to maintain oscillation. The refractive index is given by

$$\begin{aligned} \Delta n &= \Delta n_1 + \Delta n_2 \\ &= \Delta g(\alpha_{1eff} - \alpha_{2eff}) && (4.16) \end{aligned}$$

thus demonstrating the importance of χ is adiabatic chirping. The prospect for the α parameter to vary as a function of pumping level has been discussed by several authors and has been shown to be especially significant in DFB lasers [12,13,14]. It should be mentioned that other mechanisms can lead to adiabatic chirp besides those mentioned above. In particular, the presence of gain compression produces similar effects in the FM/AM response [15]. However, two of the proposed dominant mechanisms of gain compression, spectral and spatial hole burning, should not contribute significantly in these experiments since the power levels investigated were sufficiently small.

4.4 Modulation and Chirp Measurements

The laser used in these experiments is a double channel planar buried heterostructure (DCPBH) grown by a two-step liquid phase epitaxy process. A first-order uniform grating is formed on a *n*-InP substrate via holography and wet chemical etching. After InP regrowth a Au/Cr segmented electrode was formed by patterning with the end and center electrodes approximately 700 and 50 m in length, respectively.

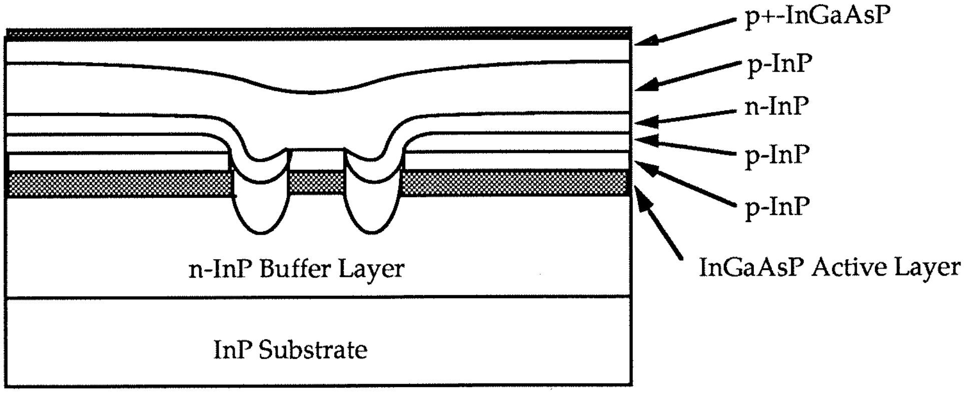

Figure 4-7: Cross-sectional view of DCPBH laser structure

The facets were cleaved and uncoated and the devices were mounted substrate down. From measurements of the below threshold spontaneous emission spectrum, the coupling coefficient was estimated to be 88 cm^{-1} and the Bragg wavelength was detuned approximately 20 nm on the blue side of the gain peak (see Figure 4-8). The device lases in a single longitudinal mode at $\lambda = 1.32$ μm with a threshold current for each individual end section (i.e., other sections unpumped) of 32 mA. Side mode suppression of 30 dB or greater was maintained throughout.

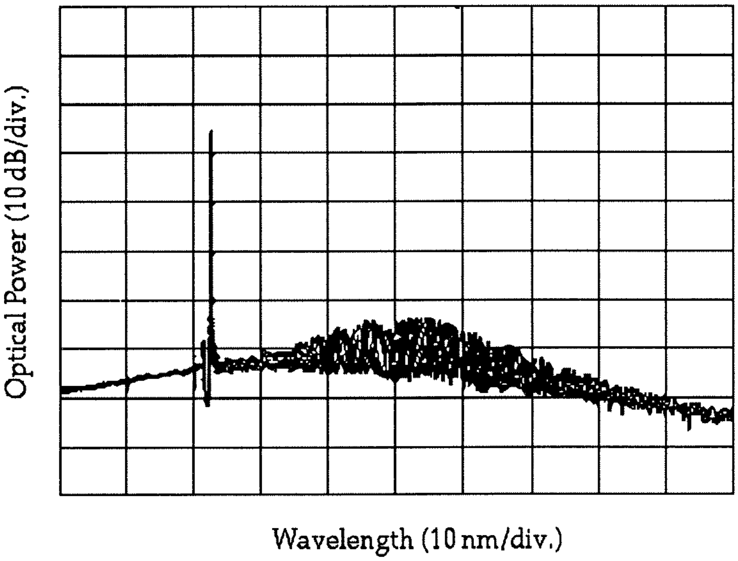

Figure 4-8: Below threshold spontaneous emission spectrum of detuned DFB laser. Lasing occurs on the blue side of the gain peak which produces a smaller effective value for α.

As shown in Figure 4-9, the two end sections are pumped with DC current while section one is also AC modulated. In all measurements section one is pumped above

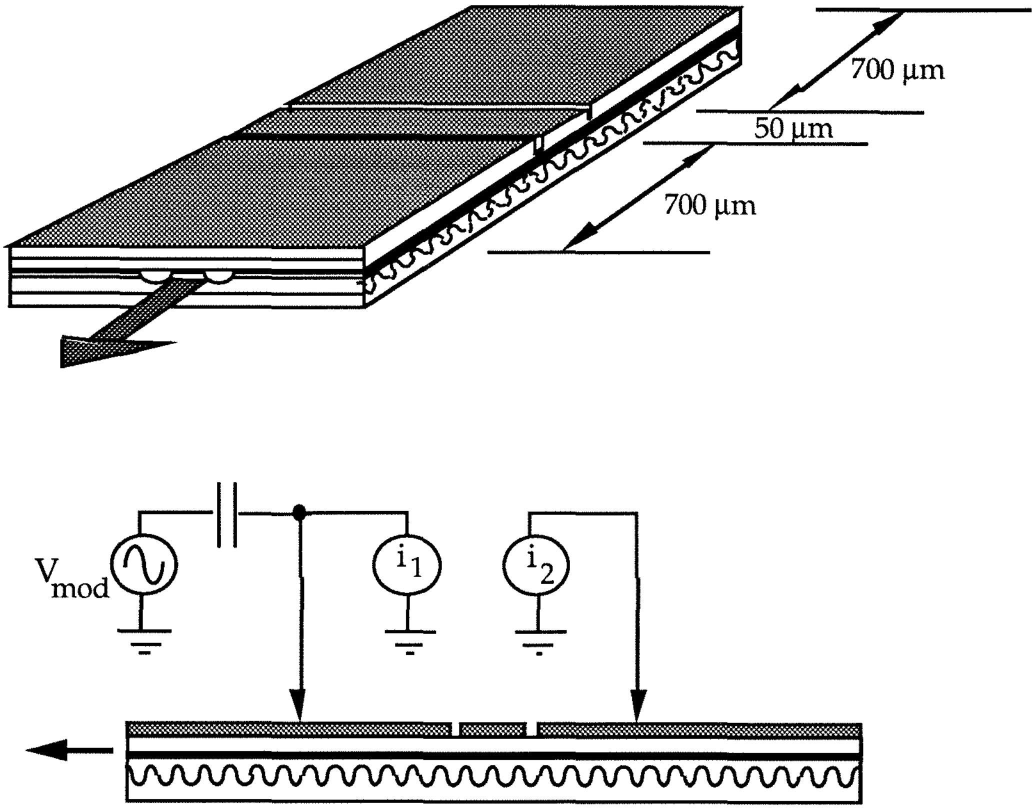

Figure 4-9: Diagram of three section dfb laser and pumping scheme

its individual threshold while section two remains below its individual threshold. The center section is left floating and acts as an absorber. Modulation measurements were performed using a HP8673D synthesized function generator to capacitively couple a RF current into the laser. An Ortel No.2610A broadband detector was used to measure the intensity modulation index m and was calibrated to + 1/2 dB. The FM spectrum was observed using a Coherent No. 240 Fabry-Perot interferometer with a

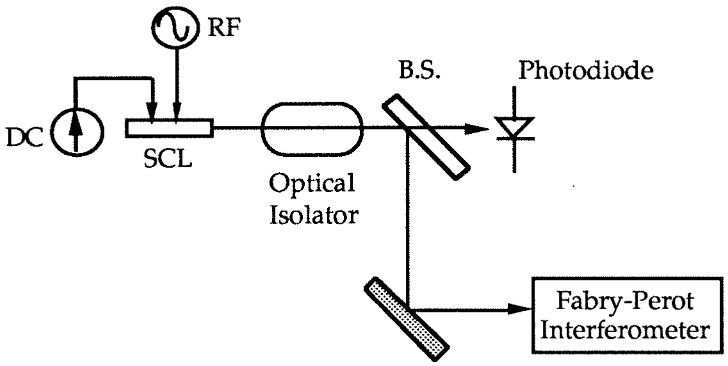

Figure 4-10: Experimental arrangement for measuring FM/AM response in DFB lasers.

free spectral range of 7.5 GHz (see Figure 4-10). In all measurements the laser was optically isolated by a minimum of 60 dB.

As discussed above, one effect of inhomogeneous excitation of a semiconductor is the introduction of a frequency and power dependence in the FM/AM response. Such behavior is shown in Figures 4-11 and 4-12. In Figure 4-11, the laser FM/AM response ratio is measured as a function of the modulation frequency. In these measurements, the laser is biased as in Figure 4-9 with section one above threshold and section two below threshold. At low frequencies, β/m increases as $1/\Omega$ as predicted in Eq. 4.9. At higher frequencies the response ratio approaches the constant value given by the effective α parameter. In Figure 4-12, β/m is plotted as a function of the output power. The modulation frequency in this measurement is 500 MHz. From Figure 4-11, the FM/AM response ratio will still show contributions of the inhomogeneous excitation. Indeed, β/m increases linearly due to its implicit dependence on power through the relaxation resonance frequency.

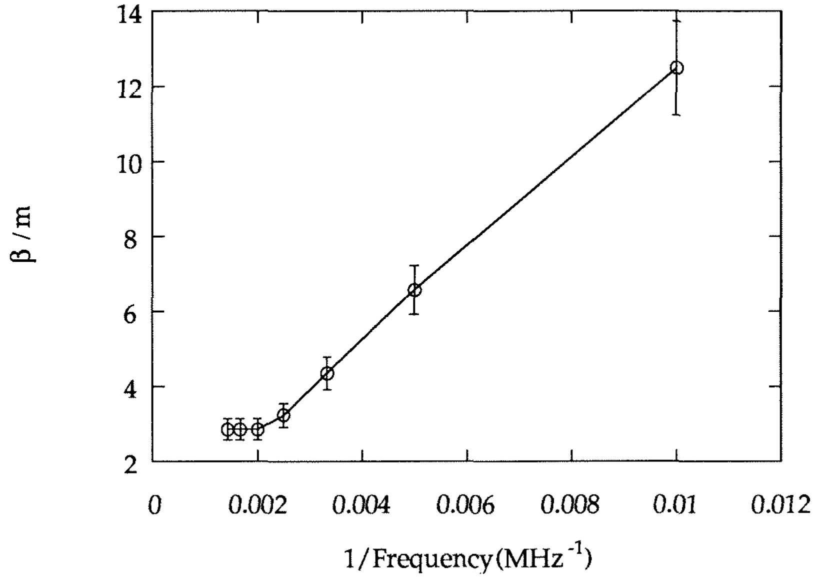

Figure 4-11: FM/AM response as a function of modulation frequency.

The adiabatic chirp will be evident in the FM spectrum as an asymmetry between the FM sidebands. In Figures 4-13 through 4-16, the FM spectra taken with the Fabry-Perot are shown at four different pumping schemes, each with the same output power of 0.4 mW. The modulation frequency used was 400 MHz. As the current in section two is increased a clear asymmetry develops indicating an increase in the adiabatic chirp χ as the photon density distribution within the cavity is varied. From these spectra one can numerically solve Equations 4.14 and 4.15 for β and ϕ. The procedure for obtaining α_{1eff} and χ is then relatively straightforward. Once ϕ is

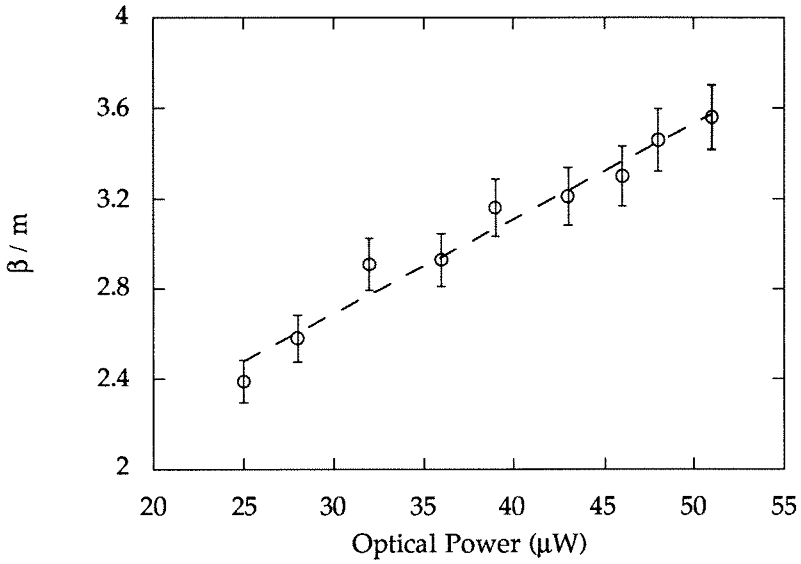

Figure 4-12: FM/AM response as a function of optical power.

known one can calculate χ from the relation

$$\tan\phi = \frac{\chi}{\Omega} \tag{4.17}$$

In Figure 4-17 the quantities α_{1eff} and χ are plotted as a function of the injection current distribution. A dimensionless parameter A is defined as

$$A = \frac{i_2}{i_1 + i_2} \tag{4.18}$$

where A=0.5 would indicate uniform pumping (neglecting the center absorber). The uniform pumping condition was not measureable in these lasers due to the strong

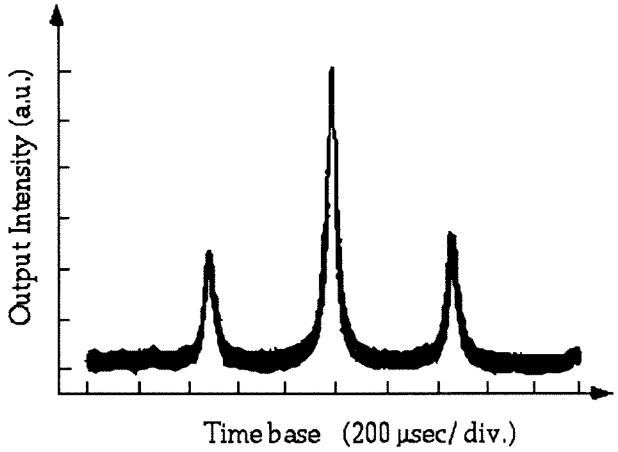

Figure 4-13: Fabry-Perot scan of DFB laser with A=0.07. Modulation frequency = 400 MHz.

detuning of the Bragg wavelength from the gain maximum (see Figure 4-8). At uniform pumping the entire laser was sufficiently transparent such that oscillation was initiated by feedback from the cleaved (uncoated) facets and not from the grating. This caused the laser to laser in the Fabry-Perot modes of the cavity.

From Figure 4-17, the effective α parameter in section one is decreased by nearly a factor of two from approximately 4 to 2. From this result one can conclude that the effective α-parameter in section two must be greater than or equal than 4 since the chirp increases with a decrease in α_{1eff}. These results are also shown in Figure 4-17. Enhancements in χ by as much as a factor of 3 were observed as the current distribution was varied. The exact mechanism for the increase in χ with pumping in section two is somewhat elusive since both parameters τ_{2eff} and ω_{2eff} can be

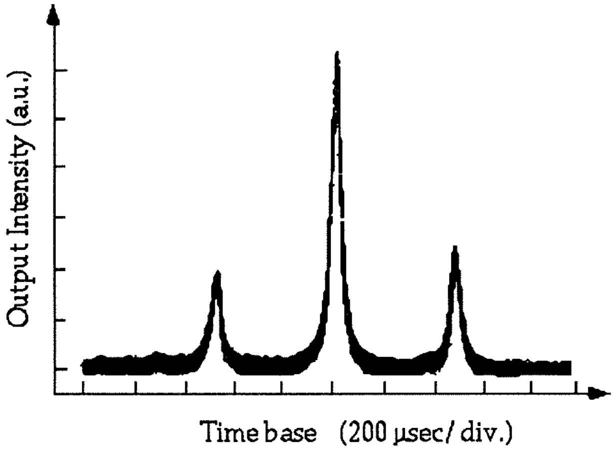

Figure 4-14: Parameters as in Figure 4-13 with A=0.24.

functions of the specific operating point. However, recent measurements have shown τ_{2eff} to decrease with the pumping level [18], which would produce a decrease in χ. A possible explanation could be that α_{2eff} is actually negative causing a decrease in α_{1eff} to lead to an increase in χ. Such behavior has been predicted in two-section lasers [19].

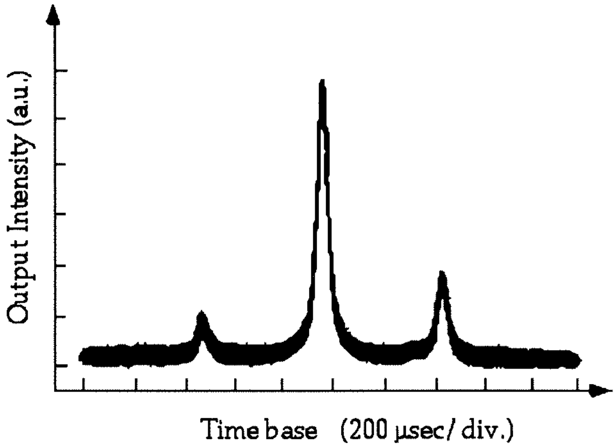

Figure 4-15: Parameters as in Figure 4-13 with A=0.32.

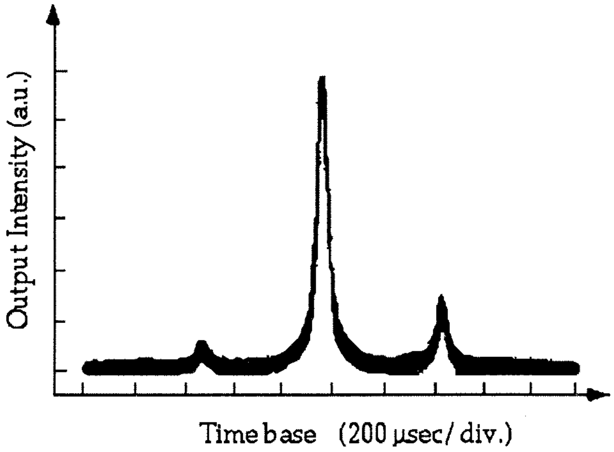

Figure 4-16: Parameters as in Figure 4-13 with A=0.36.

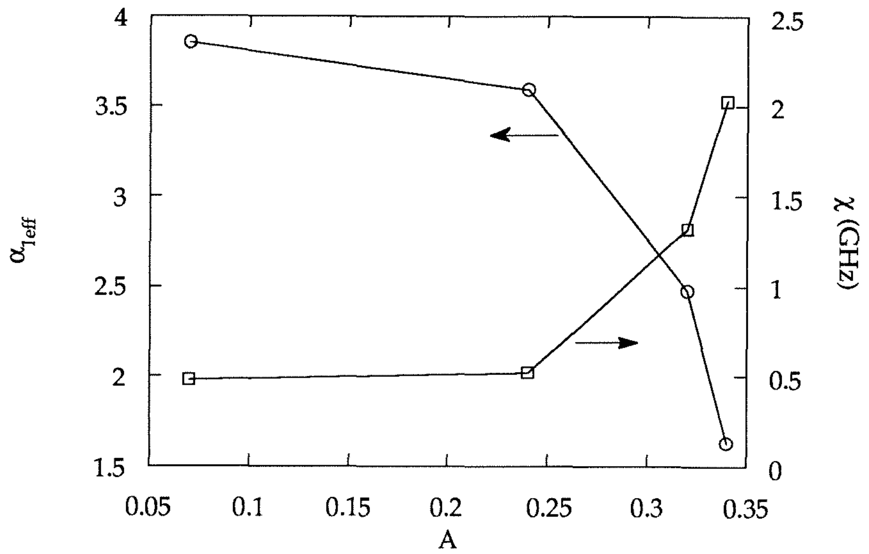

Figure 4-17: Linewidth enhancement factor and chirp as a function of injection current distribution. Modulation frequency = 400MHz.

References

[1] H.Kogelnik and C.V.Shank, *J. Appl. Phys.*, vol.43, p.2327, 1972.

[2] M.Okai, T.Tsuchiya, K.Uomi, N.Chinone, and T.Harada, *IEEE J. Quantum Electron.*, QE-27, p.1767, 1991.

[3] H.Soda, Y.Kotaki, H.Sudo, H.Ishikawa, S.Yamakoshi, and H.Imai, *Electron. Lett.*, vol.25, p.990, 1989.

[4] H.Yasaka, M.Fukuda, and T.Ikegami, *Electron. Lett.*, vol.24, p.760, 1988.

[5] Y.Kotaki, S.Ogita, M.Matsuda, Y.Kuwahara, and H.Ishikawa *Electron. Lett.*, vol.25, p.990, 1989.

[6] R.Lang and A.Yariv, *IEEE J. Quantum Electron.*, QE-21, p.1683, 1985.

[7] J.M.Iannelli, T.Schrans, T.R.Chen, Y.H.Zhuang, and A.Yariv, *Appl. Phys. Lett.*, vol.63, p.1468, 1993.

[8] C.Harder, K.Vahala, and A.Yariv *Appl. Phys. Lett.*, vol.42, p.328, 1983.

[9] O.Doyle, *Electron. Lett.*, vol.23, p.133, 1987.

[10] S.Kobayashi, Y.Yamamoto, M.Ito, and T.Kimura, *IEEE J. Quantum Electron.*, QE-18, p.582, 1982.

[11] W.Length, *IEEE J. Quantum Electron.*, QE-20, p.1045, 1984.

[12] L.Olofsson and T.G.Brown, *Appl. Phys. Lett.*, vol.57, p.2773, 1990.

[13] G.H.Duan, P.Gallion, and G.Debarge, *IEEE J. Quantum Electron.*, vo.QE-26, p.32, 1990.

[14] B.Tromborg, H.Olesen, and X.Ping, *IEEE J. Quantum Electron.*, QE-27, p.178, 1991.

[15] T.L.Koch and R.A.Linke, *Appl. Phys. Lett.*, vol.48, p.613, 1986.

[16] K.Petermann, *Laser Diode Modulation and Noise*, (Kluwer Academic, Dordrecht, The Netherlands, 1991), p.121.

[17] I.Mito, M.Kitamura, K.Kobayashi, S.Murata, M.Seki, Y.Odagiri, H.Nishimoto, M.Yamaguchi, and K.Kobayashi, *J. Lightwave Technol.*, vol. LT-1, p.195, 1983.

[18] C.Y.Kuo, Y.Twu, N.K.Dutta, E.J.Wagner, and S.W.Granlund, *Appl. Phys. Lett.*, vol.55, p.1279, 1989.

[19] R.Lang and A.Yariv, *IEEE J. Quantum Electron.*, QE-22, p.436, 1986.

[20] Thomas Schrans, *Longitudinal Static and Dynamic Effects in Semiconductor Lasers; Spectral Characteristics of Passively Mode-Locked Quantum Well Lasers*, Ph.D. Thesis, California Institute of Technology, June, 1994.

Chapter 5

Noise Induced Transitions in Optically Bistable Lasers

5.1 Introduction

The area of noise induced transitions in dynamical systems has received considerable attention in recent years. In particular, the proposal by Benzi et.al. [1] of stochastic resonance has stimulated a great deal of research. Initially put forth as an explanation of the existence of the earth's ice ages, stochastic resonance describes the phenomenon of an exchange of power between a coherent input signal and an incoherent input noise signal in a nonlinear system. The signature of this effect is an increasing signal to noise ratio (SNR) (measured at the frequency of the coherent input signal within a given bandwidth) at the system output with an increase in the input noise power (see Figure 5-1). The first experimental observation of this effect was performed by Fauve et.al. [2] by observing the switching of a saturated operational amplifier in a

Schmitt trigger circuit driven by both modulation and noise. Following this work, stochastic resonance was observed in a bidirectional ring laser [3] and later modeled and somewhat quantified [4]. Although there has been extensive theoretical work on the subject, the experimental work on stochastic resonance remains somewhat limited.

The fundamental nature of stochastic resonance lies in the inherent nonlinearity of the dynamical system in question. Although systems which display the effect can in principle by multistable, most efforts have focused on the study of bistable systems. Moreover, a distinction is often made between continuous and discrete bistable systems. As discussed in previous treatments, the output power of a discrete two-state system displaying stochastic resonance is constant, regardless of the input signal power or noise power [4]. Increasing power at the system input changes the rate of output switching between the two states; however, the additional power is merely dissipated internally by the system through relaxation mechanisms. Although the integrated output power is fixed, the frequency *characteristics* of the output power are not necessarily constant. In fact, in dynamical systems displaying stochastic resonance, power can be "redistributed" between the noise and signal components. It is precisely this redistribution of power among various frequencies that can lead to an increase in the SNR with an increase in input noise power.

A common way to visualize stochastic resonance is the double well potential model. In this model, one assumes that a particle's state is completely described by two

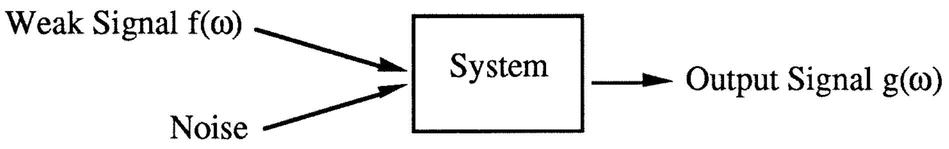

Figure 5-1: Schematic diagram of the relevant signals in a system displaying stochastic resonance.

independent states (see Figure 5-2). We assume that in making a transition from one well to another, the relaxation time within a given well is much smaller than any other time scale in question. Such an adiabatic treatment of the system will be valid for all of the investigations to be described. The particle can make transitions from one state to another either by (random) excitations over the potential barrier or by externally induced modulation of the "effective" barrier height.

If there only exists a sufficiently small modulation of the potential barrier height, transitions will not occur and therefore there is no measureable output of the system. However, as noise is added to the system the noise can actually assist in lifting the particle over the barrier thereby producing transitions and hence an output signal. One can qualitatively see that the small modulation input signal will enhance the output of the random noise induced transitions at a frequency equal to the modulation frequency. This behavior is shown in Figure 5-3.

As the input noise power is increased the transition rates between the two wells increases, particularly at the modulation frequency. However, when the input noise

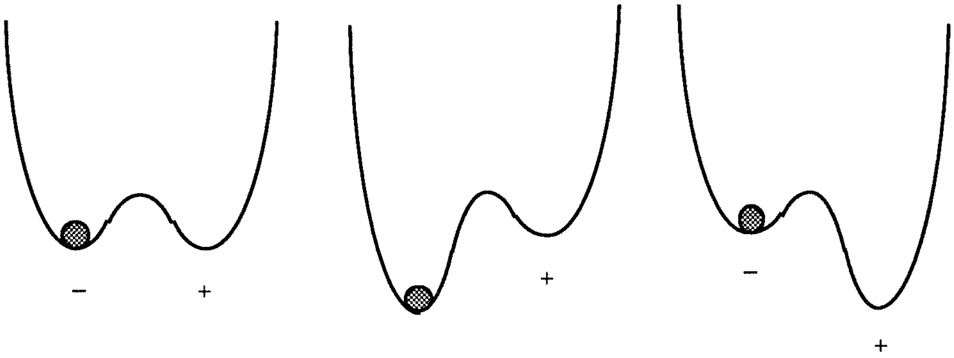

Figure 5-2: Double potential well model with the input signal modulating the barrier height. No noise is present in this picture.

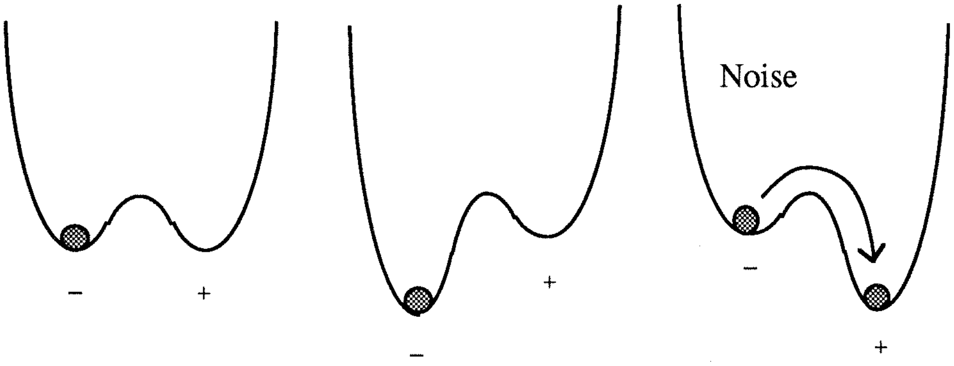

Figure 5-3: Double potential well model with signal and noise present.

becomes sufficiently large (a quantitative measure will be given shortly), the output is dominated by the random switching and looses any of the coherent nature of the input signal.

5.2 Theory of Stochastic Resonance

5.2.1 Rate Equation Analysis

In order to quantify the ideas of stochastic resonance, we follow a treatment similar to that found in [4]. We assume that the system occupies one of two stable states: z=c, z=-c. The system can be modeled by a rate equation analysis by writing the time dependent transition rates ($\Sigma_{\pm}(t)$) *out* of the potential wells as

$$\begin{aligned}\frac{d\rho_+}{dt} &= -\frac{d\rho_-}{dt} = \Sigma_-(t)\rho_-(t) - \Sigma_+(t)\rho_+(t) && (5.1)\\ &= \Sigma_-(t) - \left[\Sigma_-(t) + \Sigma_+(t)\right]\rho_+(t) && (5.2)\end{aligned}$$

The solution for $\rho_+(t)$ can be found through the use of an integrating factor as

$$\rho_+(t) = g^{-1}(t)\left[\rho_+(t_o)g(t_o) + \int_{t_o}^{t} \Sigma_-(t')g(t')dt'\right] \tag{5.3}$$

where

$$g(t) = \exp\int^{t} \left[\Sigma_+(t') + \Sigma_-(t')\right] dt' \tag{5.4}$$

The critical point in the analysis is now obtaining a form for the transition rates $\Sigma_{\pm}(t)$ such that the solution for $\rho_{\pm}(t)$ can be obtained. If one assumes that the input modulation signal is sufficiently small compared to the RMS noise power, an approximate form for the transition rates can be written as

$$\Sigma_{\pm}(t) = f(\mu \pm \eta_o \cos \omega_s t) \tag{5.5}$$

where we have taken the same notation as in Ref.[4] such that μ is a parameter representing the noise power, η_o represents the modulation amplitude, and ω_s is the modulation frequency. With this approximation the transition rate can be written as

$$\Sigma_{\pm}(t) = \frac{1}{2}\left(\alpha_o \mp \alpha_1 \eta_o \cos \omega_s t + \alpha_2 \eta_o^2 \cos \omega_s t^2 \mp ....\right) \tag{5.6}$$

where

$$\frac{1}{2}\alpha_0 = f(\mu) \tag{5.7}$$

$$\frac{1}{2}\alpha_n = \frac{(-1)^n}{n!}\frac{d^n f}{d\eta^n}(\mu) \tag{5.8}$$

After substantial algebra, the integrating factor $g(t)$ can be written as

$$g(t) = e^{\gamma t}\left[I_0(\beta) + 2I_1(\beta)\sin 2\omega_s t\right] \tag{5.9}$$

where I_n is the n^{th} order modified Bessel function, and the additional notation is defined as

$$\begin{aligned} \gamma &= \alpha_o + \frac{\alpha_2 \eta_o^2}{2} && (5.10) \\ \beta &= \frac{\alpha_2 \eta_o^2}{4\omega_s} && (5.11) \end{aligned}$$

At this point, one can obtain the conditional time dependent solution for $\rho(t|z_0, t_0)$ and from this the autocorrelation function $< z(t)z(t+\tau) >$. If one carries the above expansion only to the first order in ω_s (i.e., if only the fundamental response of the system is investigated), then one obtains the following [4]:

$$\begin{aligned} \rho_+(t|z_0, t_0) &= \frac{1}{2}\left[e^{\alpha_0(t-t_0)}\left[2\delta_{z_0 a} - 1 - \frac{\alpha 1 \eta_0 \cos\omega_s t_0 - \phi}{(\alpha_0^2+\omega_s^2)^{1/2}}\right]\right. && (5.12) \\ &\quad \left. +1 + \frac{\alpha_1 \eta_0 \cos\omega_s t - \phi}{(\alpha_0^2+\omega_s^2)^{1/2}}\right] \\ < z(t)z(t+\tau) > &= a^2 e^{-\alpha_0|\tau|}\left[1 - \frac{\alpha_1^2\eta_0^2\cos^2(\omega_s t - \phi)}{(\alpha_0^2+\omega_s^2)}\right] && (5.13) \\ &\quad + \frac{a^2\alpha_1^2\eta_0^2\left\{\cos\omega_s\tau + \cos\left(\omega_s(2t+\tau)+2\phi\right)\right\}}{2(\alpha_0^2+\omega_s^2)} \end{aligned}$$

From the autocorrelation function one can easily compute the power spectrum $S(\Omega)$ through the Wiener-Khintchine theorem thereby obtaining [4]

$$S(\Omega) = \left[1 - \frac{\alpha_1^2\eta_0^2}{2(\alpha_0^2+\omega_s^2)}\right]\left[\frac{4a^2\alpha_0}{\alpha_0^2+\Omega^2}\right] + \frac{\pi a^2\alpha_1^2\eta_0^2}{(\alpha_0^2+\omega_s^2)}\delta(\Omega-\omega_s) \qquad (5.14)$$

The power spectrum consists of a Lorentzian distribution resulting from the random noise switching (this will be shown shortly) as well as a delta function at the modulation frequency. In the absence of signal, the output remains Lorentzian, however with a slightly larger amplitude. The effect of the signal is to "clock" the random switching at the signal frequency. Furthermore, Equation 5.14 shows that there is a transfer of power from the noise to the signal. It is precisely this mechanism which leads to the increased SNR.

One can continue the expansion to the second order in ω_s in order to study the behavior of the higher harmonics of the system response function. The autocorrelation function can be found in the same manner as in Ref. [4]. After a substantial amount of algebra, one finds

$$\begin{aligned}\langle z(t)z(t+\tau)\rangle &= e^{-\gamma|\tau|}\left[1-\frac{\alpha_1^2\eta_o^2}{2(\gamma^2+\omega_s^2)}+\frac{2I_1\omega_s\alpha_2\eta_o^2}{(\gamma^2+4\omega_s^2)}+\frac{\omega_s I_1\gamma\alpha_1^2\eta_o^2}{(\gamma^2+\omega_s^2)^2}\right]\\ &\quad+\frac{1}{2}a^2\left[1-\frac{4I_1\omega_s\gamma}{(\gamma^2+\omega_s^2)}\right]\cos\omega_s|\tau|\\ &\quad+\frac{1}{2}\frac{\alpha_1^2\eta_o^2I_1}{(\gamma^2+\omega_s^2)^2}\left[2\omega_s\gamma\cos 2\omega_s|\tau|+(\gamma^2-\omega_s^2)\sin 2\omega_s|\tau|\right]e^{-\gamma|\tau|}\end{aligned}\tag{5.15}$$

In addition to the slight modifications to the exponential noise distribution and the first-order response, there are clearly contributions to the correlation at the second harmonic. The last two terms in the expression for $< z(t)z(t+\tau) >$ can be rewritten as

$$R\cos(2\omega_s|\tau|-\phi)\tag{5.16}$$

where we have defined

$$R = \sqrt{4\omega_s^2\gamma^2 + (\gamma^2 + \omega_s^2)^2} \tag{5.17}$$

$$\phi = tan^{-1}\left(\frac{\gamma^2 - \omega_s^2}{2\omega_s\gamma}\right) \tag{5.18}$$

The quantity γ is of the utmost importance in these expressions. Physically, γ behaves as the inverse of the input noise. It has been described as the ratio of the (fixed) barrier height to the noise power [4]. In finding the contribution to the power spectrum from the second harmonic terms (through a Fourier transformation) of the terms represented in Equation 5.16 one obtains

$$\frac{1}{2}\left[\frac{2\gamma\cos\phi + 2(2\omega_s - \Omega)\sin\phi}{\gamma^2 + (2\omega_s - \Omega)^2} + \frac{2\gamma\cos\phi + 2(2\omega_s + \Omega)\sin\phi}{\gamma^2 + (2\omega_s + \Omega)^2}\right] \tag{5.19}$$

If the input noise is very small with respect to the barrier height, γ becomes very large and the phase angle ϕ approaches $-\pi/2$. In this situation it could be possible for the contribution of the power spectrum from the second harmonic as given in Equation 5.19 to become negative thereby producing a dip in the spectrum at $2\omega_s$. Such behavior has been seen in analog simulations of bistable systems [16] and will be discussed below in bistable electronic circuits and semiconductor lasers.

5.2.2 Kramer's Analysis

An additional approach to the problem of stochastic resonance is to analyze the double potential well model within the framework of a Kramer's escape problem [4],[15]. The double well potential without modulation can be written as

$$V_o(z,t) = -\frac{a}{2}z^2 + \frac{b}{4}z^4 \tag{5.20}$$

and the potential with modulation as

$$V(z,t) = V_o(z,t) - Az\sin\left(\omega_s t + \phi\right) \tag{5.21}$$

The Langevin equation of motion now becomes

$$\frac{dz}{dt} = az - bz^3 + A\sin\left(\omega_s t + \phi\right) + \zeta(t) \tag{5.22}$$

where $\zeta(t)$ represents Gaussian noise such that

$$\langle\zeta(t)\rangle = 0 \tag{5.23}$$

$$\langle\zeta(t_1)\zeta(t_2)\rangle = 2D\delta(t_1 - t_2) \tag{5.24}$$

In the absence of modulation, the Kramer's escape rate can be determined by [15]

$$\Sigma_{escape} = \frac{1}{2\pi}[|V_o''(0)|V_o''(z_o)]^{1/2} exp{-}\Delta V_o/D \tag{5.25}$$

The escape time is found simple by $\tau_{escape} = 1/\Sigma_{escape}$. The input noise induces random transitions between the two wells similar to the telegraph process in communication theory. If one defines E_n as the event of obtaining exactly n transitions between times t_a and t_b, one can show that this process obeys a Poisson distribution as [14]

$$P(E_n) = \frac{[\lambda|t_b - t_a|]^n}{n!} \exp\left[-\lambda|t_b - t_a|\right] \tag{5.26}$$

It is straightforward to show that the autocorrelation function is also an exponential function and through the Wiener-Khintchine theorem, the power spectrum is then found to be a Lorentzian.

With modulation present, the rate of escape is modified and can be well approximated as

$$\Sigma_{escape} = \frac{1}{2\pi}[|V_o''(0)|V_o''(z_o)]^{1/2} exp(-\Delta V_o + u \sin \omega_s t) / D \tag{5.27}$$

Now with expressions for the transition rates the power spectrum can be calculated and the SNR determined. This has been carried out in Ref. [4] with the result

$$SNR \approx \frac{1}{D^2} e^{-}(2V_o/D) \tag{5.28}$$

At very small values of the input noise D, the SNR drops since the exponential drops more rapidly the $1/D^2$. At large values of D, the exponential approached unity and the SNR drops as $1/D^2$. Intermediate to these two regimes is a point of maximum SNR which from Equation 5.28 can be found to occur when $D = V_o$.

5.3 Experiments on Bistable Electronic Circuits

In order to investigate stochastic resonance in bistable systems, it is convenient to study the bistable electronic circuit, the Schmitt trigger, since it allows one to vary several parameters of the system easily. These parameters include the hysteresis characteristic, switching points, and switching speed. It will be shown that some of these parameters are either difficult or impossible to control in the bistable semiconductor laser.

The circuit used for these experiments is shown in Figure 5-4. It consists of input isolation stages followed by summation, additional isolation, and finally the Schmitt trigger. The output is symmetrical with respect to zero and the switching time from negative saturation to positive saturation was measured to be approximately 0.2 μsec. The inputs to the system are a 180 mV sine wave at 15 kHz and broadband white noise. The noise is obtained from a pseudorandom bit generator as describe in Appendix C. The power spectrum of the white noise was measured to be flat to within ± 0.1 dB from 400 μHz to 400 kHz. In Figure 5-5 is plotted the signal and noise amplitudes at the output of the Schmitt trigger. The measured output spectrum was

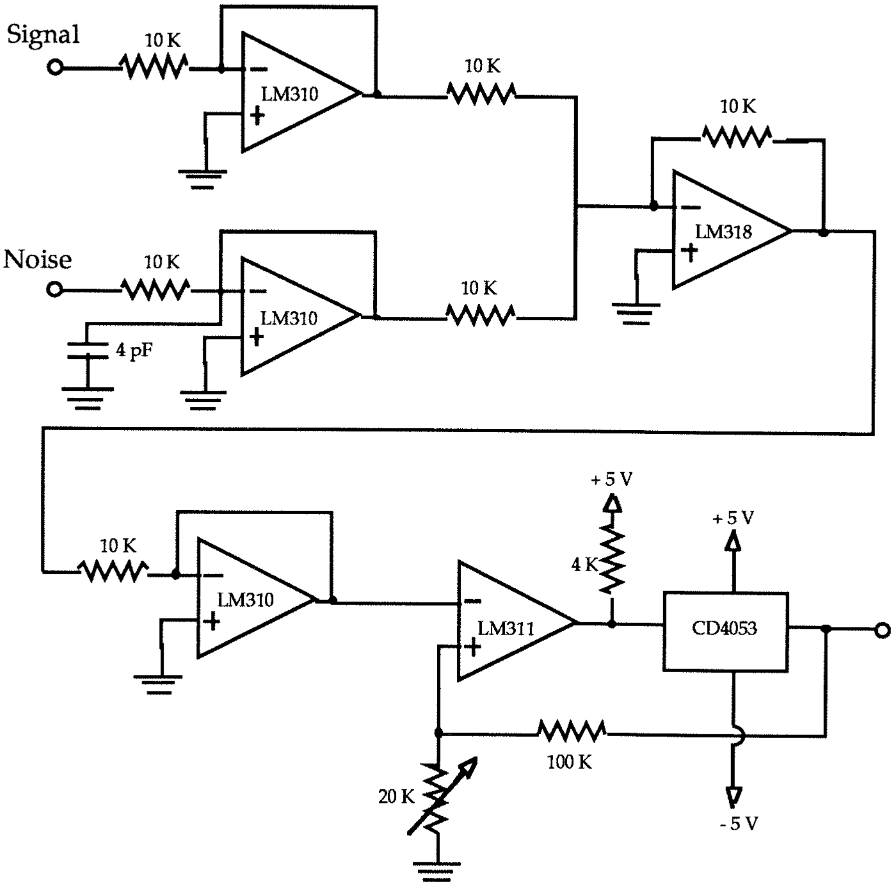

Figure 5-4: Circuit diagram of Schmitt trigger.

normalized to a 1 Hz bandwidth and averaged for 1000 scans. As the input noise power is increased both the signal and noise increase, however the signal component increases at a faster rate than the noise component. This produces an increase in the SNR as displayed in Figure 5-6. After reaching a maximum, the SNR decreases as the system is dominated by the input noise.

It is also instructive to study the phase relationship between the input and output

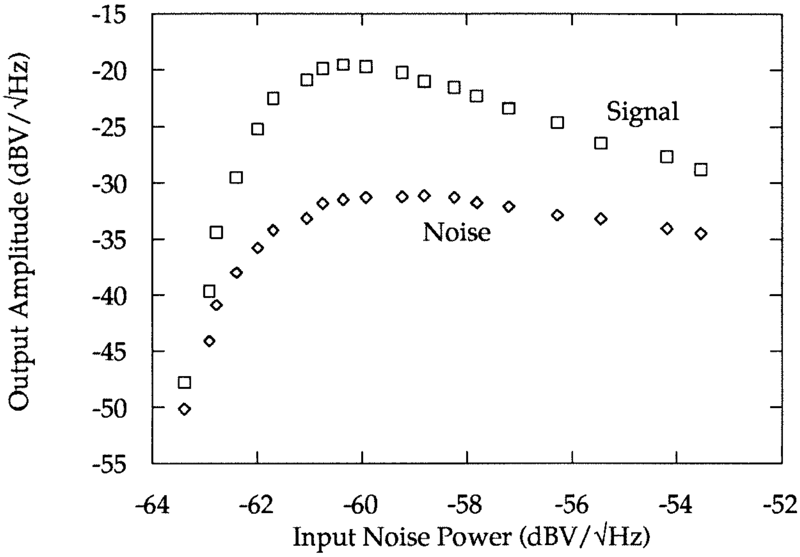

Figure 5-5: Signal output and noise output of the Schmitt trigger circuit shown in Figure 5-4. Switching occurs at $V_{in} = \pm 0.590V$. Modulation frequency is 15 kHz.

signals in the Schmitt trigger. If a sine wave is used as the input signal, the output will be a square wave whose phase is shifted from the input. It is straightforward to show that the phase shift can be written as

$$\phi = sin^{-1}(\frac{V_{hyst.}}{A}) \qquad (5.29)$$

where $V_{hyst.}$ is the switching voltage required at the input (set by the system) and A is the amplitude of the input signal.

One can take this reasoning one step further and show that input amplitude noise is converted to output phase noise in a bistable device such as this while input phase noise remains as output phase noise. This AM-PM conversion is extremely non-linear

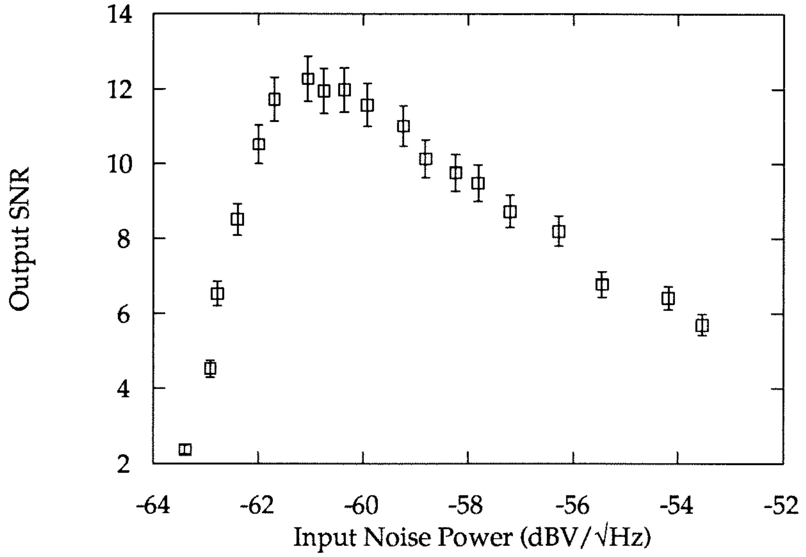

Figure 5-6: Output SNR as a function of input noise level in Schmitt trigger circuit.

as can be seen in the relation

$$\phi(t) = sin^{-1}\left[\frac{V_{hyst.}}{A_o(1 + m\cos\Omega t)}\right] \tag{5.30}$$

where m is the AM modulation index. As a test of Equation 5.29 a measurement of the input to output phase shift as a function of the input amplitude A was carried out. The results of this measurement are shown in Figure 5-7. The dashed line represents a fit of the data to Equation 5.29. From the fit a value of 180 ± 2.5 mV was obtained for the switching voltage $V_{hyst.}$ which agrees with the value calculated from the experimental parameters of 188 ± 4 mV.

In addition to the phase shift as a function of input amplitude, there also exists the obvious phase shift due to the limited response time of the system. In Figure 5-8

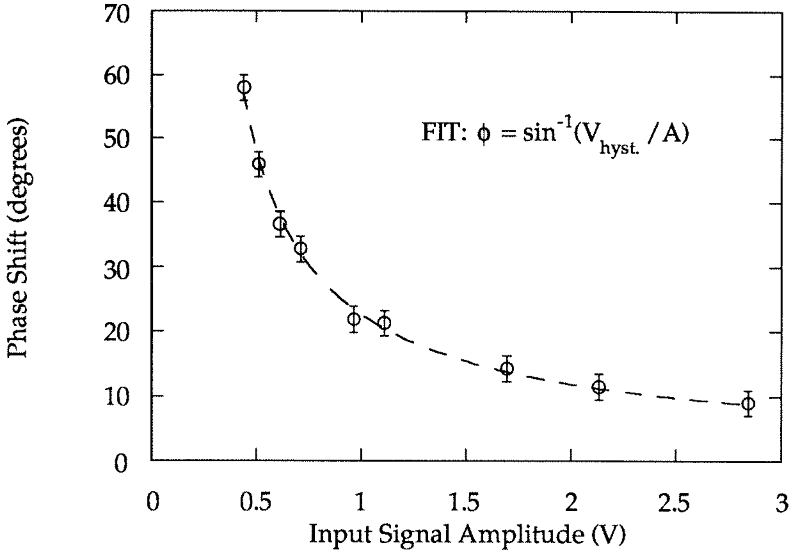

Figure 5-7: Phase relationship between input sine wave and output square wave as a function of input signal amplitude. From the fit one obtains a switching voltage of 0.18 V.

is shown the phase shift as a function of the input signal modulation frequency with the input amplitude remaining fixed. Due to the limited response time (in particular, the Schmitt trigger), this particular circuit configuration is limited to approximately a 1MHz bandwidth.

As discussed in the previous section, the response of a bistable system at the second harmonic frequency can exhibit anomolous behavior under certain input conditions. In particular, attention was given to the noise suppression or "dip" in the power spectrum at $2\omega_s$. In Figures 5-9 and 5-10 the amplitude spectrum is plotted for three different input noise levels. The modulation amplitude and frequency remain constant in all measurements as does the threshold switching voltage. The threshold voltage was set to 590 mV and the input modulation amplitude was 180 mV. One

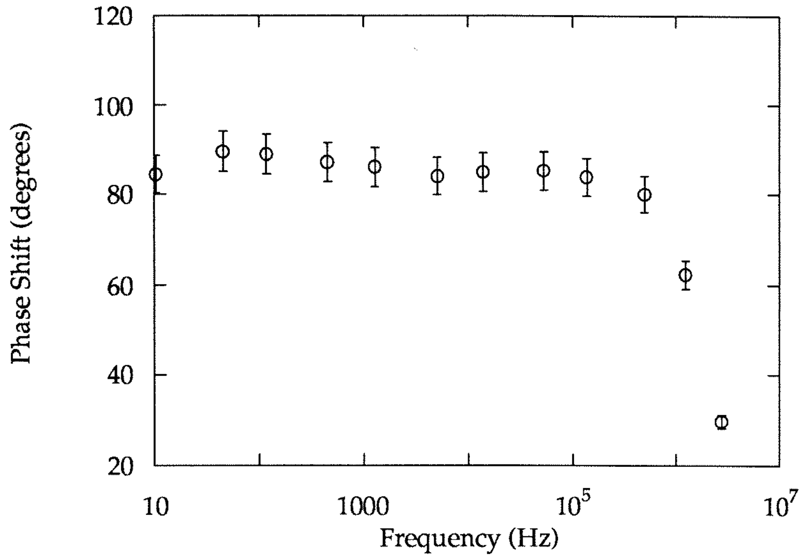

Figure 5-8: Phase relationship between the input sine wave and output square wave as a function of the modulation frequency.

sees that at low input noise levels a clear dip develops at $2\omega_s$ and the depth of the dip increases as the noise levels decreases. Also evident in both figures is a response at $3\omega_s$. Such behavior has been reported in a similar circuit however with $1/f$ noise instead of white noise at the input [5]. From the present results, it appears that there exists no requirement for noise characteristics other than white noise in order for noise "suppression" to occur at even harmonic frequencies (similar effects have been observed at the fourth and sixth harmonic).

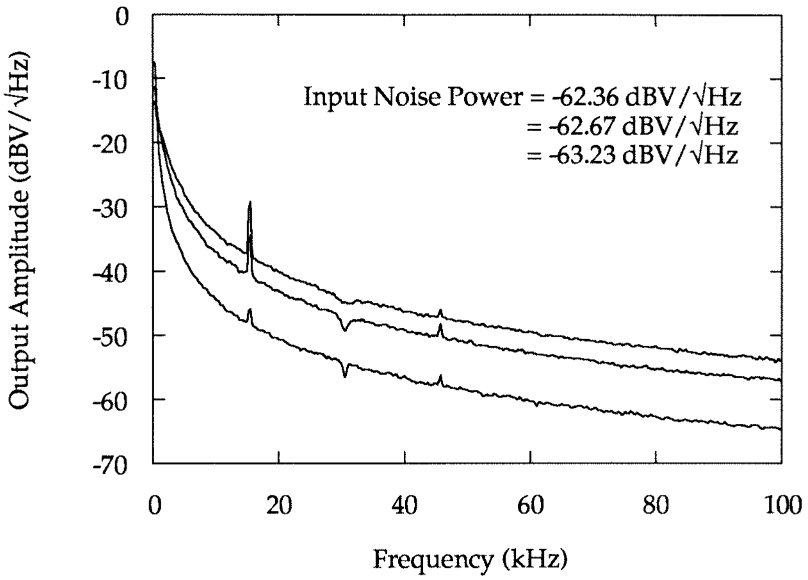

Figure 5-9: Output amplitude spectrum of the Schmitt showing response at the fundamental and second harmonic frequencies for various input noise levels.

5.4 Experiments on Bistable Semiconductor DFB Lasers

Having provided a theoretical and experimental foundation for stochastic resonance with the electronic Schmitt trigger, we now turn our attention to semiconductor lasers. In these experiments, a two-section DFB laser was used with parameters similar to those found in Chapter 4. The continuous wave (CW) threshold current in section one was 58 mA, while section two could only be pumped to 22 mA to prevent lasing off the Bragg wavelength ($\lambda_{lasing} = 1.32\mu m$). For the purposes of this investigation, the property of primary importance for this device is bistability. As shown in Figure 5-11, the laser exhibits bistability in its output power and output wavelength as a function

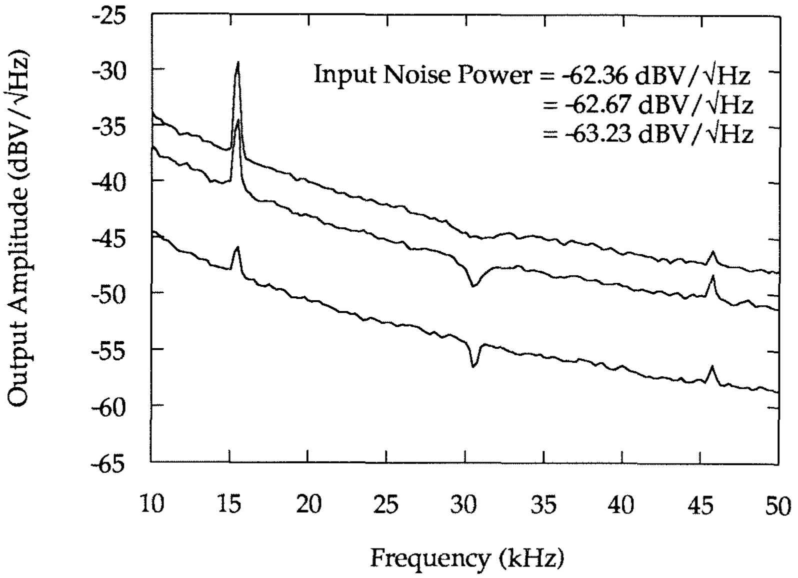

Figure 5-10: Enlarged scale of the measurements in Figure 5-9.

of injection current. (The laser exhibits this bistability with current injection into either section one or section two but for the sake of brevity we show only section one current in this figure.) It should be noted that the observed bistability is markedly different form that of the more familiar structure of a semiconductor laser with an incorporated saturable absorber. The bistability here takes place between switching of the two degenerate modes of the DFB laser. The hysteresis arises from section two acting as a (active) frequency dependent reflector. The mode spacing between λ_+ and λ_- is 14 $\mathring{A}$ and side mode suppression of 25 dB or greater was maintained throughout.

For the purposes of understanding the two states of the device we plot the various operating points of this laser in the $i_1 - i_2$ plane as shown in Figure 5-12. The figure shows the regions of consistent operation in either mode one or mode two and also

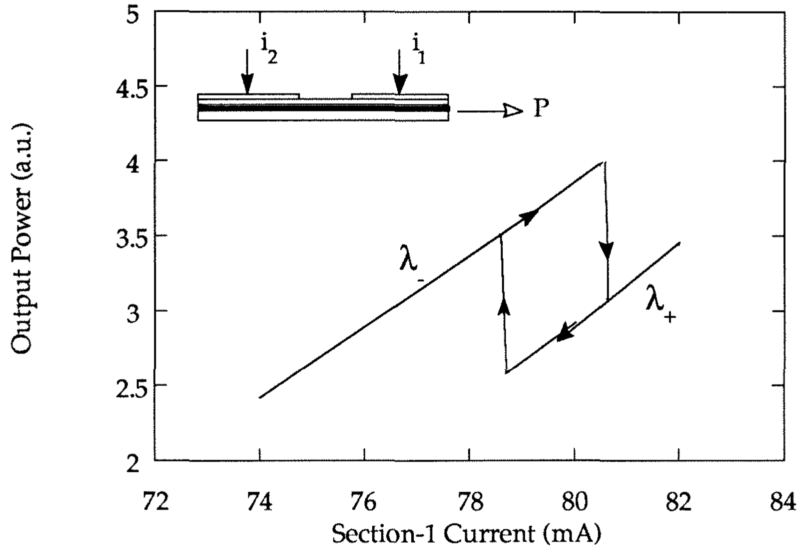

Figure 5-11: Bistable operation two section DFB laser.

the region of hysteresis. The operating mode in the hysteresis region depends on the recent history of arriving at the operating point. With the information in Figure 5-12 an optical experiment analogous to the electronic Schmitt trigger experiment can be constructed. An operating point is selected within the hysteresis region as designated by the asterisk. A small modulation current is then superimposed on i_1^{DC} and a noise current (white) is superimposed on i_2^{DC}. In the context of previous treatments of stochastic resonance, these currents have the effect of modulating the "potential barrier height" and varying the particle's energy, respectively. However, the dynamics here are somewhat different from the double potential well picture since the random variable is discrete and switching between states is taken to be instantaneous. As previously discussed, one must exercise care when considering white noise (zero correlation time) in such discrete state systems. Frequently, the noise is modeled as an exponentially correlated process (i.e., Ornstein-Uhlenbeck noise) [8].

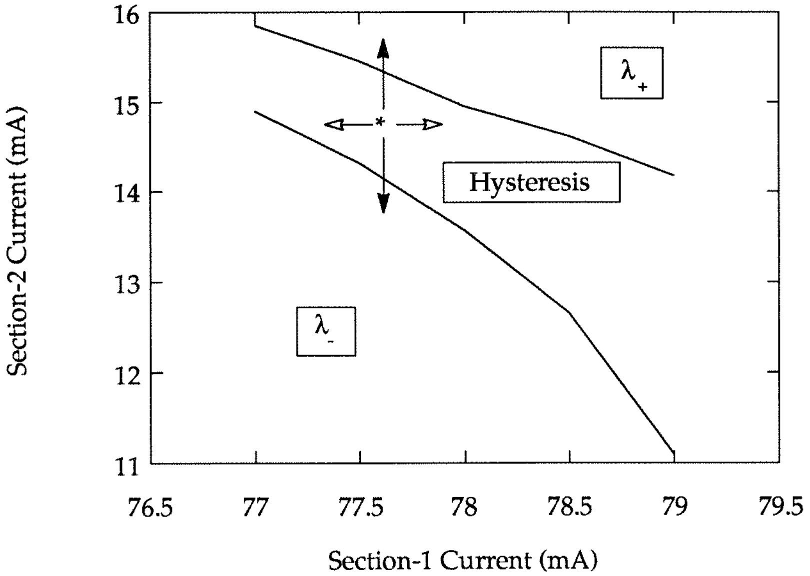

Figure 5-12: Operating point graph for two section DFB laser. The asterisk represents the operating point for the stochastic resonance experiments.

The observation of stochastic resonance in this device can be accomplished by employing the output power or the oscillation wavelength as the output variable. We choose to measure the oscillation wavelength since this greatly facilitates distinguishing the two separate states. A modulation current at 30 kHz is capacitively coupled into section one and a white noise current is directly injected into section two. The output optical field of the laser is passed through a 0.28m spectrometer (resolution of 2Å) which is tuned (arbitrarily) to transmit λ_-. The output signal is detected with a 10 MHz bandwidth germanium photodiode and provides the output signal for spectral analysis. In this way, the detector output is high when the laser was lasing in mode one (λ_-) and low when the laser was lasing in mode two (λ_+). The power spectrum of the detector current was then amplified and observed on a Stanford Research Systems SR760 FFT audio spectrum analyzer with a resolution bandwidth of 250 Hz over a 100 kHz span.

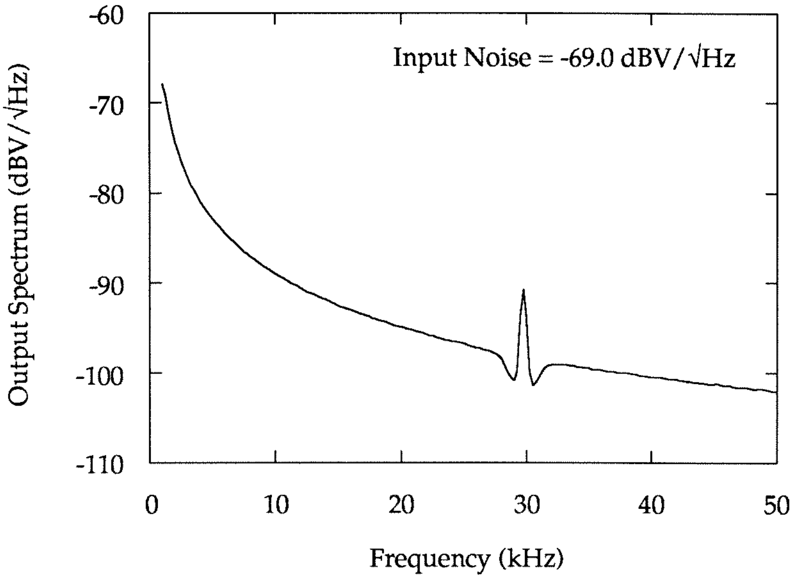

Figure 5-13: Output amplitude spectrum of electrically switched DFB laser.

The modulated signal applied to the system was sufficiently weak such that in the absence on input noise no switching occurred. The introduction of noise (which alone is able to induce random transitions) then provides an effective lowering (in phase) of the potential barrier height such that transitions driven by the modulated signal may occur. A typical power spectrum of the output current of the photodiode is shown in Figure 5-13. The power spectrum consists of the characteristic peak at the modulation frequency superimposed on the Lorentzian noise distribution. As the input noise power was increased the width of the Lorentzian increased accordingly (see Figure 5-14).

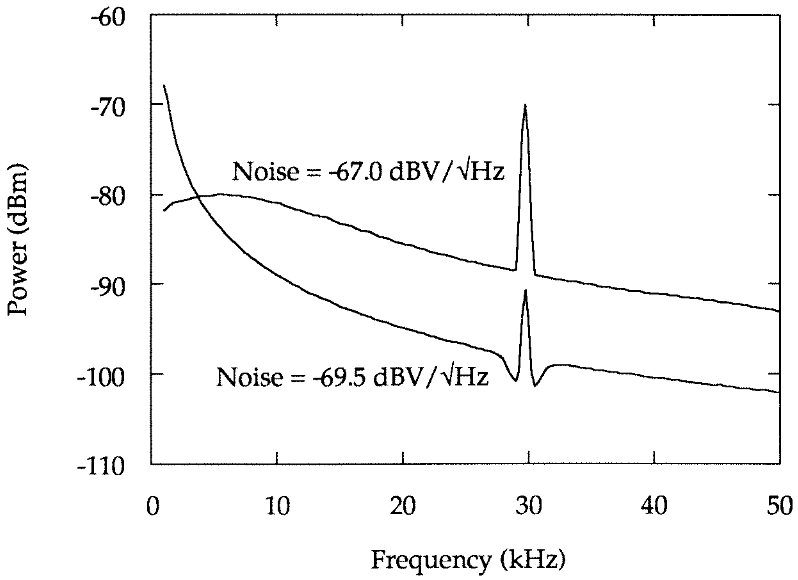

Figure 5-14: Output amplitude spectra for various noise levels in an electrically switched DFB laser.

In order to observe stochastic resonance, the SNR at the modulation frequency was measured at various input noise powers while keeping the modulation amplitude and frequency constant. The signal is defined as the height of the modulation induced peak in the output amplitude spectrum and the noise as the interpolated level at the modulation frequency (or the noise power at the modulation frequency with *only* noise at the input). The results of this measurement are shown in Figure 5-15. (The SNR has been normalized to a 1 Hz bandwidth for convenience.) As the input noise power is increased, the output SNR increases by approximately 22 dB before decreasing at high input noise power. This behavior is similar to that reported in [2] and represents the first observation of stochastic resonance in a semiconductor laser. It should be noted that switching times in this laser are on the order of 1 ns and therefore could serve

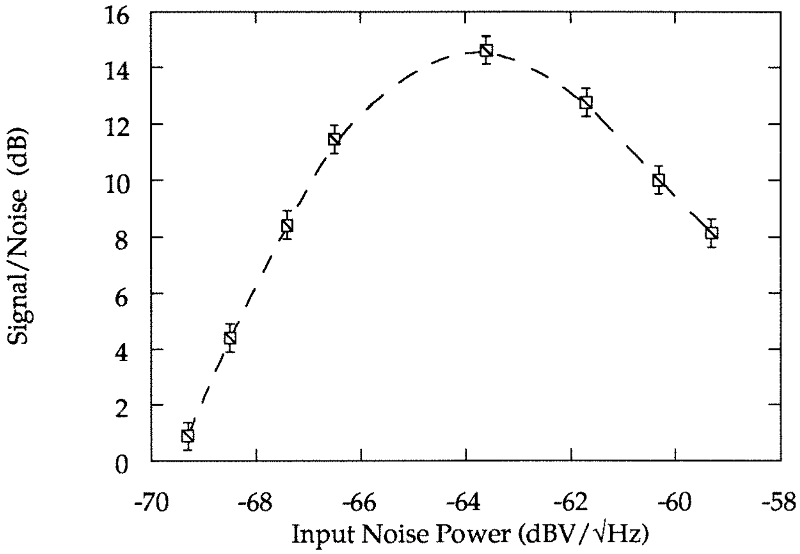

Figure 5-15: Output SNR as a function of input noise power in a two section DFB laser.

as a useful tool for experimentally studying ultra-high frequency effects in stochastic resonance.

It is instructive to study the signal and noise components in the output spectrum separately. In Figure 5-16 we see that at low input noise levels the output signal component *increases* with input noise at a faster rate than the corresponding output noise component. Similarly, at high input noise levels the output signal *decreases* at a faster rate than the output noise component. It is straightforward to conclude that intermediate to these two regimes lies a maximum in the output SNR. This behavior is quite similar to the previous experiments with the Schmitt trigger further supporting the notion of stochastic resonance as a universal phenomenon.

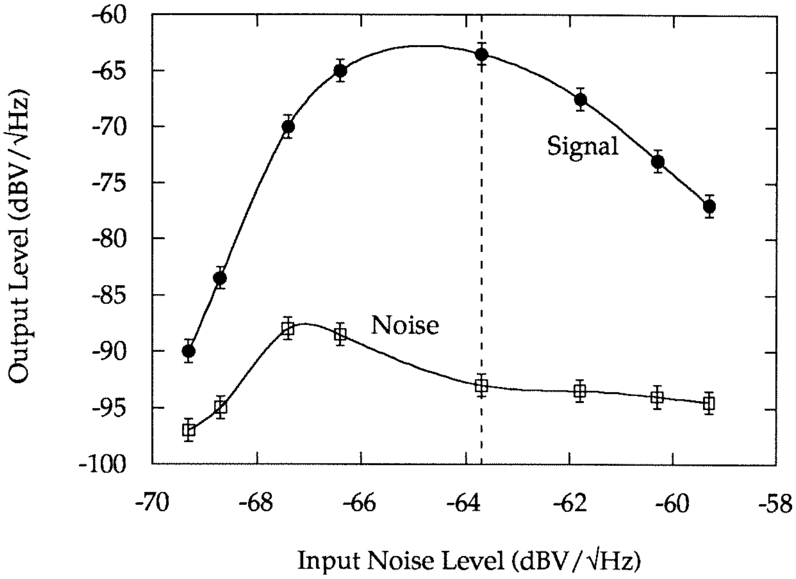

Figure 5-16: Signal and noise components in two section DFB laser.

5.5 All Optical Stochastic Resonance in a Bistable Semiconductor Fabry Perot Laser

In addition to observing stochastic resonance in an electronic input/electronic output system or an electronic input/optical output system, one can also investigate an all-optical system utilizing both optical input and output signals. Such a scheme could prove to be useful in an all-optical repeater technology [9]. The most straightforward method of observing all-optical stochastic resonance in semiconductor lasers is to employ a Fabry-Perot laser structure which incorporates a saturable absorber. This device has been investigated extensively by Harder and Yariv [11]. A schematic diagram of the device is shown in Figure 5-17.

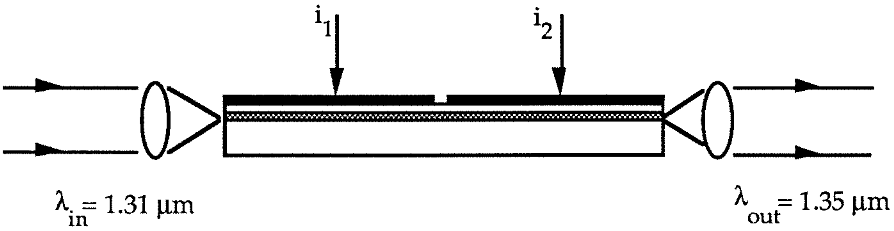

Figure 5-17: Two-section Fabry-Perot laser incorporating a saturable absorber.

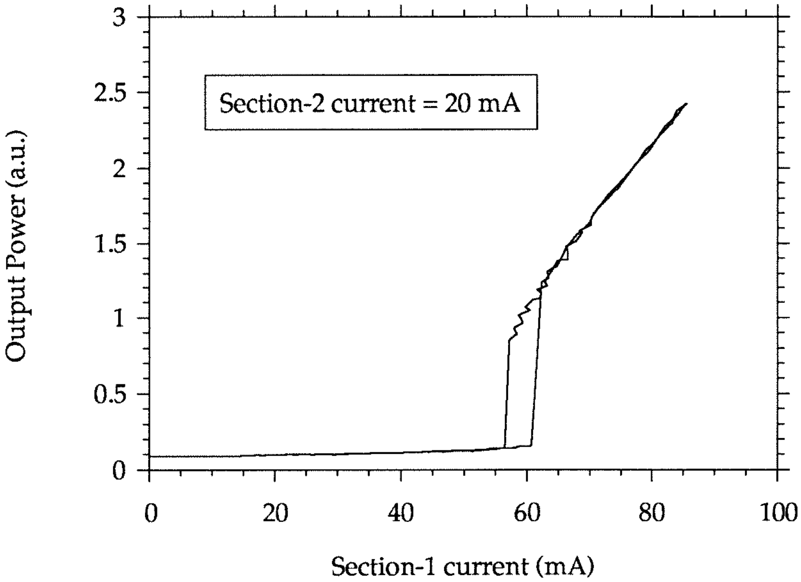

Figure 5-18: Hysteresis characteristic of a two-section Fabry-Perot semiconductor laser

Typically, bistability in this device is exhibited by sweeping the injection current in one of the sections thereby causing the output to switch from above to below threshold with a hysteresis characteristic. Measurements of such behavior is shown in Figure 5-18. The laser used was a two-section InGaAsP Fabry-Perot laser with uncoated facets. Each section length was 350 μm with an electrical isolation of appoximately 800 Ω. As the current in section two is increased, the hysteresis loop moved to lower currents since the absorber section (in this case, section two) is more readily bleached by the internal optical field. Section one turn-on currents were decreased to 50 mA (section two current = 25 mA) and 43 mA (section two current = 30 mA). The fact that the hysteresis loop can be varied in its position is a very useful characteristic for the stochastic resonance experiments.

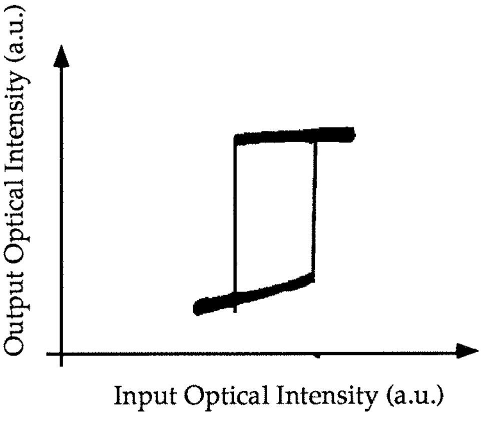

Figure 5-19: Hysteresis characteristic in an optical input/output bistable Fabry-Perot laser diode.

In these experiments, we use an optical signal which is coupled into the active layer as the input modulation signal. Such an arrangement is similar to an injection locking geometry. The hysteresis characteristic for this configuration is shown in

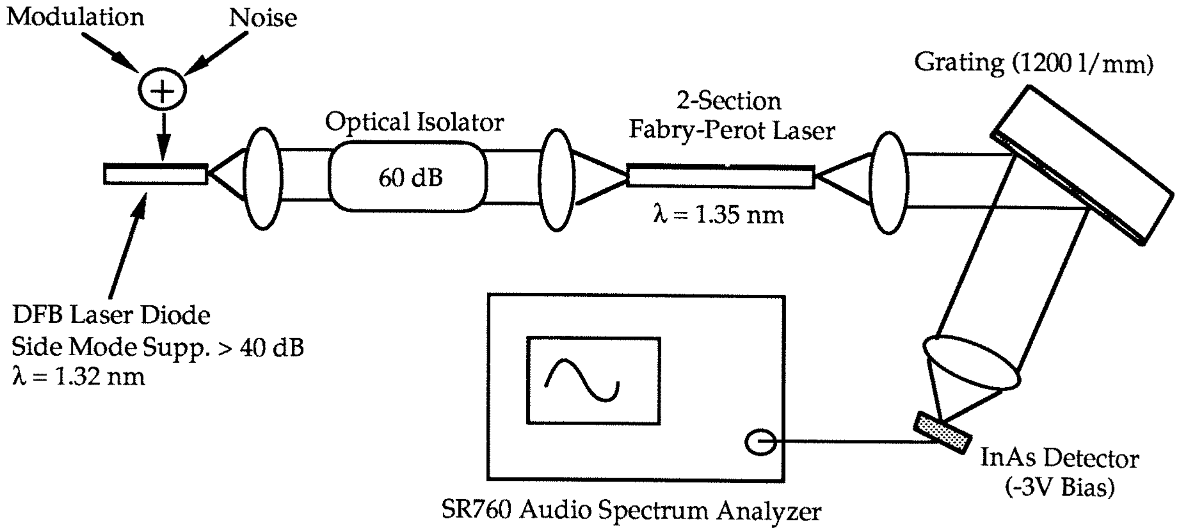

Figure 5-20: Experimental set-up for measuring all optical stochastic resonance in a two-section Fabry-Perot laser.

Figure 5-19. An experiment analogous to the Schmitt trigger can now be constructed. The experimental arrangement for this experiment is shown in Figure 5-20. An optical signal with a given SNR is "constructed" by using suitable AC and noise currents to drive a single-mode DFB laser lasing at 1.32 μm. After optical isolation, this optical signal is injected into the back facet of the two section Fabry-Perot laser described above. The two DC currents of the Fabry-Perot laser enable the hysteresis loop to be positioned such that the average DC optical power lies in the center of the loop. This is analogous to the selection of the operating point in Figure 5-12. The output of the Fabry-Perot ($\lambda = 1.35\mu m$) is separated from any trace of the input signal which may diffract around the laser with a diffraction grating. The signal is then detected with a photodiode whose photocurrent is measured as before.

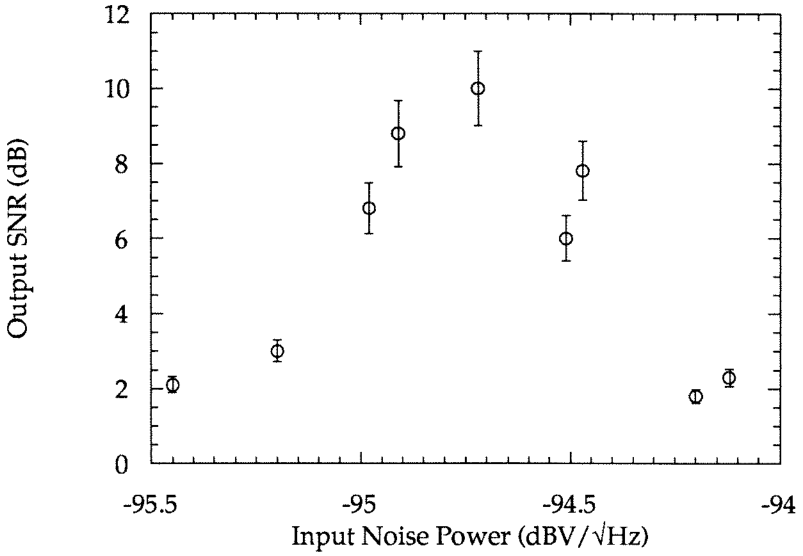

Figure 5-21: Output SNR as a function of input noise power for bistable two section Fabry-Perot laser.

The results of this measurement are shown in Figure 5-21. As with the other stochastic resonance experiments, there is a dramatic increase in the output SNR with an increase in the input noise power and then a subsequent decay at large noise values. As alluded to previously, this device could hold promise for applications in optical regeneration and wavelength conversion. Its ability to tune not only the hysteresis position but also the hysteresis width through the DC current selection enables this device to tailor its response to a variety of input signal characteristics.

5.6 Conclusions

The phenomenon of stochastic resonance has been shown to be a somewhat universal effect in connection with bistable dynamical systems. It was demonstrated in electronic systems, opto-electronic systems, and lastly all optical systems. From the point of view of applications, the bistable Fabry-Perot laser offers much promise since all signals remain in the optical domain. However, there are many areas which still need to be investigated. Some of these include the influence of "critical slowing down" on the system response, the effects of input noise other than white noise, and the possibility of exploiting the anomolous behavior of these systems at the second harmonic frequency. Given the importance of SNR and its possible enhancement in modern communications systems, stochastic resonance should remain a viable area of research.

References

[1] R.Benzi, A.Sutera, and A.Vulpani, *J .Phys. A*, vol.14, L453, 1981.

[2] S.Fauve and F.Heslot, *Phys. Lett.*, vol.97A, p.5, 1983.

[3] B.McNamara, K.Wiesenfeld, and R.Roy, *Phys. Rev. Lett.*, vol.60, p.2626, 1988.

[4] B.McNamara and K.Wiesenfeld, *Phys. Rev. A*, vol.39, p.4854, 1989.

[5] L.B.Kiss, Z.Gingl, Z.Marton, J.Kertesz, F.Moss, G.Schmera, and A.Bulsara, *J. of Stat. Phys.*, vol.70, p.451, 1993.

[6] M.Nakamura, H.W.Yen, A.Yariv, E.Garmire, and S.Somekh, *Appl. Phys. Lett.*, vol.23, p.224, 1973.

[7] J.Iannelli, T.Schrans, T.R.Chen, Y.H.Zhuang, and A.Yariv, *Appl. Phys. Lett.*, vol.63, p.1468, 1993.

[8] P.Hanggi, P.Jung, C.Zerbe, and F.Moss, *J. of Stat. Phys.*, vol.70, p.25, 1993.

[9] H.Kawaguchi, *Bistabilities and Nonlinearities in Laser Diodes*, Artech House, Boston, 1994.

[10] I.Mito, M.Yamaguchi, and K.Kobayashi, *IEEE J. Lightwave Technol.*, vol.LT-1, p.195, 1983.

[11] C.Harder, K.Lau, and A.Yariv, *IEEE J. Quantum Electron.*, vol.QE-18, p.1351, 1982.

[12] M.Jinno and T.Natsumoto, *IEEE J. Lightwave Technol.*, vol.LT-10, p.448, 1992.

[13] K.-Y.Liou, C.A.Burrus, U.Koren, and T.L.Koch, *Appl. Phys. Lett.*, vol.51, p.1777, 1987.

[14] J.S.Bendat, *Principles and Applications of Random Noise Theory*, John Wiley and Sons, New York, p.191, 1958.

[15] H.A.Kramers, *Physica*, vol.7, p.284, 1940.

[16] F.Moss, unpublished.

Appendix A

Rate Equation Analysis of an Externally Coupled Dispersive Loss

The result for linewidth reduction by a dispersive loss as predicted from the Van der Pol analysis is applicable to any semiconductor laser system with optical feedback (under the constraints mention in section 3.2.1). As previously stated in the preceding analysis, it was assumed that the loss mechanism was situated within the semiconductor laser cavity. The difference between an analysis of a loss mechanism within the semiconductor laser or external to it appears as a correction in the amplitude fluctuation terms in the rate equations. This arises from the effects of the finite delay time of the field in passing through the external loss mechanism. For calculating the spectral linewidth this does not affect the results, as will be shown. This shows the validity of the Van der Pol method. It is independent of the particular configuration or geometry of the optical feedback. The key advantage of this analysis is that one only needs to calculate Q from the system specific operating conditions.

As a verification of this model we now calculate the linewidth reduction for our system by carrying out detailed dynamic calculations for the complex field amplitude and carrier density.

To calculate the laser linewidth the rate equations are written as

$$\begin{aligned}
\dot{S}(t) &= (G - \frac{1}{\tau_p}S(t) + 2\left[\kappa(\omega_m) + \frac{\partial\kappa}{\partial\omega}\dot{\phi}\right] \cdot \sqrt{S(t-\tau)S(t)}\cos(\Phi + \delta\phi) && \text{(A.1)} \\
\dot{\phi}(t) &= \frac{\alpha}{2}(G - \frac{1}{\tau_p}) - (\omega_m - \Omega) - \left[\kappa(\omega_m) + \frac{\partial\kappa}{\partial\omega}\dot{\phi}\right] \cdot \sqrt{\frac{S(t-\tau}{S(t)}}\sin(\Phi + \delta\phi(&& \text{(A.2)} \\
\dot{N} &= -GS - \frac{N}{\tau_s} + E + \Xi && \text{(A.3)}
\end{aligned}$$

where τ_s is the spontaneous carrier lifetime, E is the pumping rate, and Ξ is the carrier Langevin noise source. The rate equations are linearized about small variations as in Section 2.3. Additionally, the time delayed quantities are Taylor expanded as

$$\begin{aligned}
\sqrt{\frac{S(t-\tau)}{S(t)}} &\approx 1 - \frac{\tau\dot{\rho}}{2S_o} && \text{(A.4)} \\
\partial\phi &= \phi(t) - \phi(t-\tau) && \text{(A.5)} \\
&\approx \tau\dot{\phi} && \text{(A.6)}
\end{aligned}$$

Equation A.6 relies on the assumption that the delay time τ is much smaller than the coherence time, which is valid for the cavity lengths and observed linewidths in this experiment. This linearization leads to a system of coupled linear differential equations

$$\begin{aligned}\dot{\rho}(1+a_{\Phi})+2S_o\dot{\varphi}(b_{\Phi}-a_{\kappa}) &= G_N S_o \eta - \frac{R^{SP}}{S_o}\rho + \Delta_S && \text{(A.7)}\\ \dot{\phi}(1+a_{\Phi}+b_{\kappa})-\frac{b_{\Phi}}{2S_o}\dot{\rho} &= \frac{\alpha}{2}G_N\eta + \Delta_{\phi} && \text{(A.8)}\\ \dot{\eta} &= -\left(\frac{1}{\tau_s}+G_N S_o\right)\eta - G(n_o)S_o + \Xi && \text{(A.9)}\end{aligned}$$

where a_{Φ} and b_{Φ} are the in-phase and quadrature components, respectively, of the frequency dependent phase variations of the field field defined as

$$\begin{aligned}a_{\Phi} &= \kappa(\omega_m)\tau(\omega)\cos\Phi && \text{(A.10)}\\ b_{\Phi} &= \kappa(\omega_m)\tau(\omega)\sin\Phi && \text{(A.11)}\end{aligned}$$

and a_{κ} and b_{κ} are the in-phase and quadrature components of the frequency dependent amplitude variations of the feedback field defined as

$$\begin{aligned}a_{\kappa} &= \left.\frac{\partial\kappa}{\partial\omega}\right|_{\omega=\omega_m}\cos\Phi && \text{(A.12)}\\ b_{\kappa} &= \left.\frac{\partial\kappa}{\partial\omega}\right|_{\omega=\omega_m}\sin\Phi && \text{(A.13)}\end{aligned}$$

This linear system of coupled differential equations can be readily solved by taking the Fourier transform of the equations and then algebraically solving for the transformed functions $\tilde{\rho}, \tilde{\phi}$, and $\tilde{\eta}$. Instead of then carrying out the inverse transformations one can calculate the variance of the phase diffusion as

$$< \Delta\phi(t)^2 >= \frac{1}{\pi} Real \int_{-\infty}^{\infty} d\Omega < |\tilde{\phi}(\Omega)|^2 > (1 - e^{i\Omega t} \tag{A.14}$$

where the Fourier transform of the phase is given by

$$\tilde{\phi} = \frac{A_S \tilde{\Delta_S}(\omega) + A_\phi \tilde{\Delta_\phi}(\omega) + A_n \tilde{\Xi}(\omega)}{Det} \tag{A.15}$$

where the determinant *Det* is given by

$$\begin{aligned} Det &= i\omega \left\{ G(n_o) G_N S_o \left[\alpha(b_\Phi - a_\kappa) - (1 + a_\Phi + b_\kappa) \right] - \left(i\omega + \frac{1}{\tau_s} + G_N S_o \right) \right. \\ &\cdot \left. \left[\left(i\omega(1 + a_\Phi) + \frac{R^{SP}}{S_o} \right) (1 + a_\Phi + b_\kappa) - i\omega b_\Phi (b_\Phi - a_\kappa) \right] \right\} \end{aligned} \tag{A.16}$$

Since we are only interested in the linear time dependence of $\langle \Delta\phi(t)^2 \rangle$ (i.e., phase diffusion behaving as Brownian motion) in calculating the linewidth, Equation A.14 is evalulated by contour integration only considering the secord-order pole at $\omega = 0$.

After a substantial amount of algebra this integration leads to

$$\langle \Delta\phi(t)^2 \rangle = \frac{R^{SP}}{2S_o} \frac{1 + \alpha^2}{(1 + \alpha C_r + C_i)^2} t = 2\pi(\Delta\nu)t \tag{A.17}$$

where the quantities relating to the self-damping rates have been neglected and C_r and C_i are as defined in Equations 3.25 and 3.27. Using the definition of the modified Schawlow-Townes linewidth, $\Delta\nu_o = R^{SP}(1+\alpha^2)/4\pi S_o$, the expression for the linewidth reduction becomes

$$\frac{\Delta\nu}{\Delta\nu_o} = \frac{1}{[1+\alpha C_r + C_i]^2} = \frac{1}{Q^2} \tag{A.18}$$

Therefore, the linewidth reduction behaves as $1/Q^2$ identically as predicted by the Van der Pol analysis.

Appendix B

Resonant Doppler-Free Faraday Rotation in Atomic Cesium as a Dispersive Loss

In order to describe quantitatively the feedback signal from the external cavity containing the cesium vapor, we calculate the susceptibility of the cesium / magnetic field system as a function of wavelength. The susceptibility for calculating the pump transmission is simply a straightforward calculation involving an inhomogeneously broadened medium. For the returning probe beam, one must take into account the redistribution of level populations induced by the pump beam. Various authors have treated either the cesium system or similar systems through a variety of theoretical techniques [1,2,6].

The resonant levels in the cesium which are employed for the frequency locking technique are shown in Figure B-1. The particular transition in this manifold at 852.1 nm employed in the present experiments involves the F=5 and F=4 hyperfine levels (each with a degeneracy of 2F+1). The splitting between the F=3 and F=4 ground states is 9.193 GHz and is commonly used as a frequency standard in atomic clocks [5].

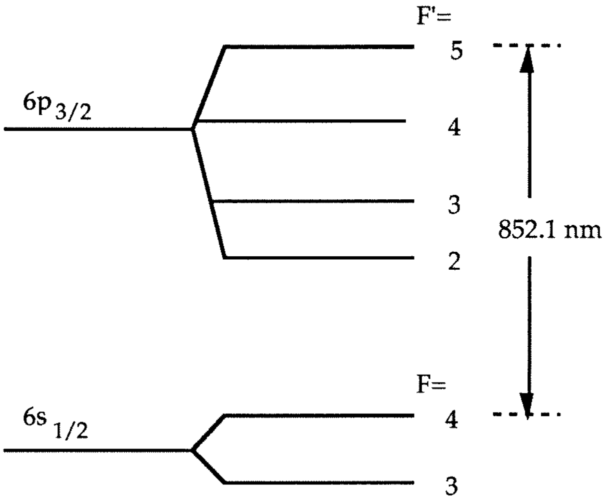

Figure B-1: Cesium level diagram at 852.1 nm

In order to calculate the energy shift with an applied magnetic field one needs the Lande g-factors which are given by [4]

$$g(F) = g(J)\frac{F(F+1)+J(J+1)-I(I+1)}{2F(F+1)} \tag{B.1}$$

$$g(J) = 1+\frac{J(J+1)-L(L+1)+S(S+1)}{2J(J+1)} \tag{B.2}$$

The energy shift produced by the magnetic field can then be calculated by

$$\Delta E = g m_F \hbar \omega_L \tag{B.3}$$

$F = 3$	-351 kHz/Gauss
$F = 4$	+350 kHz/Gauss
$F' = 2$	-934 kHz/Gauss
$F' = 3$	-0.55 kHz/Gauss
$F' = 4$	+373 kHz/Gauss
$F' = 5$	+560 kHz/Gauss

Table B.1: Frequency shifts due to magnetic field splitting.

where ω_L is the Larmor frequency. The frequency shifts for each of the levels are listed in Table B.1.

Assuming the selection rule of $\Delta m_F = 0, \pm 1$, there are 27 possible transitions each with a specific transition strength as shown in Figure B-2. If one groups these transitions into groups of constants Δm the following expressions for the transition energy are obtained

$$\begin{aligned} \Delta E &= \hbar\omega_o + \left[\tfrac{3m}{20} - \tfrac{2}{5}\right]\hbar\omega_L \quad \text{for} \quad \Delta m_F = 1 \\ \Delta E &= \hbar\omega_o + \tfrac{3m}{20}\hbar\omega_L \quad \text{for} \quad \Delta m_F = 0 \\ \Delta E &= \hbar\omega_o + \left[\tfrac{3m}{20} - \tfrac{2}{5}\right]\hbar\omega_L \quad \text{for} \quad \Delta m_F = -1 \end{aligned}$$

The susceptibility can now be expressed in the basis [6]

$$\hat{e}_+ = \frac{1}{\sqrt{2}}(\hat{x} + i\hat{y}) \tag{B.4}$$

$$\hat{e}_- = \frac{1}{\sqrt{2}}(\hat{x} - i\hat{y}) \tag{B.5}$$

$$\hat{e}_o = \hat{z} \tag{B.6}$$

as

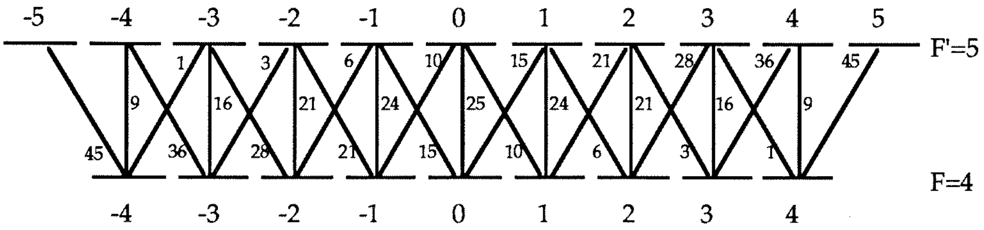

Figure B-2: Transition diagram for F'=5 to F=4 levels

$$\chi_{++} = \frac{e^2}{2\epsilon_o\hbar} \sum_{m_F=-4}^{+4} \frac{\left|\langle 5, m_F+1 \mid \frac{1}{\sqrt{2}}(\hat{x}+i\hat{y}) \mid 4, m_F\rangle\right|^2}{\left(\omega_o + \left[\frac{3m_F}{20}+\frac{2}{5}\right]\omega_L - \omega - i\frac{\Gamma}{2}\right)} \tag{B.7}$$

$$\chi_{--} = \frac{e^2}{2\epsilon_o\hbar} \sum_{m_F=-4}^{+4} \frac{\left|\langle 5, m_F-1 \mid \frac{1}{\sqrt{2}}(\hat{x}-i\hat{y}) \mid 4, m_F\rangle\right|^2}{\left(\omega_o + \left[\frac{3m_F}{20}-\frac{2}{5}\right]\omega_L - \omega - i\frac{\Gamma}{2}\right)} \tag{B.8}$$

$$\chi_{oo} = \frac{e^2}{2\epsilon_o\hbar} \sum_{m_F=-4}^{+4} \frac{\left|\langle 5, m_F \mid \hat{z} \mid 4, m_F\rangle\right|^2}{\left(\omega_o + \frac{3m_F}{20}\omega_L - \omega - i\frac{\Gamma}{2}\right)} \tag{B.9}$$

In order to take into account the Doppler broadening of the spectral lines one can define a Voigt parameter as

$$a = \frac{\Delta\nu_N}{\Delta\nu_D}\sqrt{\ln 2} \tag{B.10}$$

where $\Delta\nu_N$ is the natural linewidth and the Doppler linewidth is obtained from the

Maxwellian velocity distribution as

$$\Delta\nu_D = 2\sqrt{\ln 2}\frac{\nu_o}{c}\sqrt{\frac{2kT}{M}} \tag{B.11}$$

where M is the cesium atomic mass. An additional quantity $\Delta\nu_m$ relating the frequency difference of the transition to the Doppler linewidth is defined as

$$\nu_m^{\pm,0} = \frac{2\Delta\nu_m^{\pm,0}}{\Delta\nu_D}\sqrt{2\ln 2} \tag{B.12}$$

where $\Delta\nu_m$ is the transition frequency deviation from the zero field case.

With these definitions the expressions for the susceptibility now become

$$\begin{aligned}
\chi_{++} &= \frac{Ne^2 i\sqrt{\ln 2}}{2m\omega_o\epsilon_o\sqrt{\pi}\Delta\nu_D}\sum_{m_F=-4}^{4} W(\nu - {\nu_m}^{+1} + ia)f_m^{+1} && \text{(B.13)}\\
\chi_{--} &= \frac{Ne^2 i\sqrt{\ln 2}}{2m\omega_o\epsilon_o\sqrt{\pi}\Delta\nu_D}\sum_{m_F=-4}^{4} W(\nu - {\nu_m}^{-1} + ia)f_m^{-1} && \text{(B.14)}\\
\chi_{--} &= \frac{Ne^2 i\sqrt{\ln 2}}{2m\omega_o\epsilon_o\sqrt{\pi}\Delta\nu_D}\sum_{m_F=-4}^{4} W(\nu - {\nu_m}^{0} + ia)f_m^{0} && \text{(B.15)}
\end{aligned}$$

where the plasma dispersion fucnction W is defined by

$$\begin{aligned}
W(x+iy) &= \frac{i}{\pi}\int_{\infty}^{\infty} dt\left[\frac{\exp -t^2}{x+iy-t}\right] && \text{(B.16)}\\
&= W_{Re} + iW_{Im} && \text{(B.17)}
\end{aligned}$$

This function may be expanded as

$$W(z) = e^{z^2} + e^{-x^2} \frac{2i}{\sqrt{\pi}} \int_0^x dt e^{t^2} \tag{B.18}$$

One can see that the real part of the plasma dispersion function is simply a Gaussian while the imaginary part is given by

$$W_{Im} = \frac{2}{\sqrt{\pi}} \mathcal{D}(\zeta) \tag{B.19}$$

where $\mathcal{D}(\zeta)$ is defined as Dawson's integral [7].

It is now a straightforward matter of calculating the transmission through the magnetically active cesium medium sandwiched between crossed polarizers. Taking the incident electric field parallel to that of the first polarizer one obtains

$$T = \frac{1}{2} \exp -\overline{\alpha} L \left[\cosh \Delta\alpha L - \cos 2\rho L\right] \tag{B.20}$$

where $\overline{\alpha}, \Delta\alpha$, and ρ are defined as the absorption, circular dichroism, and rotary power, respectively. These quantities may be expressed in terms of the previous definitions as

$$\overline{\alpha} \;=\; \alpha_o \left\{ \sum_{m_F=-4}^{4} W_{Re}(\nu - \nu_m^{+1} + ia) f_m^{+1} + W_{Re}(\nu - \nu_m^{-1} + ia) f_m^{-1} \right\} \tag{B.21}$$

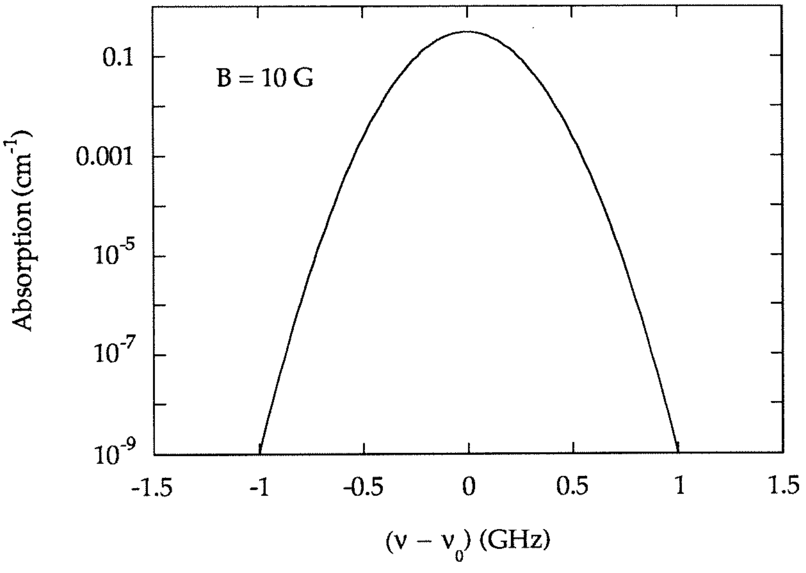

Figure B-3: Single pass absorption coefficient. $I/I_{sat} = 10$, Cell temperature = 25 °C.

$$\Delta\alpha = \alpha_o \left\{ \sum_{m_F=-4}^{4} W_{Re}(\nu - \nu_m^{+1} + ia) f_m^{+1} - W_{Re}(\nu - \nu_m^{-1} + ia) f_m^{-1} \right\} \quad (B.22)$$

$$\rho = \frac{\alpha_o}{2} \left\{ \sum_{m_F=-4}^{4} W_{Im}(\nu - \nu_m^{-1} + ia) f_m^{-1} - W_{Im}(\nu - \nu_m^{+1} + ia) f_m^{+1} \right\} \quad (B.23)$$

These quantities are plotted as a function of frequency in Figures B-3, B-4, and B-5.

The transmission is plotted in Figure B-6 as a function of frequency for various magnetic fields. At small magnetic fields such as those in Figure B-6, the transmission at linecenter is very small due to large absorption and a small rotation in the cesium. However, in the wings of the transition, the absorption can be neglected and the transmission is chiefly governed by the rotation explaining why transmission increases with magnetic field.

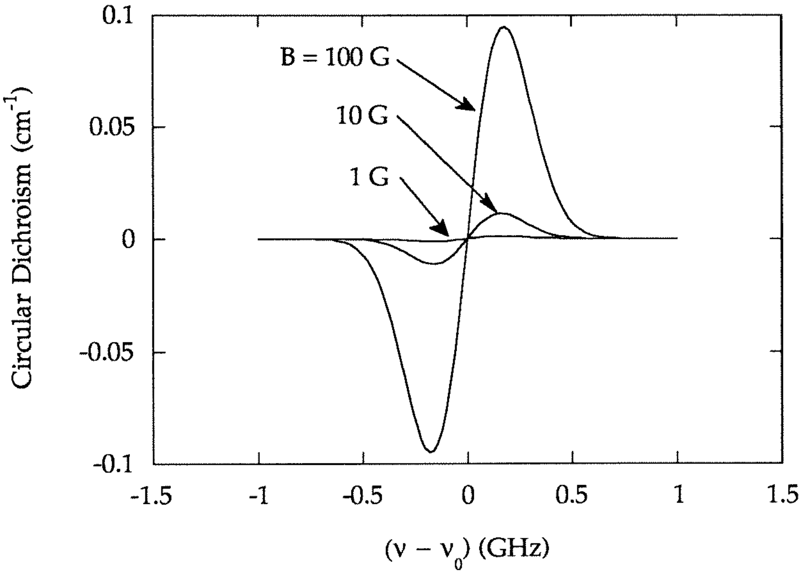

Figure B-4: Single pass circular dichrosim. I/I_{sat} = 10, Cell temperature = 25 °C.

It is also instructive to investigate the temperature dependence of this arrangement. Although the temperature causes an increase in the Doppler linewidth, it also effects the density of the cesium since cesium is a solid at room temperature. One can use the empirical relation [8]

$$\log P = 4.165 - \frac{3830}{T} \tag{B.24}$$

in order to calculate the vapor pressure of cesium as a function of temperature and then calculate the corresponding density. In Figure B-7 the peak transmission is plotted as a function of temperature. The transmission increases shown are a direct result of Equation B.24.

In order to calculate the transmission of the return probe beam, we can again

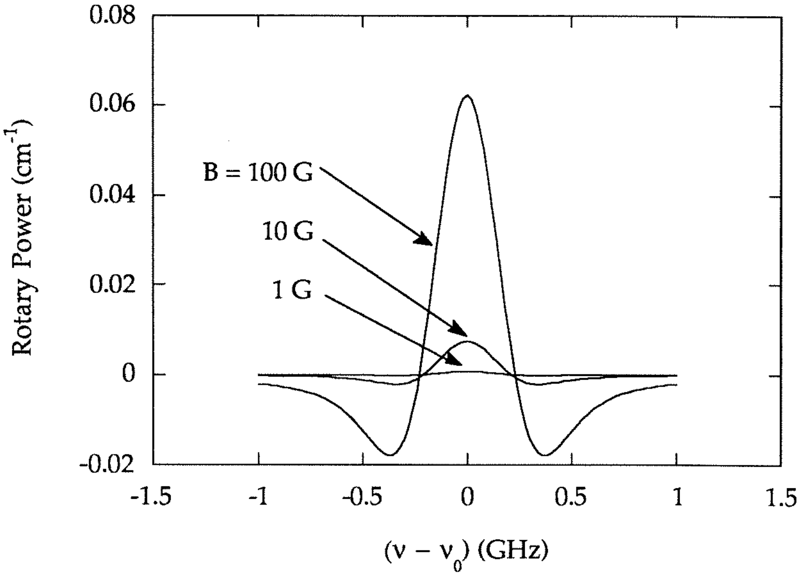

Figure B-5: Single pass rotary power. $I/I_{sat} = 10$, Cell temperature = 25 °C.

solve for the suscepibilities and use the formalism presented above. However, since the population is no longer in thermal equilibrium one must utilize a slightly different approach in solving for χ than that used in Equations B.7-B.9. A common technique for solving such a problem is to employ density matrices. The suscepibility for a two-level system can be written as

$$\chi(\omega') = \frac{N p_{12} \rho_{12}(\omega')}{E(\omega')} \tag{B.25}$$

where N is the atomic density, p_{12} is the dipole matrix element, and E is the electric field magnitude. The diagonal density matrix element ρ_{12} can be written as

$$\rho_{12}(\omega') = \frac{-(1/\hbar) p_{12} E(\omega') \Delta\rho}{\omega' - \omega_o + i\Gamma} \tag{B.26}$$

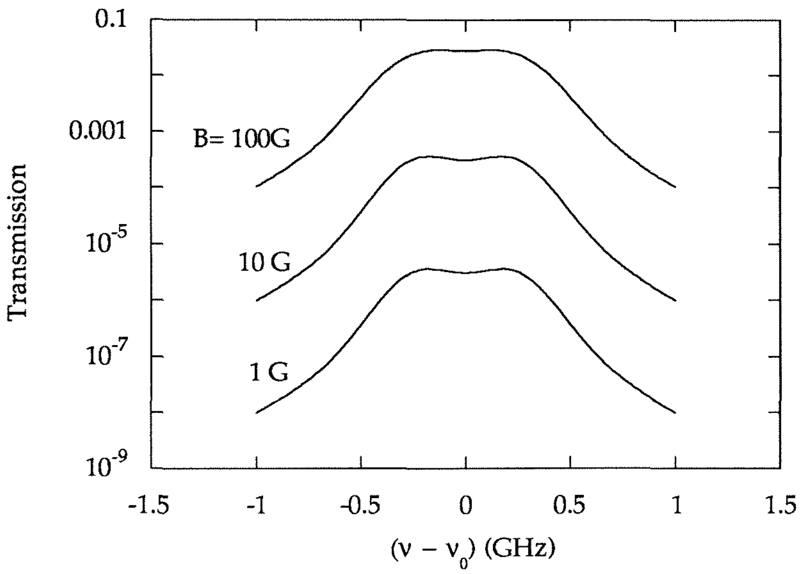

Figure B-6: Single pass transmission coefficient. Cell temperature = 25 °C.

The crucial element of this expression is the population function $\Delta\rho$ This quantity can be expressed as [3]

$$\Delta\rho = \Delta\rho^{o}\left[1 + \frac{\Gamma^2 I/I_{sat}}{(\omega - \omega_o)^2 + \Gamma^2}\right]^{-1} \tag{B.27}$$

where

$$\Delta\rho^{o}(v_z, \beta) = \frac{\Delta\rho^{oo}}{\sqrt{\pi}\beta} e^{-v_z^2/\beta^2} \tag{B.28}$$

where $\Delta\rho^{oo}$ is the population difference between the two states given by the Boltzmann distribution and β describes the Doppler broadening width.

The only atoms which both the pump *and* probe encounter are those which possess only transversal velocity components (i.e., $v_z = 0$). All other velocities are unaffected since the pump and probe are counterpropagating. This can be described by replacing

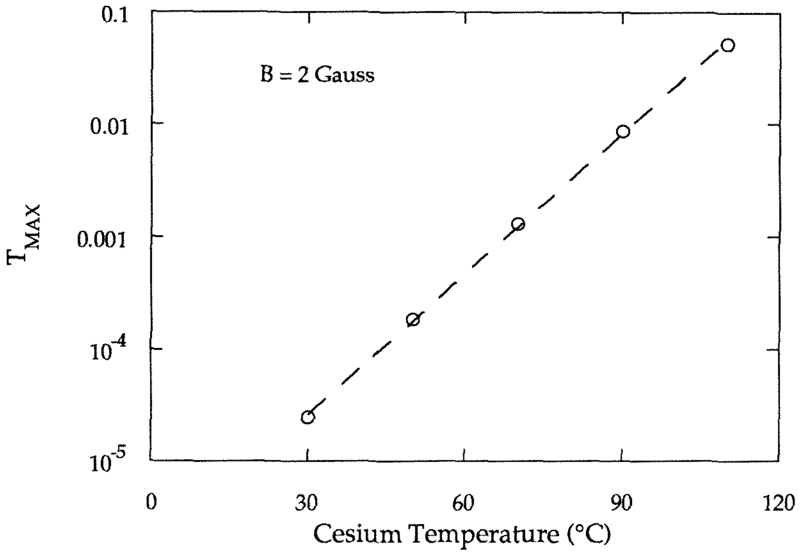

Figure B-7: Temperature dependence of single pass transmission

ω in the expression for $\Delta\rho$ with $\omega - kv$ and ω' in the expression for ρ_{12} with $\omega' + kv$. Furthermore, the expression for $\Delta\rho^o$ in Equation B.28 must be substituted into Equation B.27. With these substitutions one integrates over all positive and negative velocities yielding

$$\chi(\omega') = \frac{-N|p_{12}|^2\Delta\rho^{oo}}{\hbar\sqrt{\pi}\beta}\int_{-\infty}^{\infty} dv_z \frac{e^{-v_z^2/\beta^2}}{\left[1+\frac{\Gamma^2 I/I_{sat}}{(\omega-\omega_o+kv_z)^2+\Gamma^2}\right]\left[\omega'-\omega_o-kv_z+i\Gamma\right]} \tag{B.29}$$

By taking the real and imaginary parts of this integral the expressions for χ' and χ'' can be obtained. After a contour integration and application of the Kramers-Kronig relations one obtains [10]

$$\Delta\chi''(\omega') = \chi''_o\left[1-\frac{1}{\sqrt{1+I/I_{sat}}}\right]\cdot\frac{{\Gamma_{sat}}^2}{4(\omega-\omega_o)^2+{\Gamma_{sat}}^2} \tag{B.30}$$

$$\Delta\chi'(\omega') = 2\chi_o''\left[1 - \frac{1}{\sqrt{1 + I/I_{sat}}}\right] \cdot \frac{\Gamma_{sat}(\omega - \omega_o)}{4(\omega - \omega_o)^2 + \Gamma_{sat}{}^2} \tag{B.31}$$

where χ_o'' is the imaginary part of the susceptibility in the case of thermal equilibrium of the level populations (see Equations B.13-B.15), I_{sat} is the saturation intensity ($I_{sat} \approx 1$ mW/cm^2 in cesium), and the saturated linewidth is defined as

$$\Gamma_{sat} = \Gamma\left[1 + \sqrt{1 + \frac{I}{I_{sat}}}\right] \tag{B.32}$$

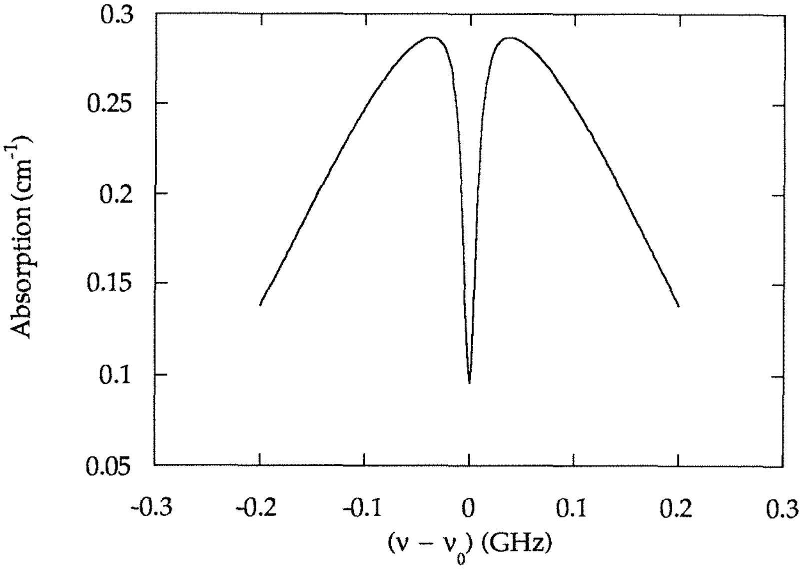

Figure B-8: Probe beam absorption coefficient. Temperature = 25°C.

At this point it is worth noting that this calculation of the modifications to the probe susceptibility has neglected several effects. With the counterpropagating pump/probe arrangement, the strong pump wave can alter the radiation and absorption lineshape function of the atoms. These effects have been investigated both

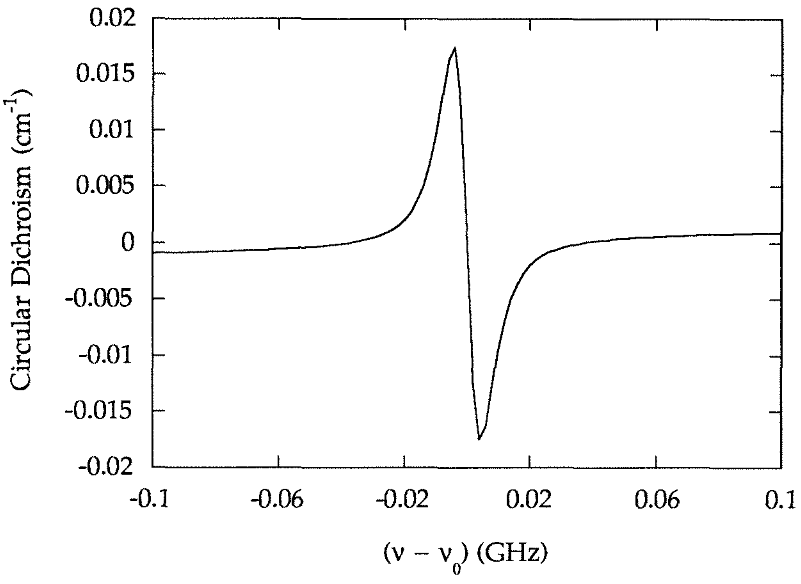

Figure B-9: Probe beam circular dichroism. Temperature = 25°C.

theoreticaly and experimentally and have been shown to be significant at large values of I/I_{sat} [9]. Other effects include spatial inhomogeneity of the beam profiles, transit time effects, and polarization crossover resonances. Discussions of several of these phenomena can be found in [10,9,3].

With the expressions for the susceptibility of the probe, one can calculate the transmission in the same manner as above for the pump beam. In Figures B-8, B-9, and B-10 are plotted the absorption, circular dichroism, and rotary power for a magnetic field of 1 Gauss at room temperature. As one might expect, the absorption profile is essentially the same as for the pump at all frequencies except at linecenter where the pump and probes interact with the same class of atoms. The width of the absorption dip is approximately equal to Γ_{sat} as defined above.

In Figure B-11, the total transmission function (i.e., the product of pump and

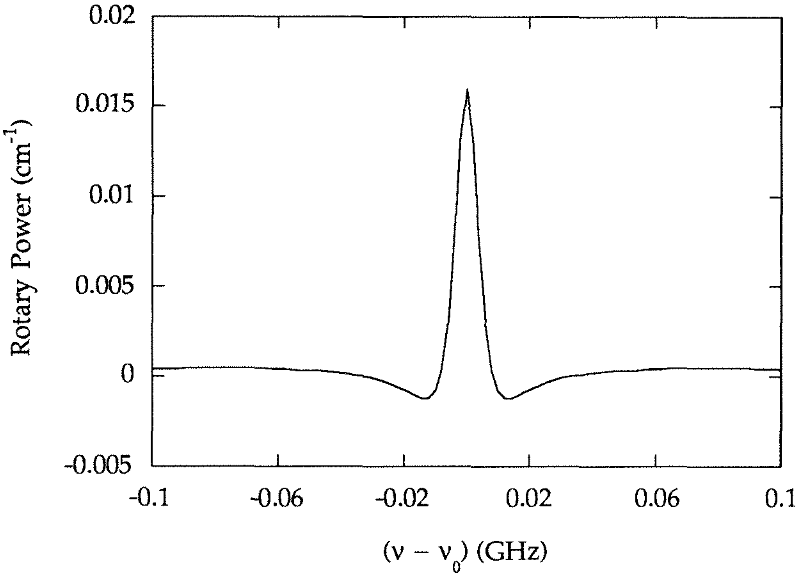

Figure B-10: Probe beam rotary power. Temperature = 25°C.

probe transmissions) is plotted for a magnetic field of 1 Gauss at room temperature. An extremely narrow Doppler-free feature is obtained at linecenter with a width also equal to Γ_{sat}. It is instructive to examine the dependence of transmission on the degree of saturation by the pump beam. In Figure B-12 one can see that pump intensities above 30-40 times saturation intensity increase the transmission only very slightly.

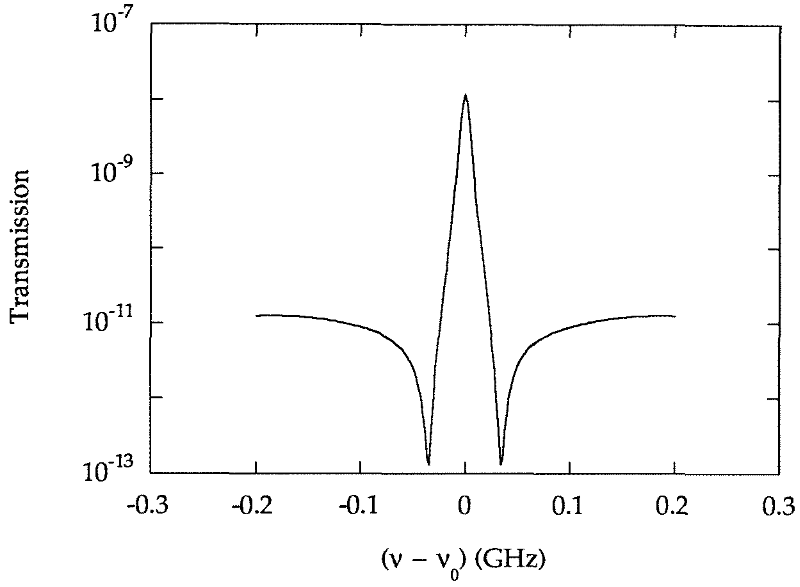

Figure B-11: Two-pass transmission function. Temperature = 25°C.

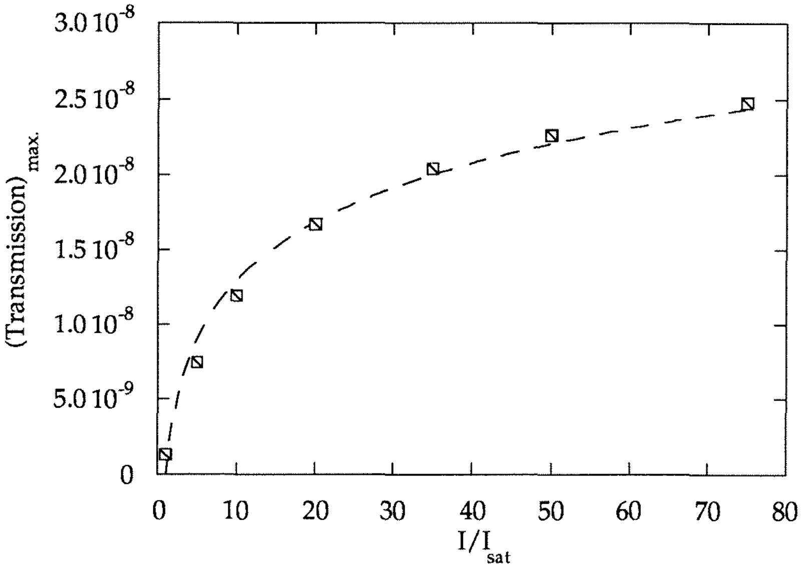

Figure B-12: Calculated maximum two-pass transmission as a function of input pump intensity.

References

[1] J.Menders, K.Benson, S.H.Bloom, C.S.Liu, and E.Korevaar, *Opt. Lett.*, vol.16, p.846, 1991.

[2] N.Cyr and M.Tetu, *Opt. Lett.*, vol.16, p.946, 1991.

[3] Y.R.Shen, *The Principles of Nonlinear Optics*, John Wiley and Sons, New York, 1982.

[4] E.U.Condon and G.H.Shortley, *The Theory of Atomic Spectra*, Cambridge University Press, London,1967.

[5] M.Ohtsu, *Highly Coherent Semiconductor Lasers*, Artech House, Boston, 1992.

[6] P.Yeh, *Appl. Opt.*, vol.21, p.2069, 1982.

[7] M.Abramowitz and I.A.Stegun, *Handbook of Mathematical Functions*, Dover, New York, 1972.

[8] *CRC Handbook of Chemistry and Physics*, CRC Press, 64th edition, 1984.

[9] V.S.Letokhov and V.P.Chebotayev, *Nonlinear Laser Spectroscopy*, Springer-Verlag, New York, 1977.

[10] M.A.Levenson and S.Kano, *Introduction to Nonlinear Laser Spectroscopy*, Academic Press, Boston, 1988.

Appendix C

Generation of Broadband Analog Noise

Broadband white noise is commonly found in physical systems such as the thermal noise across a resistor or reverse biased diode. While in principle these could be used as voltage sources for white noise, they suffer from the limitation of a small and fixed output noise power. Further amplification would lead to the complication of the spectral response of the amplifier stage. Because of these and other complications, such devices are not well suited for serving as variable amplitude noise sources.

Several methods have been proposed and demonstrated for the generation of white noise signals. Among these are signal transformations [2] and chaotic maps [3]. A more direct and practical approach to the generation of broadband white noise is by filtering random digital signals. A common technique of generating "random" digital signals is the pseudo-random bit sequence (PRBS) generator [1]. This method produces a digital bit stream that is truly non-periodic over some maximum length. The assurance of this achieving this maximum length is governed by the specifics of the circuit design. The bit stream (which can be up to several million bits long) is then repeated producing a periodicity of very low frequency. Through analog low-pass filtering of this output, white Gaussian distributed noise is produced.

The circuitry used to generate the maximal length sequence is shown in Figure C-1. Shift registers (No.74F675A) generate a bit stream at a rate determined by the clock frequency. Certain bits in this stream are selected, passed through an exclusive-OR gate (No.74F04) and fed back into the shift registers. The selection of these particular bit positions (referred to as tap points) is vital to producing a maximal length sequence.

The output at this point is TTL (0-5V). After passing through a CMOS analog switch (No.CD4053) a symmetrical signal with respect to ground is produced. A typical signal at this point is shown in Figure C-2. This signal possesses interesting spectral characteristics such as periodicity at a frequency equal to the inverse of the maximal length generation time, and nodes in the spectrum at the clock frequency and all its multiples (see Figure C-3). It can be shown that the power spectrum of this digital signal consists of a series of delta functions under an envelope described by [1]

$$\left(\frac{\sin x}{x}\right)^2 \tag{C.1}$$

where

$$x = \pi \frac{f}{f_{clock}} \tag{C.2}$$

The noise voltage can be written as

$$V_{rms} = 5V\left(\frac{2}{f_{clock}}\right)^{1/2} \tag{C.3}$$

This expression remains valid for frequencies less that approximately 10

In Figure C-4 we show a typical noise signal produced from this technique with low-pass filtering at 2.5 kHz. As shown in Figure C-5, the spectrum of the noise amplitude is white to within 1 dB from approximately DC to 1 kHz. Wider band noise is easily obtained by utilizing a larger clock frequency in the generator.

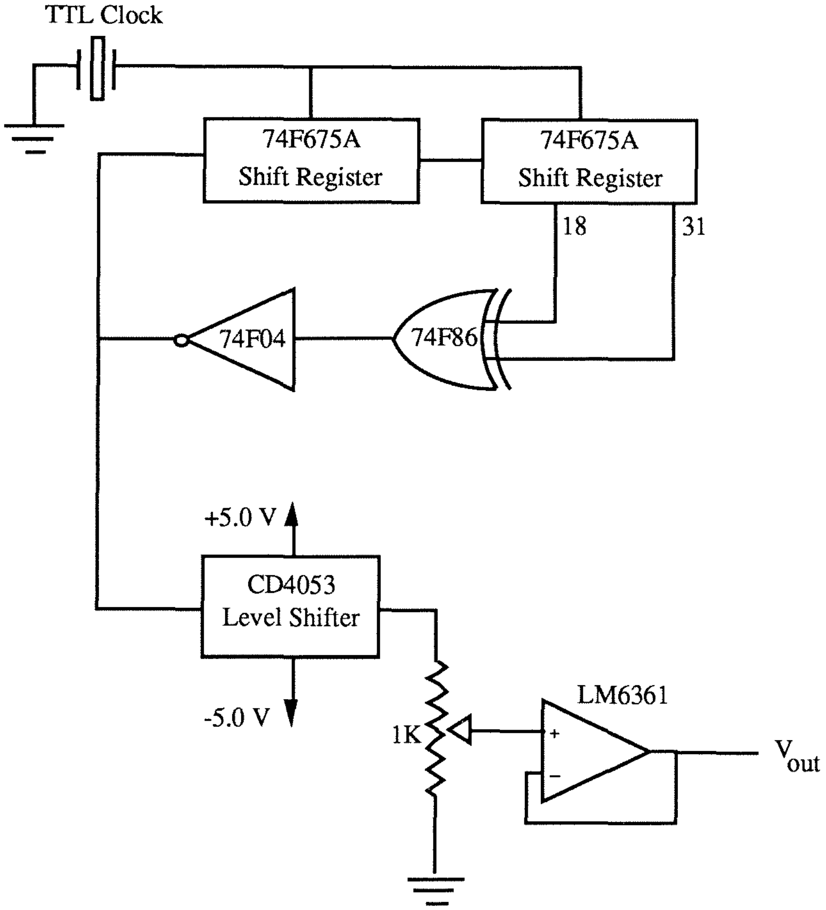

Figure C-1: Circuit schematic for the PRBS generator. All circuit components are supplied with power from individual regulators to eliminate cross contamination. Additionally, all supply leads are bypassed with 0.1 μF ceramic disc capacitors.

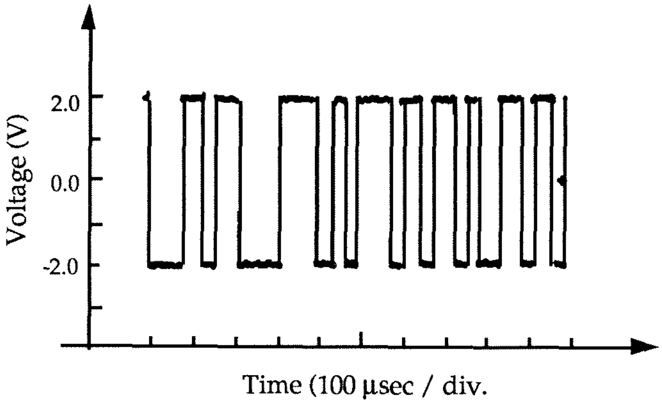

Figure C-2: Digital output of the PRBS generator with clock frequency of 40 kHz

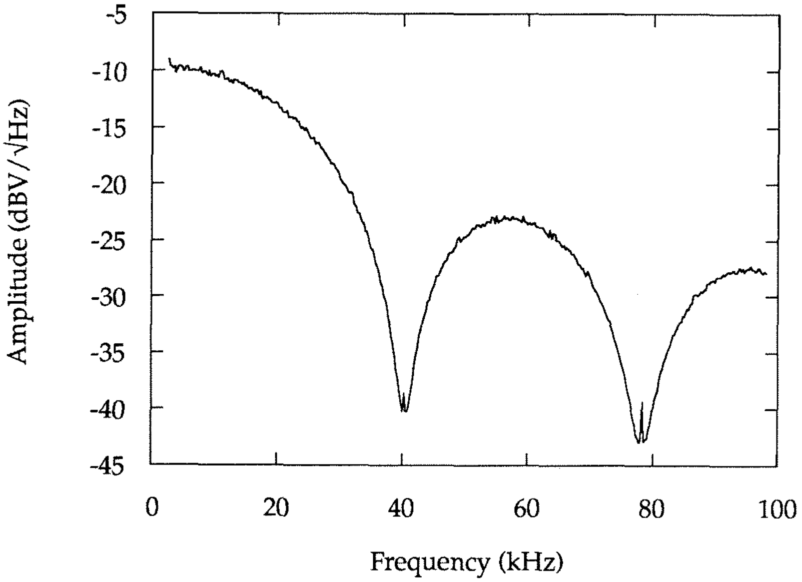

Figure C-3: Spectrum of the PRBS generator before filtering

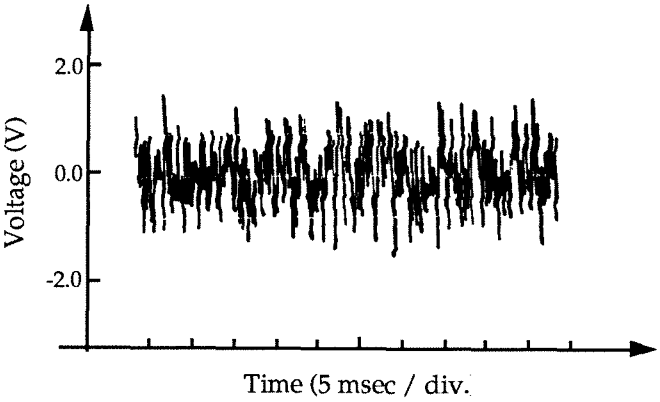

Figure C-4: Analog filtered noise with low-pass filtering at 2.5 kHz

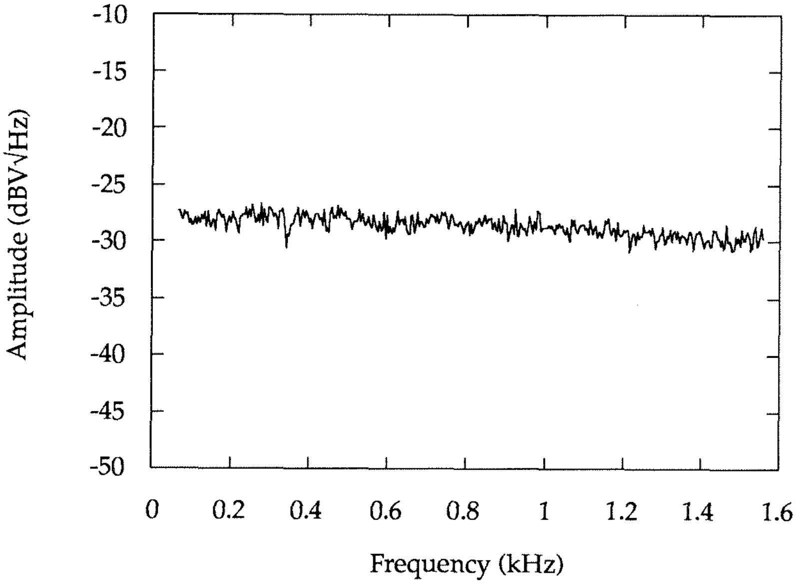

Figure C-5: Spectrum of the PRBS after low-pass filtering

References

[1] P.Horiwitz and W.Hill, *The Art of Electronics*, Cambridge University Press, Cambridge, 1989.

[2] A.Karim, S.Al-Bayati, and A.A.Aljudi, *Int. J. Electronics*, vol.70, p.321, 1991.

[3] G.C.McGonigal and M.I.Elmasry, *IEEE Trans. Circuits Syst.*, vol.34, p.981, 1987.